

From cold seeps to hot vents on the Nubian/Eurasian plate boundary in the North Atlantic Ocean

DISSERTATION

zur Erlangung des Doktorgrades

an der Mathematisch- Naturwissenschaftlichen Fakultät

der Christian-Albrechts Universität zu Kiel

Vorgelegt von

Christopher Schmidt

Kiel, 2019

Referent: Prof. Klaus Wallmann

Korreferent: Priv.-Doz. Dr. Thor Hansteen

Tag der mündlichen Prüfung: 29.11.2019

Zum Druck genehmigt: 29.11.2019

Der Dekan

Erklärung

Hiermit erkläre ich, dass ich die vorliegende Doktorarbeit selbstständig und ohne Zuhilfenahme unerlaubter Hilfsmittel erstellt habe. Weder diese noch eine ähnliche Arbeit wurde an einer anderen Abteilung oder Hochschule im Rahmen eines Prüfungsverfahrens veröffentlicht oder zur Veröffentlichung vorgelegt. Ferner versichere ich, dass die Arbeit unter Einhaltung der Regeln guter wissenschaftlicher Praxis der Deutschen Forschungsgemeinschaft entstanden ist. Ich versichere das mir noch kein akademischer Titel entzogen wurde.

Christopher Schmidt

Abstract

Hot and cold fluid expulsions at the seabed are common phenomena in various tectonic settings. Both temperature endmembers play a major role in the element exchange between the lithosphere and the ocean. Understanding the formation and processes involved in fluid generation is the key to understand the impact of fluid discharge on global element cycles. Hot and cold vents normally appear in different tectonic settings, where hot vents are most common in spreading centers and cold vents are present in active and passive continental margin settings. This study focuses on the western and eastern end of the Nubian/Eurasian plate boundary in the North Atlantic Ocean. The Nubian/Eurasian plate boundary and its specific tectonic characteristics with a spreading environment in the western part (Azores Plateau and Terceira Rift) and a compressional and strike-slip setting at its eastern end (Gulf of Cadiz) allows for, both, hot and cold fluid venting.

The first part of this study comprises a novel fully-coupled, basin-scale, reaction-transport model to simulate the fluid genesis of five mud volcanoes in the Gulf of Cadiz, at the eastern end of the Nubian/Eurasian plate boundary. The study was designed to investigate fluid formation processes that were previously postulated by Hensen et al. (2015). An advantage of this model is the coupling of a realistic geophysical setting with geochemical processes, considering a growing sediment column over time together with compaction of sediments as well as diffusion and advection of dissolved pore water species and chemical reactions. The modeled processes affecting the fluid genesis include the dehydration of clay minerals and the recrystallization of calcium carbonate. In addition to that, we tested if a circulation of fluids through aged (>140 Ma) oceanic crust could also affect fluid genesis. The model is capable to reproduce the fluid signatures (chloride, strontium and $^{87}\text{Sr}/^{86}\text{Sr}$) of all mud volcanoes. With this modeling approach we confirm the hypothesis that fluid circulation along deeply rooted strike slip faults old oceanic crust is likely affecting the fluid composition at the studied mud volcanoes.

The second chapter of this study gives a first comprehensive overview of pore water compositions for the magmatically active Azores Plateau, at the western end of the Nubian/Eurasian plate boundary. The data set comprises 22 gravity cores with various different geochemical fluid patterns. Most gravity cores are affected by early diagenetic processes like AOM, carbonate precipitation and recrystallization. Furthermore, also weathering of volcanic compounds could affect the pore water patterns. Despite the ongoing

volcanic activity no deep submarine hydrothermal systems at the Azores plateau are described to date. Here we report for the first time clear indications for the existence of sediment hosted hydrothermal systems on the Azores Plateau. The geochemical signals of the four identified systems are typical mid-oceanic-ridge signals, with increased Ca and depleted Mg and SO₄ fluids, indicating a hydrothermal alteration of the basement. In order to distinguish those signals from ash alteration we underline our findings by seismic profiles showing sill intrusions and fluid conduits as well as free gas in the subsurface.

The last chapter provides a multi element and isotope analyses of a hydrothermal vent in the Terceira Rift, at the western end of the Nubian/Eurasian plate boundary. Fluids sampled in the Terceira Rift show elevated Mg, SO₄ and total alkalinity values. Those fluids do not show the typical trends known from hydrothermal vents at mid-oceanic spreading centers. The most straightforward interpretation of those findings is the dissolution of the hydrothermally formed mineral caminite, an Mg-sulfate-hydroxide-hydrate. Caminite is a rare mineral but proposed to form under specific conditions such as high temperature and inhibited Mg-smectite formation in hydrothermal recharge zones. In general, those conditions are met in the Terceira Rift. We propose the hydrothermal system is in a waning state and caminite dissolves as it is shifted out of the temperature stability field by progressive cooling of the hydrothermal system. Enriched fluids are rising to the seafloor via slow advection through listric faults.

Zusammenfassung

Heiße und kalte Fluidaustritte sind bekannte Phänomene am Meeresboden, treten aber generell in völlig verschiedenen tektonischen Milieus auf. Während heiße Quellen typischerweise im Bereich mittelozeanischer Rückensysteme zu finden sind, treten kalte Quellen bevorzugt an aktiven und passiven Kontinentalrändern auf. Sowohl heiße als auch kalte Quellen spielen eine wichtige Rolle im Austausch von chemischen Elementen zwischen dem Ozean und der Lithosphäre. Demnach stellt ein besseres Verständnis der Entstehung solcher Quellen sowie der Reaktionen, die während der Fluidbildung ablaufen, einen wichtigen Baustein dar, um ihren Einfluss auf globale Stoffkreisläufe im Ozean zu erfassen und zu quantifizieren. Die vorliegende Studie betrachtet die Untersuchung von Entwässerungsstrukturen am westlichen und östlichen Ende der afrikanisch/europäischen Plattengrenze im Atlantischen Ozean. Die spezielle tektonische Konstellation mit einer divergenten Plattengrenze im westlichen Teil (Azoren Plateau und Terceira Graben) und der Kombination aus einer Transformstörung und einer konvergenten Plattengrenze am östlichen Ende (Golf von Cádiz) beherbergt beide Arten von Fluidquellen.

Der erste Teil dieser Arbeit besteht aus einem neu entwickelten, großskaligem, gekoppelten Transport-Reaktions-Modell zur Simulation der Fluidgenese von 5 Schlammvulkanen im Golf von Cádiz (östliches Ende der afrikanisch/europäischen Plattengrenze). Diese Studie wurde im Wesentlichen durchgeführt, um eine von Hensen et al. (2015) entwickelte Hypothese zur Fluidentstehung zu überprüfen. Ein Vorteil dieses Modellansatzes ist die realistische Kopplung von geophysikalischen und geochemischen Prozessen, wie zum Beispiel einer über die Zeit anwachsenden Sedimentsäule unter der Berücksichtigung gleichzeitiger Kompaktion der Sedimente, sowie die Berechnung von diffusivem und advektivem Transport gelöster Stoffe im Porenwasser und deren chemischer Reaktionen. Die modellierten Prozesse der Fluid Entstehung umfassen die Entwässerung von Tonmineralen und die Rekristallisation von Karbonatsedimenten. Mit dem Modell können Fluidsignaturen (Chlorid, Strontium und $^{87}\text{Sr}/^{86}\text{Sr}$) für alle Schlammvulkane reproduziert werden. Zusätzlich wurde eine Zirkulation von Meerwasser in alter Ozeankruste (>140 Ma), wie von Hensen et al. (2015) vorgeschlagen, simuliert. Die Ergebnisse dieses Ansatzes unterstützen die Hypothese, dass die Zirkulation von Fluiden in der ozeanischen Kruste die Entstehung der Fluide an den untersuchten Schlammvulkanen beeinflusst.

Der zweite Teil dieser Arbeit umfaßt erstmalig einen grundsätzlichen Überblick über die Porenwassergeochemie von Oberflächensedimenten des magmatisch aktiven Azoren

Plateaus am westlichen Ende der afrikanisch/europäischen Plattengrenze. Der vorliegende Datensatz von 22 Schwerelotkernen zeigt eine Reihe verschiedener geochemischer Signaturen, die unter anderem auf frühdiagenetische Prozesse wie die anaerobe Methanoxidation, Fällung von Kalziumkarbonat bzw. dessen Rekristallisation hinweisen. Des Weiteren finden sich auch Anzeichen für die Verwitterung vulkanischer Bestandteile im Sediment. Trotz der anhaltenden vulkanischen Aktivität des Plateaus sind bisher keine Hydrothermalquellen im tiefmarinen Milieu bekannt. Diese Studie erbringt erstmalig Hinweise für hydrothermale Aktivität auf dem Azoren Plateau. Die geochemische Zusammensetzung dieser Systeme, die durch Berechnung von Endgliedern ermittelt wurde, ähnelt mit der Anreicherung von Ca und der Abnahme von Mg und SO₄ der Zusammensetzung bekannter mittelozeanischer Quellen. Das Auftreten dieser geochemischen Signaturen deckt sich in den meisten Fällen mit Auftreten magmatischer Intrusionen, von Fluid-Kanälen sowie von Gasanreicherungen im Untergrund, was unsere Interpretationen untermauert.

Das letzte Kapitel zeigt eine Multi-Element und Isotopen Analyse einer vermutlich hydrothermalen Quelle im Terceira Graben, am westlichen Ende der afrikanisch/europäischen Plattengrenze. Porenwasserproben aus dem Terceira Graben zeigen hier allerdings ungewöhnlich hohe Konzentrationen von Mg und SO₄ sowie erhöhte Alkalitätswerte, womit sie deutlich von typischen Fluid-Trends von Hydrothermalsystemen an mittelozeanischen Rücken abweichen. Die Resultate sind am besten durch die Auflösung des hydrothermal gebildeten Minerals Caminit, eines Magnesium-Sulfat-Hydroxid-Hydrates, erklärbar. Bislang gibt es nur einzelne Meeresbodenfunde von Caminit, weil dieses Mineral ein sehr enges Stabilitätsfenster hat und unter normalen Tiefseebedingungen instabil ist. Allerdings ist es vorstellbar, dass das Mineral unter bestimmten Bedingungen, wie z.B. das Vorherrschen hoher Temperaturen in bereits alterierter Kruste, in tieferen Bereichen hydrothermalen Systeme in großen Mengen gebildet werden kann. Da der Terceira Graben grundsätzlich diese Bedingungen erfüllt, kann man im Falle einer abklingenden hydrothermalen Aktivität, verbunden mit einer fortlaufenden Abkühlung des Systems, davon ausgehen, dass sich vormals gebildete Caminit-Vorkommen wieder auflösen, was wiederum zu der Bildung Mg- und SO₄-reicher Fluide führt. Die Fluide steigen entlang listrischer Verwerfungen durch die Sedimentdecke langsam zum Meeresboden auf.

Table of Contents

Abstract.....	I
Zusammenfassung.....	III
Table of Contents	V
I. Introduction	1
I.I Cold Seeps and Mud Volcanoes.....	2
I.II Hydrothermal systems	3
I.III Global Mg cycle.....	4
I.IV Volcanic Ash weathering.....	7
I.V The Nubian/Eurasian plate boundary in the North Atlantic Ocean.....	9
I.VI Thesis Outline	10
I.VII References	11
II. Genesis of mud volcano fluids in the Gulf of Cadiz using a novel basin-scale model approach.....	17
Abstract.....	18
II.1 Introduction	19
II.2 Geological setting of the Gulf of Cadiz	21
II.3 Reactive-transport model	22
II.3.1 General concept	22
II.3.2 Reaction solver.....	23
II.3.2.1 Clay dehydration	23
II.3.2.2 Carbonate recrystallization	24
II.3.2.3 Fluid injection from basement	24
II.3.2.4 Strontium isotopes.....	25
II.3.3 Boundary conditions and initial conditions.....	25
II.3.3.1 Dissolved species	25
II.3.3.2 Solid species.....	27

II.3.4 Solution algorithm.....	28
II.4 Model case studies	29
II.4.1 Case study I: Captain Arutyunov MV.....	29
II.4.2 Case study 2: ATI MVs.....	33
II.4.3 Case study 3: Porto MV	36
II.4.4 Summary of case studies	39
II.5 Conclusions and implications.....	41
References.....	42
III Insights into pore fluid geochemistry of the Azores Plateau: From early diagenesis to hydrothermal vents.....	49
Abstract.....	50
III.1 Introduction.....	51
III.2 Regional Setting	52
III.3 Materials and Methods.....	53
III.3.1 Sediment and pore water sampling.....	53
III.3.2 Pore water analyses.....	55
III.3.3 Isotope analyses	55
III.3.4 Head space gas analyses.....	56
III.3.5 Solid phase	56
III.3.6 Seismic data.....	56
III.3.7 Numerical reaction transport model	56
III.3.7.1 AOM Model.....	57
III.3.7.2 Carbonate recrystallization model	57
III.3.8 End member calculation.....	57
III.4 Results.....	57
III.4.1 Pore water chemistry.....	57
III.4.1.1 Background GCs Azores Plateau.....	60
III.4.1.2 Background GCs Terceira Rift	60

III.4.1.3 Hydrothermally influenced GCs.....	60
III.4.2 Isotope data.....	61
III.4.3 Head space gas.....	61
III.4.3 Solid phase	61
III.4.4 Seismic lines.....	63
III.4.4.1 M113-75	63
III.4.4.2 M113-73	63
III.4.4.3 M113-17	64
III.4.4.4 M79-20/21	64
III.4.4.5 M79-30	64
III.5 Discussion.....	65
III.5.1 Background GCs Azores Plateau.....	65
III.5.1.1 Ash rich GCs.....	65
III.5.1.2 Ash poor GCs.....	66
III.5.1.3 “Fried Eggs” GCs.....	71
III.5.2 Background GCs Terceira Rift.....	72
III.5.3 Hydrothermally influenced GCs.....	73
III.5.3.1 Hydrothermal vent west of São Jorge (GC38)	74
III.5.3.2 Hydrothermal vent between São Jorge and Pico (GC36).....	75
III.5.3.3 “Fried Eggs” hydrothermal vent (GC23)	76
III.5.3.4 Hydrothermal vent north of the Hironnelle Basin (GC46).....	77
III.5.3.5 West of Monaco Bank (GC13).....	77
III.6 Conclusions and Outlook.....	78
References.....	79
IV. Origin of high Mg and SO ₄ fluids in sediments of the Terceira Rift, Azores - indications for caminite dissolution in a waning hydrothermal system.....	83
Abstract.....	84
Plain Language Summary.....	84

IV.1 Introduction.....	85
IV.2 Materials and Methods	86
IV.2.1 Pore fluid and sediment sampling	86
IV.2.2 Pore fluid analyses.....	87
IV.2.3. Solid phase analyses	87
IV.2.4 Smear slides.....	87
IV.2.5 Si Isotopes	88
IV.2.6 Sulfur Isotopes.....	89
IV.2.7. Sr Isotopes.....	89
IV.2.8. Ca Isotopes	90
IV.2.9 Mg Isotopes.....	90
IV.2.10 Head Space gas analyses.....	91
IV.2.11 Endmember calculations	92
IV.2.12 Thermodynamic model.....	93
IV.2.13 Transport model.....	94
IV.2.14 Seismic data.....	94
IV.3 Results	95
IV.3.1 Pore fluid composition and isotope data.....	95
IV.3.2 Solid phase	99
IV.3.3 Head space gas	99
IV.4 Discussion.....	100
IV.4.1 Near-surface diagenetic processes.....	100
IV.4.2 Indications for upward fluid flow.....	101
IV.4.3 Hydrothermal signature	101
IV.4.3.1 SO ₂ enriched volatiles.....	102
IV.4.3.2 Anhydrite dissolution.....	102
IV.4.3.3 Mg-rich smectite.....	103
IV.4.3.4 Low temperature weathering of peridotite.....	104

IV.4.4 Dissolution of Caminite	104
IV.4.5 End member calculation	106
IV.4.6 Implications.....	108
IV.5 Summary and conclusions	109
References.....	110
V. Conclusion	115
Acknowledgements	117
Appendix A for chapter II.....	119
Appendix B for chapter III	125
Appendix C for chapter IV	137

I. Introduction

Hot and cold fluid expulsions are common phenomena in various marine settings (Fig. I; Herzig and Hannington, 2006; Kopf, 2002). Submarine hydrothermal fluid vents occur in areas with magmatic activity such as mid-oceanic spreading centers, back arc settings and intraplate hot spots (Beaulieu et al., 2013). Cold vents and mud volcanoes are generally found in convergent tectonic settings and in areas with high sediment accumulation (Kopf, 2002; Mazzini and Etiope, 2017; Milkov, 2000; Suess et al., 1985). Fluid expulsion in marine transform faults and fracture zones apart from spreading centers is less common (Hensen et al., 2019). Most known vents/seeps are located in ridge - ridge transform faults, e.g. VEMA Fracture Zone in the Central Atlantic Ocean (Cannat et al., 1991; Devey et al., 2018). On large scale fracture zones, e.g. the Azores-Gibraltar Fracture zone (AGFZ), active fluid vents have not been described to date. However, for the Tydeman fracture zone hydrothermal fluid circulation is assumed based on seismic data (Calvert and Potts, 1985; Potts et al., 1986), but not confirmed by ground truthing yet.

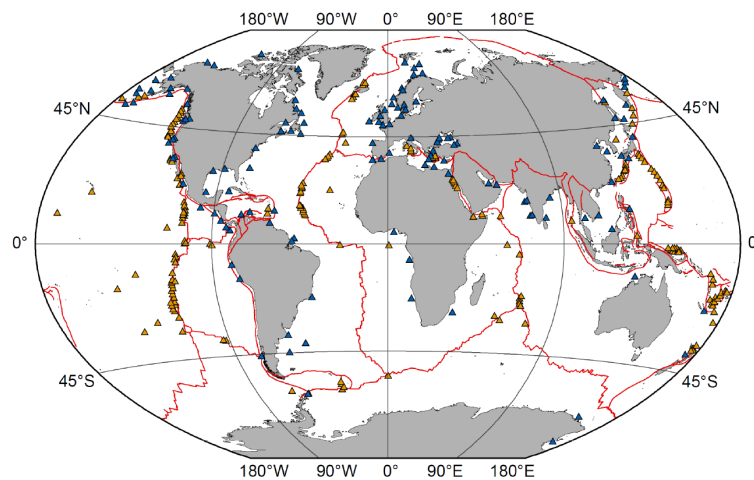


Fig I.I Map of global occurrence of hydrothermal systems and cold seeps taken from Scholz (2009). Yellow triangles mark hydrothermal systems; blue triangles are cold seeps and mud volcanoes

Hydrothermal systems and cold seeps play both a significant role in various global element and isotope cycles between the lithosphere and hydrosphere. The main elements and isotope systems affected are Mg, SO₄, Ca, Sr, Li, CH₄, ⁸⁷Sr/⁸⁶Sr and δ²⁶Mg (e.g. Berg et al., 2019; Berndt et al., 2016; James et al., 1999; Nielsen et al., 2006; Scholz et al., 2010). Processes affecting the fluid genesis can differ from diagenetic process in the sediment column to leaching of elements from hard rocks and mineral precipitation.

I.I Cold Seeps and Mud Volcanoes

Mud volcanoes (MVs) and cold seeps are manifestations of deep sourced processes in sediments emanating fluids and gas, on the sea floor. Fluid temperatures in cold seeps and mud volcanoes are generally slightly elevated in contrast to the surrounding seawater (4°C) with an increase of up to 5°C (Kopf, 2002). Fluids emitted by MVs are important for the element flux from the lithosphere to the hydrosphere, as they are typically enriched in CH₄ and elements like Ba, B, Sr and Li (Hensen et al., 2007; Scholz et al., 2010; Scholz et al., 2009; Wallmann et al., 2006). Cold fluid escape structures can be found worldwide in convergent tectonic settings e.g. Gulf of Cadiz (NE Atlantic Ocean, Hensen et al., 2007; Scholz et al., 2009) or the Costa Rica convergent margin (Linke et al., 2005; Schmidt et al., 2005; Shipley et al., 1990) and where sediment accumulation is high, e.g. on the Nile deep-sea fan (Mediterranean Sea; Feseker et al., 2010), the Haakon Mosby MV (Arctic Ocean Norway; Vogt et al., 1997) or in the Congo Delta (Sahling et al., 2008).

Mud volcanism can be caused by various drivers, prerequisite a density inversion (Kopf, 2002). A primary density inversion can be caused by density contrast of buried sediments. A major mineral with low density in the marine environment is smectite. If rapid burial or low permeability layers overlying these sediments overpressure is generated quickly, causing fluids to rise upwards (e.g. Westbrook and Smith, 1983). Furthermore also thermogenic processes such as clay dehydration can cause overpressure in sediments as additional fluids are added to ambient pore fluids (e.g. Fitts and Brown, 1999). In addition to that, high organic matter input into sediments lead to a microbial or thermogenic gas generation which also generates overpressure in buried sediments (Suess et al., 1999). In most MVs several of the above mentioned processes can act simultaneously causing fluids and mud to rise to the seafloor (Kopf, 2002).

Fluid geochemistry of MVs can vary significantly, deepening on sedimentary deposits. Most of the following described processes occur simultaneously but have contradictory effects on the fluid composition what makes a differentiation in fluids sometimes a challenging task. A major processes changing the fluid composition is the clay dehydration (Hensen et al., 2007; Kastner et al., 1991). Clay dehydration leads to a freshening of the pore fluids causing a decrease for Cl. A second major process is the thermogenic and microbial mineralization of organic matter (Fehn et al., 2003). Organic matter degradation leads to the formation of methane and CO₂. Under low temperature and high pressure conditions gas hydrates form and modify the Cl composition of the fluids (Haeckel et al., 2004; Torres et al.,

2004). Mud volcano fluids in the Gulf of Cadiz are also affected by the recrystallization of carbonates. This process strongly enriches Sr concentrations in the ambient fluids compared to seawater levels (Hensen et al., 2015). The presence of salt diapirs and the dissolution of evaporites cause an increase of the salinity of the ambient pore fluids (Haffert et al., 2013; Reitz et al., 2007; Wallmann et al., 1997). This process can be distinguished by a 1:1 increase of Na and Cl. Formation and dissociation of gas hydrates has an impact on chlorinity of ambient pore fluids (Hensen and Wallmann, 2005; Martin et al., 1993; Suess et al., 1999; Wallmann et al., 2018).

I.II Hydrothermal systems

Hydrothermal systems develop in regions with magmatic activity and most of these systems are found at mid-ocean spreading centers. Seawater is typically recharged into the oceanic basement at the flanks of the spreading centers and can be heated up to temperatures of over 400 °C (Herzig and Hannington, 2006). Circulation of fluids through hydrothermal systems is one of the major drivers for the cooling of young oceanic crust (Elderfield and Schultz, 1996). Heat is therefore the main driver for a hydrothermal convection cell. In general, hydrothermal fluid circulation through the basement ceases at a crustal age of 65 ± 10 Ma due to sealing by an increasing sediment cover (Stein et al., 1995). During the heating of the fluids, the geochemical signature of fluids is modified due to reactions with the surrounding oceanic crust. Fluids of hydrothermal systems are characterized by the depletion of Mg and SO₄ while Ca is enriched (Fig. I.II; Elderfield and Schultz, 1996). The major process involved are (i) the formation of Mg-rich smectite, (ii) the precipitation of anhydrite and other sulfide minerals, and (iii) the albitization of plagioclase (Alt and Honnorez, 1984). During Mg-smectite formation seawater Mg is quantitatively removed from ambient fluids. Anhydrite precipitation decreases SO₄ and Ca in the fluids. Furthermore, SO₄ is reduced to H₂S, which precipitates as massive sulfide in the basement and on the seafloor in the vicinity of hot vents. Such deposits are highly enriched in e.g. Cu, Pb, Ag, Au, and rare earth elements. During the albitization of plagioclase Ca is released from the basement and enriched in the ambient fluids.

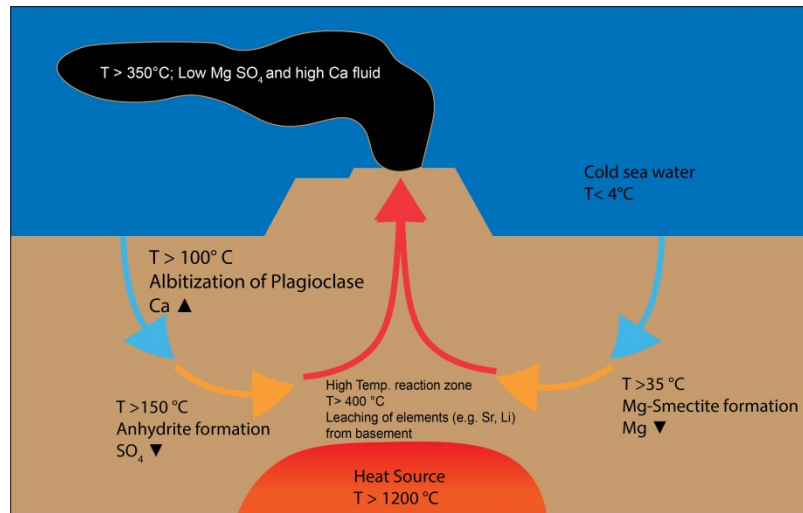


Fig. I.III Schematic sketch of hydrothermal system showing major reactions in recharge zones

Sediment-hosted hydrothermal systems can develop in areas of active magmatism with high sediment accumulation. Such areas are oceanic rifts close to land masses e.g. the Guaymas Basin, Middle Valley, Red Sea and Escanaba Trough (Herzig and Hannington, 2006). Basement alteration processes are here similar to those at unsedimented mid-oceanic spreading systems. The ascent of the fluids to the seafloor leads to interactions with the sediments, thereby the fluid signature can be highly modified. Fluids of the Guaymas Basin are for example highly enriched in methane (Berndt et al., 2016; Geilert et al., 2018). Fluids of the Escanaba Trough are in contrast enriched in alkali elements (e.g. Li, Cs and Rb) and boron (James et al., 1999). Whereas fluids of the Atlantis II deep in the Red Sea are described as brines (Hartmann, 1985). The modification of the fluids always depends on the type of the host sediments.

I.III Global Mg cycle

Magnesium is one of the major elements, which is removed from the ocean due to hydrothermal processes. In the following chapter IV, a so far unperceived Mg short term sink with a high potential of isotope fractionation will be discussed. To understand the possible consequences of the described process it is important present the Mg and $\delta^{26}\text{Mg}$ cycle in general.

Mg is the second most abundant cation in the ocean with a concentration of 53.2 mM. The residence time of this conservative element in the ocean is about 13 Ma. The present day $\delta^{26}\text{Mg}$ value is -0.8 ‰ (Teng, 2017). There are several smaller and larger sources and sinks balancing the oceanic budget. The main source of Mg to the ocean is the continental runoff

with an estimated flux of up to 5.1 Tmol yr⁻¹ (Berner and Berner, 2012) subdivided into two sources; silicate weathering (3 Tmol yr⁻¹) and carbonate weathering (2.1 Tmol yr⁻¹). The isotopic composition of these sources can vary significantly depending on the hinterland geology. If fluids are in interaction with calcium carbonate minerals they are enriched in light Mg, whereas fluids interacting with silicate rocks are more enriched in heavy Mg. This results in a broad range for the continental runoff with $\delta^{26}\text{Mg}$ values of -2.5 to +0.64 ‰ (Teng, 2017).

Groundwater discharge to the ocean is the second largest source flux and contributes about 1.8 Tmol yr⁻¹ (Dzhamalov and Safronova, 2002). The mean isotopic value of this source is -1.2 ‰ (Berg et al., 2019).

A smaller source for Mg to the ocean is the low temperature weathering of peridotite (Snow and Dick, 1995). Ligi et al. (2013) proposed that weathering of peridotites has changed the Mg budget from 80 Ma ago to modern seawater values. Based on numerical modelling results, Ligi et al. (2013) proposes a flux from peridotite weathering of up to 1.1 Tmol yr⁻¹. In contrast Liu et al. (2017) showed that only a small portion of the Mg is transferred into the ocean whereas most of the Mg is stored in Mg-rich smectite. The impact on seawater $\delta^{26}\text{Mg}$ would be that heavy Mg is stored in Mg-rich smectite (Wimpenny et al., 2014) while excess Mg remaining in the fluids is presumably enriched in light Mg.

A so far neglected source for Mg are hydrothermal vents in back arc settings which are enriched in Mg (de Ronde and Stucker, 2015). SO₂ provided by magmatic degassing, like fumaroles on land, is via disproportion transformed to H₂SO₄ and H₂S while the resulting highly acidic fluids dissolve Mg-rich minerals such as olivine resulting in SO₄ and Mg enriched hydrothermal fluids. Those fluids have been described at DESMOS Caldera off shore Papua New Guinea (Gamo et al., 1997; Seewald et al., 2015) and in the Kermadec Arc in the western Pacific Ocean (de Ronde and Stucker, 2015). Because only a few sites are described, quantification of the flux due to this process is difficult to estimate. However, de Ronde and Stucker (2015) assume that the hydrothermal emission of arc systems amounts to about 10% of the global emission of MOR systems. However, compared to the continental runoff this source seems to be rather small. Furthermore, no measured isotope data are available to date for this process. Olivine is enrichment in heavy Mg (Teng, 2017), hence this flux should have a $\delta^{26}\text{Mg}$ signature higher than seawater.

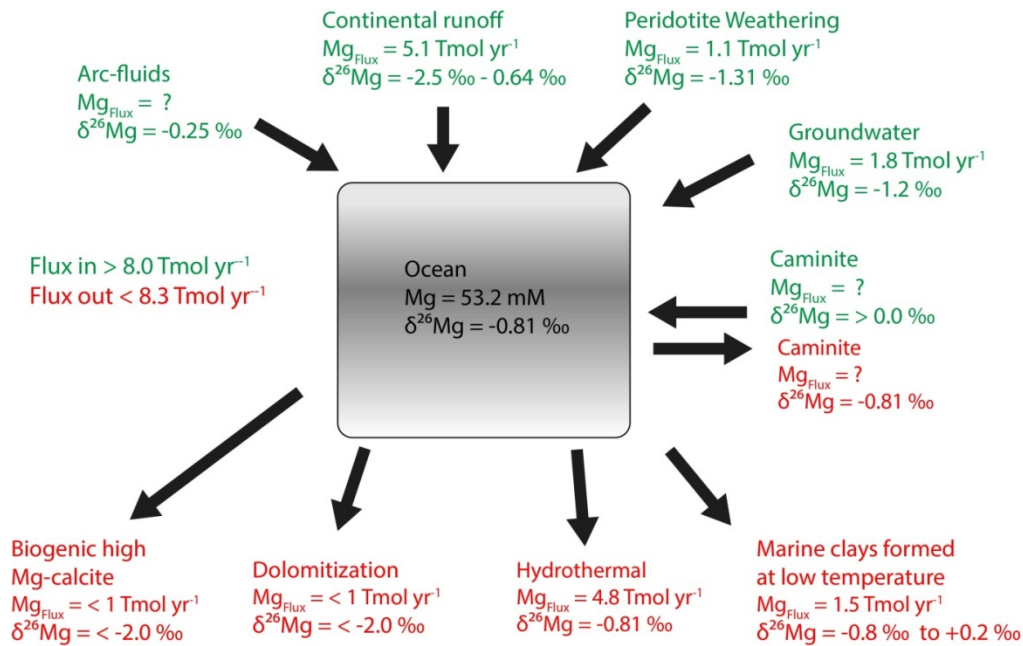


Fig. I.III Sketch for oceanic Mg and $\delta^{26}\text{Mg}$ budget for the major sources (green) and sinks (red)

In contrast, there is one main and several minor sinks for Mg in the ocean. One is the quantitative removal of Mg in hydrothermal systems where Mg is bound to clay minerals in the basement and no longer available for a reflux to the ocean. The second major sink is the dolomitization of calcium carbonate.

Hydrothermal circulation at spreading centers results in a quantitative removal of Mg from the fluids with a flux of up to 4.8 Tmol yr^{-1} (Elderfield and Schultz, 1996). Mg is transferred into Mg-rich smectite (Saponite) during alteration of the oceanic basement. Those smectite have a bulk $\delta^{26}\text{Mg}$ of $> 0\text{‰}$ (Wimpenny et al., 2014).

Another sink for Mg is the low temperature weathering of basalts and authigenic formation of clay in sediments. This process is hard to quantify as Mg-smectite formation in sediments is dependent on several external factors such as Si availability. However, Fantle and Higgins (2014) estimated that the flux of Mg is about 1.5 Tmol yr^{-1} . Isotopic composition of authigenic clays is about -0.8‰ to $+0.2\text{‰}$ indicating a strong fractionation. Formation of biogenic high Mg-calcite e.g. foraminifera, coccoliths, corals or bivalves is a minor sink in the global budget. Overall the flux is less than 1 Tmol yr^{-1} (Bernier and Bernier, 1996). On the other side isotope composition for carbonates varies strong from seawater composition, with typical values for carbonates as low as -2‰ (Saenger and Wang, 2014).

The dolomitization of calcium carbonates is a rather small sink in the modern ocean with an Mg flux into dolomite with less than 1 Tmol yr⁻¹. However, the fractionation of Mg from seawater is strong with values up to 2‰ (Teng, 2017).

Overall the flux for Mg of the sources and sinks are to some extent in balance (Fig. I.III). However, some smaller sources and sinks are so far not taken into account in global studies. Future studies should evaluate those sources, as some of them show potential for high fractionation of $\delta^{26}\text{Mg}$.

I.IV Volcanic Ash weathering

Chapter III and IV are studies on the Azores Plateau, a volcanic active region. Numerous volcanic eruptions of the Azores Archipelago deposited vast amounts of volcanic tephra and fall out at the seafloor. Weathering of the volcanic tephra can have a significant impact on ambient pore fluids (e.g. Schacht et al., 2008). Volcanic deposits consist of loose or consolidated pyroclastic fall, block and ash flow as well as tuffaceous sediments composed of volcanic glass, mineral and country rock. It has been estimated that up to 20 wt% of the sediments in the Caribbean Sea (Peters 2000) and up to 60 wt% in the Northwest Pacific (Scudder 2009, 2014) are of volcanic origin. The alteration of those deposits can result in authigenic mineral precipitation, mineral dissolution and a modification of the ambient pore fluids. Alteration of volcanoclastic sediments plays a major role in element cycling and CO₂ fixation in the global context. However, depending on the volcanic composition, weathering can have a wide range of different effects on the pore fluids (Tab. I.1).

According to Schacht (2005) the effect on pore fluids of basaltic glass alteration is characterized by the removal of Mg, Na, K and enrichments of Ca and Si. Felsic glass in contrast is enriched in trace elements, and Si, Al, Mn, Ba and Sr to Ca.

Table I.I Element enrichments from ash dissolution, smectite and zeolite formation relative to seawater

Element	Change in pore fluid composition relative to seawater
Ca	Higher for ash dissolution and smectite dissolution, over 80°C depleted due to Ca-zeolite formation, depleted when calcite is formed by ash weathering
Li	Depleted during smectite formation; enriched by volcanic ash dissolution
B	Enriched by ash dissolution
Mg	Depleted during smectite formation
Sr	Enriched by ash dissolution
Na	Depleted during smectite formation and low T (70 -80 °C) zeolite formation
K	Depleted during smectite formation and low T (70 -80 °C) zeolite formation
Si	Enriched by ash dissolution

The rate and degree of ash weathering is depending on availability of CO₂ and therefore on the input of organic matter. Even if glass alteration rates are high, the impact of the alteration can barely be observed in the pore fluids of the upper tens of meters as seawater composition overprints weathering signals (Schacht et al., 2008). With increasing depth different stages of alteration can be recognized from the authigenic mineral assemblage. Those secondary minerals are a sink for elements released during alteration. For basaltic glass the first stage is a palagonite layer on the surface. This stage is missing for felsic glass, here a direct dissolution of the glass is observed. The next stage is characterized by the formation of authigenic smectite. This reaction consumes H₂O, Li and Mg while Ca and non-radiogenic Sr is released into the ambient pore fluids. Formation of smectite starts at low temperatures and doubles the rate every 10°C. The next alteration stage is marked by the formation of zeolites at temperatures of about 70°C. First K and Na-rich zeolites (e.g. phillipsite and heulandite) and at temperatures >80°C also Ca-rich zeolites start to form (e.g. laumontite). In general this process removes K, Na, Ca, Al and Si from pore fluids.

I.V The Nubian/Eurasian plate boundary in the North Atlantic Ocean

The Nubian/Eurasian Plate Boundary also named the Azores Gibraltar Fracture Zone in the North Atlantic Ocean extends from the Azores Triple Junction in the West over 2450 km to the Gulf of Cadiz in the East. The plate boundary can be divided into three sections (Fig. I.IV). The westernmost section is marked by the 500 km long extensional regime of the Terceira Rift, running from the Mid-Atlantic Ridge in south east direction over the Azores Plateau. Based on GPS data Marques et al. (2013) proposed that the plate boundary is a diffuse area of ~150 km width. The plate boundary composes parts of the Azores Plateau and the Terceira Rift. Vogt and Jung (2004) showed that the spreading rate with 4 mm a^{-1} is the lowest spreading rate on the world to date.

East of Santa Maria Island of the Azores Archipelago the diffuse plate boundary connects with the Gloria Fault. The Gloria Fault, with 1300 km the largest segment, is marked by strike slip motion (Argus et al., 1989).

East of the Madeira-Tore Rise the Gloria Fault passes over into the 600 km long South West Iberian Margin (SWIM) faults and the Gibraltar subduction zone. The Gibraltar subduction zone enters the Atlantic Ocean from the east (Duarte et al., 2013) and builds up an accretionary wedge in the Atlantic Ocean between the Iberian Peninsula in the north and the Morocco margin in the south. Several deep rooted faults are cutting through the accretionary wedge (Zitellini et al., 2009). The SWIM faults are part of the diffuse plate boundary at the eastern end.

Seismic activity is present over the whole extent of the plate boundary. The main seismic activity is located in the Terceira Rift and the Gibraltar arc (Batista et al., 2017). The Gloria fault can produce significant earth quakes as the event with Magnitude 8.4 in 1941 (Baptista et al., 2016), one of the largest earthquakes ever recorded in a transform fault setting. Large earthquakes occurred also within the SWIM fault system in the past, e.g. the 1755 Great Lisbon Earthquake with a magnitude of $M_w > 8.5$ (Baptista et al., 1988). The Terceira Rift is characterized by smaller earthquakes with $M_w < 6$.

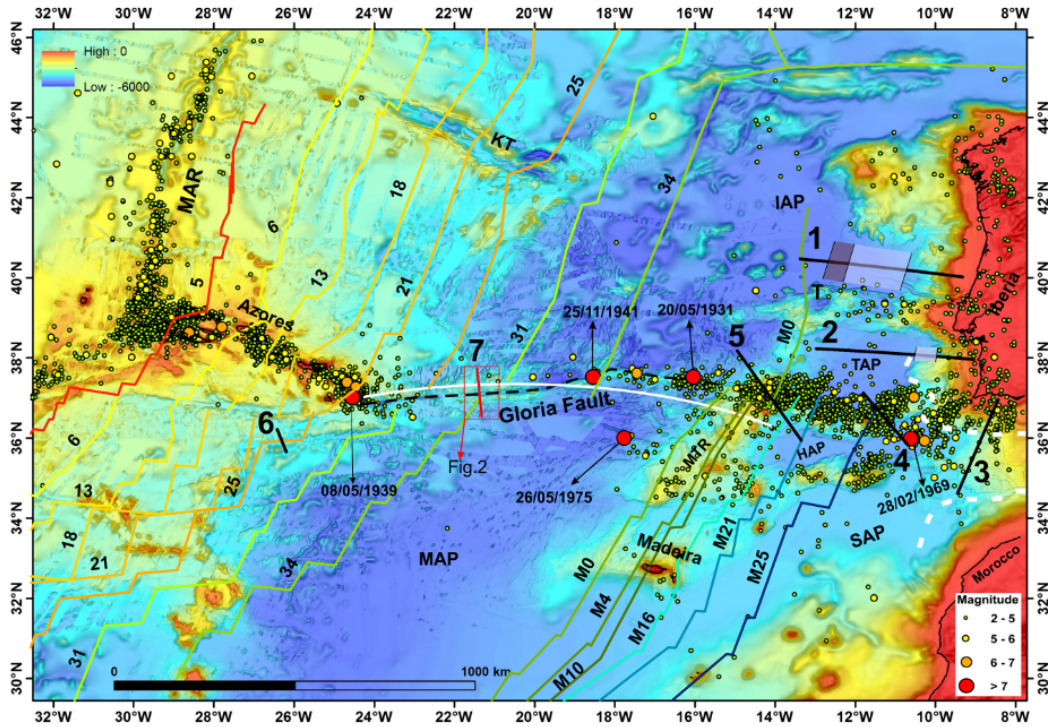


Fig. I.IV Bathymetric map of the Nubian/Eurasian plate boundary indicating seismicity from Batista et al. (2017)

Fluid expulsions are mainly described for the plate boundary at the accretionary wedge. Over 50 mud volcanoes mostly aligned along the strike slip faults are described in the literature (Gutscher et al., 2012). Within the Terceira rift only one submarine hydrothermal system was described so far (Cardigos et al., 2005). The D. João de Castro seamount hosted a shallow hydrothermal system, which seems to be inactive at present state (Beier, 2016). However, for the Gloria Fault there is a lack of data. The existence of fluid discharge is only speculative to date. Nevertheless, in similar transform faults in the North Atlantic strong signs for discharge are present (Fisher and Von Herzen, 2005), combined with the active seismicity, active fluid flow at Gloria Fault is likely to occur.

I.VI Thesis Outline

The following three chapters present standalone articles, which are published or going to be submitted to international scientific journals. They deal with fluid seeps at the eastern and western end of the Nubian/Eurasian plate boundary in the North Atlantic Ocean.

Chapter II is a model-based validation of hypothesis presented in the publication “Strike-slip faults mediate the rise of crustal-derived fluids and mud volcanism in the deep sea” by Hensen et al. (2015). Here we test the previously made statements about various fluid

sources and test if fluid circulation through altered oceanic crust could be one explanation for the fluid chemistry observed at three mud volcanoes. A 1D basin scale transport reaction model based on the framework of Burwicz and Rüpke (2019) was developed and adapted to simulate the genesis of fluids emanating through these mud volcanoes.

Chapter III and IV deal with pore fluid characterization of the Azores plateau and the Terceira rift. A first general description of pore fluids of the Azores Plateau is given in Chapter III. Here we described patterns of ash alteration and show that hydrothermal systems are active in this region. Chapter IV focuses on high Mg and SO₄ fluids of a hydrothermal system in the Terceira Rift. In this multi-element and -isotope approach, we focus on mineral dissolution and the effects on pore fluid chemistry.

Chapter II is already published in *Geochimica et Cosmochimica Acta* (Schmidt et al., 2018), chapter IV has been submitted to *G-cubed* while chapter III is being prepared for submission to *Marine Geology*.

I.VII References

- Alt, J.C., Honnorez, J., 1984. Alteration of the upper oceanic crust, DSDP site 417: mineralogy and chemistry. *Contributions to Mineralogy and Petrology* 87, 149-169.
- Argus, D.F., Gordon, R.G., Demets, C., Stein, S., 1989. Closure of the Africa-Eurasia-North America plate motion circuit and tectonics of the Gloria fault. *Journal of Geophysical Research* 94, 5585-5602.
- Baptista, M.A., Heitor, S., Miranda, J.M., Miranda, P., Mendes Vitor, L., 1988. The 1755 Lisbon tsunami; evaluation of the tsunami parameters. *Journal of Geodynamics* 25, 143-157.
- Baptista, M.A., Miranda, J.M., Batlló, J., Lisboa, F., Luis, J., Maciá, R., 2016. New study on the 1941 Gloria Fault earthquake and tsunami. *Natural Hazards and Earth System Sciences* 16, 1967-1977.
- Batista, L., Hübscher, C., Terrinha, P., Matias, L., Afilhado, A., Lüdmann, T., 2017. Crustal structure of the Eurasia–Africa plate boundary across the Gloria Fault, North Atlantic Ocean. *Geophysical Journal International* 209, 713-729.
- Beaulieu, S.E., Baker, E.T., German, C.R., Maffei, A., 2013. An authoritative global database for active submarine hydrothermal vent fields. *Geochemistry, Geophysics, Geosystems* 14, 4892-4905.
- Beier, C., 2016. Azores Plateau - Cruise No. M128 - July 2 - July 27, 2016 - Ponta Delgada (Azores, Portugal) - Ponta Delgada (Azores, Portugal), *METEOR Berichte*, p. 42.
- Berg, R.D., Solomon, E.A., Teng, F.-Z., 2019. The role of marine sediment diagenesis in the modern oceanic magnesium cycle. *Nature Communications* 10, 4371.

Berndt, C., Hensen, C., Mortera-Gutierrez, C., Sarkar, S., Geilert, S., Schmidt, M., Liebetrau, V., Kipfer, R., Scholz, F., Doll, M., 2016. Rifting under steam—How rift magmatism triggers methane venting from sedimentary basins. *Geology* 44, 767-770.

Berner, E.K., Berner, R.A., 1996. *Global environment: water, air, and geochemical cycles*. Prentice-Hall.

Berner, E.K., Berner, R.A., 2012. *Global environment: water, air, and geochemical cycles*. Princeton University Press.

Burwicz, E., Rüpke, L., 2019. Thermal State of the Blake Ridge Gas Hydrate Stability Zone (GHSZ)—Insights on Gas Hydrate Dynamics from a New Multi-Phase Numerical Model. *Energies* 12, 3403.

Calvert, A., Potts, C., 1985. Seismic evidence for hydrothermally altered mantle beneath old crust in the Tydeman fracture zone. *Earth and Planetary Science Letters* 75, 439-449.

Cannat, M., Mamaloukas-Frangoulis, V., Auzende, J.-M., Bideau, D., Bonatti, E., Honnorez, J., Lagabrielle, Y., Malavielle, J., Mevel, C., 1991. A geological cross-section of the Vema Fracture Zone transverse ridge, Atlantic Ocean. *Journal of Geodynamics* 13, 97-118.

Cardigos, F., Colaço, A., Dando, P.R., Ávila, S.P., Sarradin, P.M., Tempera, F., Conceição, P., Pascoal, A., Serrão Santos, R., 2005. Shallow water hydrothermal vent field fluids and communities of the D. João de Castro Seamount (Azores). *Chemical Geology* 224, 153-168.

de Ronde, C.E.J., Stucker, V.K., 2015. Chapter 47 - Seafloor Hydrothermal Venting at Volcanic Arcs and Backarcs, in: Sigurdsson, H. (Ed.), *The Encyclopedia of Volcanoes (Second Edition)*. Academic Press, Amsterdam, pp. 823-849.

Devey, C.W., Augustin, N., Brandt, A., Brenke, N., Köhler, J., Lins, L., Schmidt, C., Yeo, I.A., 2018. Habitat characterization of the Vema Fracture Zone and Puerto Rico Trench. *Deep Sea Research Part II: Topical Studies in Oceanography* 148, 7-20.

Duarte, J.C., Rosas, F.M., Terrinha, P., Schellart, W.P., Boutelier, D., Gutscher, M.-A., Ribeiro, A., 2013. Are subduction zones invading the Atlantic? Evidence from the southwest Iberia margin. *Geology* 41, 839-842.

Dzhamalov, R.G., Safronova, T.I., 2002. On Estimating Chemical Discharge into the World Ocean with Groundwater. *Water Resources* 29, 626-631.

Elderfield, H., Schultz, A., 1996. Mid-Ocean Ridge hydrothermal fluxes and the chemical composition of the ocean. *Annual Review of Earth and Planetary Sciences* 24, 191-224.

Fantle, M.S., Higgins, J., 2014. The effects of diagenesis and dolomitization on Ca and Mg isotopes in marine platform carbonates: implications for the geochemical cycles of Ca and Mg. *Geochimica et Cosmochimica Acta* 142, 458-481.

Fehn, U., Snyder, G.T., Matsumoto, R., Muramatsu, Y., Tomaru, H., 2003. Iodine dating of pore waters associated with gas hydrates in the Nankai area, Japan. *Geology* 31, 521-524.

Feseker, T., Brown, K.M., Blanchet, C., Scholz, F., Nuzzo, M., Reitz, A., Schmidt, M., Hensen, C., 2010. Active mud volcanoes on the upper slope of the western Nile deep-sea fan - first results from the P362/2 cruise of R/V Poseidon. *Geo-Marine Letters* 30, 169-186.

Fisher, A.T., Von Herzen, R.P., 2005. Models of hydrothermal circulation within 106 Ma seafloor: Constraints on the vigor of fluid circulation and crustal properties, below the Madeira Abyssal Plain. *Geochemistry, Geophysics, Geosystems* 6.

Fitts, T.G., Brown, K.M., 1999. Stress-induced smectite dehydration: ramifications for patterns of freshening and fluid expulsion in the N. Barbados accretionary wedge. *Earth and Planetary Science Letters* 172, 179-197.

Gamo, T., Okamura, K., Charlou, J.-L., Urabe, T., Auzende, J.-M., Ishibashi, J., Shitashima, K., Chiba, H., 1997. Acidic and sulfate-rich hydrothermal fluids from the Manus back-arc basin, Papua New Guinea. *Geology* 25, 139-142.

Geilert, S., Hensen, C., Schmidt, M., Liebetrau, V., Scholz, F., Doll, M., Deng, L., Fiskal, A., Lever, M.A., Su, C.-C., 2018. On the formation of hydrothermal vents and cold seeps in the Guaymas Basin, Gulf of California. *Biogeosciences* 15, 5715-5731.

Gutscher, M.-A., Dominguez, S., Westbrook, G.K., Le Roy, P., Rosas, F., Duarte, J., Terrinha, P., Miranda, J., Graindorge, D., Gailler, A., 2012. The Gibraltar subduction: A decade of new geophysical data. *Tectonophysics* 574, 72-91.

Haeckel, M., Suess, E., Wallmann, K., Rickert, D., 2004. Rising methane gas bubbles form massive hydrate layers at the seafloor. *Geochimica et Cosmochimica Acta* 68, 4335-4354.

Haffert, L., Haeckel, M., Liebetrau, V., Berndt, C., Hensen, C., Nuzzo, M., Reitz, A., Scholz, F., Schönfeld, J., Perez-Garcia, C., Weise, S.M., 2013. Fluid evolution and authigenic mineral paragenesis related to salt diapirism - The Mercator mud volcano in the Gulf of Cadiz. *Geochimica et Cosmochimica Acta* 106, 261-286.

Hantschel, T., Kauerauf, A.I., 2009. *Fundamentals of basin and petroleum systems modeling*. Springer Science & Business Media.

Hartmann, M., 1985. Atlantis-II Deep geothermal brine system. Chemical processes between hydrothermal brines and Red Sea deep water. *Marine Geology* 64, 157-177.

Hayes, D.E., Pimm, A.C., Beckmann, J.P., Benson, W.E., Berger, W.H., Roth, P.H., Supko, P.R., von Rad, U., 1972. Site 135, DSDP, Initial Reports U.S. Government Printing Office, Washington, D.C, pp. 15-48.

Hensen, C., Duarte, J.C., Vannucchi, P., Mazzini, A., Lever, M.A., Terrinha, P., Géli, L., Henry, P., Villinger, H., Morgan, J., Schmidt, M., Gutscher, M.-A., Bartolome, R., Tomonaga, Y., Polina, A., Gràcia, E., Tinivella, U., Lupi, M., Çağatay, N., Elvert, M., Sakellariou, D., Matias, L., Kipfer, R., Karageorgis, A.P., Ruffine, L., Liebetrau, V., Pierre, C., Schmidt, C., Batista, L., Gasperini, L., Burwicz, E., Neres, M., Nuzzo, M., 2019. Marine Transform Faults and Fracture Zones: A Joint Perspective Integrating Seismicity, Fluid Flow and Life. *Frontiers in Earth Science* 7.

Hensen, C., Nuzzo, M., Hornibrook, E., Pinheiro, L.M., Bock, B., Magalhães, V.H., Brückmann, W., 2007. Sources of mud volcano fluids in the Gulf of Cadiz - indications for hydrothermal imprint. *Geochimica et Cosmochimica Acta* 71, 1232-1248.

Hensen, C., Scholz, F., Nuzzo, M., Valadares, V., Gràcia, E., Terrinha, P., Liebetrau, V., Kaul, N., Silva, S., Martínez-Loriente, S., Bartolome, R., Piñero, E., Magalhães, V.H., Schmidt, M., Weise, S.M., Cunha, M., Hilario, A., Perea, H., Rovelli, L., Lackschewitz, K.,

2015. Strike-slip faults mediate the rise of crustal-derived fluids and mud volcanism in the deep sea. *Geology* 43, 339-342.
- Hensen, C., Wallmann, K., 2005. Methane formation at Costa Rica continental margin - constraints for gas hydrate inventories and cross-décollement fluid flow. *Earth and Planetary Science Letters* 236, 41-60.
- Herzig, P.M., Hannington, M.D., 2006. Input from the deep: Hot vents and cold seeps, *Marine geochemistry*. Springer, pp. 457-479.
- James, R.H., Rudnicki, M.D., Palmer, M.R., 1999. The alkali element and boron geochemistry of the Escanaba Trough sediment-hosted hydrothermal system. *Earth and Planetary Science Letters* 171, 157-169.
- Kastner, M., Elderfield, H., Martin, J.B., 1991. Fluids in convergent margins: what do we know about their composition, origin, and role in diagenesis and importance for oceanic chemical fluxes? *Phil. Trans. R. Soc. London, Ser. A* 335, 243-259.
- Kopf, A., 2002. Significance of mud volcanism. *Reviews of Geophysics* 40, 1-52.
- Ligi, M., Bonatti, E., Cuffaro, M., Brunelli, D., 2013. Post-Mesozoic rapid increase of seawater Mg/Ca due to enhanced mantle-seawater interaction. *Scientific reports* 3.
- Linke, P., Wallmann, K., Suess, E., Hensen, C., Rehder, G., 2005. In-situ benthic fluxes from an intermittently active mud volcano at the Costa Rica convergent margin. *Earth and Planetary Science Letters* 235, 79-95.
- Liu, P.-P., Teng, F.-Z., Dick, H.J.B., Zhou, M.-F., Chung, S.-L., 2017. Magnesium isotopic composition of the oceanic mantle and oceanic Mg cycling. *Geochimica et Cosmochimica Acta* 206, 151-165.
- Marques, F., Catalão, J., DeMets, C., Costa, A., Hildenbrand, A., 2013. GPS and tectonic evidence for a diffuse plate boundary at the Azores Triple Junction. *Earth and Planetary Science Letters* 381, 177-187.
- Martin, J.B., Gieskes, J.M., Torres, M., Kastner, M., 1993. Bromine and iodine in Peru margin sediments and pore fluids: Implications for fluid origins. *Geochimica et Cosmochimica Acta* 57, 4377-4389.
- Mazzini, A., Etiope, G., 2017. Mud volcanism: An updated review. *Earth-Science Reviews* 168, 81-112.
- Milkov, A.V., 2000. Worldwide distribution of submarine mud volcanoes and associated gas hydrates. *Marine Geology* 167, 29-42.
- Nielsen, S.G., Rehkämpfer, M., Teagle, D.A.H., Butterfield, D.A., Alt, J.C., Halliday, A.N., 2006. Hydrothermal fluid fluxes calculated from the isotopic mass balance of thallium in the ocean crust. *Earth and Planetary Science Letters* 251, 120-133.
- Potts, C., Calvert, A., White, R., 1986. Crustal structure of Atlantic fracture zones-III. The Tydeman fracture zone. *Geophysical Journal International* 86, 909-942.

- Reitz, A., Haeckel, M., Wallmann, K., Hensen, C., Heeschen, K., 2007. Origin of salt-enriched pore fluids in the northern Gulf of Mexico. *Earth and Planetary Science Letters* 259, 266-282.
- Saenger, C., Wang, Z., 2014. Magnesium isotope fractionation in biogenic and abiogenic carbonates: implications for paleoenvironmental proxies. *Quaternary Science Reviews* 90, 1-21.
- Sahling, H., Bohrmann, G., Spiess, V., Bialas, J., Breitzke, M., Ivanov, M., Kasten, S., Krastel, S., Schneider, R.R., 2008. Pockmarks in the Northern Congo Fan area, SW Africa: Complex seafloor features shaped by fluid flow. *Marine Geology* 249, 206-225.
- Schacht, U., 2005. Alteration of volcanic glasses in marine sediments: Laboratory experiments and field studies. CAU, Kiel.
- Schacht, U., Wallmann, K., Kutterolf, S., Schmidt, M., 2008. Volcanogenic sediment-seawater interactions and the geochemistry of pore waters. *Chemical Geology* 249, 321-338.
- Schmidt, C., Burwicz, E., Hensen, C., Wallmann, K., Martinez-Loriente, S., Gracia, E., 2018. Genesis of mud volcano fluids in the Gulf of Cadiz using a novel basin-scale model approach. *Geochim Cosmochim Acta* 243, 186-204.
- Schmidt, M., Hensen, C., Mörz, T., Müller, C., Grevemeyer, I., Wallmann, K., Mau, S., Kaul, N., 2005. Methane hydrate accumulation in "Mound 11" mud volcano, Costa Rica forearc. *Marine Geology* 216, 83-100.
- Scholz, F., 2009. Pore water expulsion at submarine cold seeps: geochemical evidence for short cuts between crust, sediment and ocean Christian Albrechts Universität Kiel, p. 116.
- Scholz, F., Hensen, C., De Lange, G.J., Haeckel, M., Liebetrau, V., Meixner, A., Reitz, A., Romer, R.L., 2010. Lithium isotope geochemistry of marine pore waters - Insights from cold seep fluids. *Geochimica et Cosmochimica Acta* 74, 3459-3475.
- Scholz, F., Hensen, C., Reitz, A., Romer, R.L., Liebetrau, V., Meixner, A., Weise, S.M., Haeckel, M., 2009. Isotopic evidence ($^{87}\text{Sr}/^{86}\text{Sr}$, $\delta^7\text{Li}$) for alteration of the oceanic crust at deep-rooted mud volcanoes in the Gulf of Cadiz, NE Atlantic Ocean. *Geochimica et Cosmochimica Acta* 73, 5444-5459.
- Seewald, J.S., Reeves, E.P., Bach, W., Saccocia, P.J., Craddock, P.R., Shanks, W.C., Sylva, S.P., Pichler, T., Rosner, M., Walsh, E., 2015. Submarine venting of magmatic volatiles in the Eastern Manus Basin, Papua New Guinea. *Geochimica et Cosmochimica Acta* 163, 178-199.
- Shipley, T.H., Stoffa, P.L., Dean, D.F., 1990. Underthrust sediments, fluid migration paths, and mud volcanoes associated with the accretionary wedge off Costa Rica: Middle America Trench. *Journal of Geophysical Research* 95, 8743-8752.
- Snow, J.E., Dick, H.J., 1995. Pervasive magnesium loss by marine weathering of peridotite. *Geochimica et Cosmochimica Acta* 59, 4219-4235.
- Stein, C.A., Stein, S., Pelayo, A., 1995. Heat flow and hydrothermal circulation, in: Humphris, S.E., Zierenberg, R.A., Mullineaux, L.S., Thomson, R.E. (Eds.), *Seafloor hydrothermal systems: physical, chemical, biological, and geological interactions*. American Geophysical Union, Washington DC, pp. 425-445.

- Suess, E., Carson, B., Ritger, S.D., Moore, J.C., Jones, M.L., Kulm, L.D., Cochrane, G.R., 1985. Biological communities at vent sites along the subduction zone off Oregon, in: Jones, M.L. (Ed.), *The Hydrothermal Vents of the Eastern Pacific: An Overview*. Bull. Biol. Soc. Wash., pp. 475-484.
- Suess, E., Torres, M., Bohrmann, G., Collier, R.W., Greinert, J., Linke, P., Rheder, G., Trehu, A., Wallmann, K., Winckler, G., Zuleger, E., 1999. Gas hydrate destabilization: Enhanced dewatering, benthic material turnover and large methane plumes at the Cascadia convergent margin. *Earth and Planetary Science Letters* 170, 1-15.
- Teng, F.-Z., 2017. Magnesium Isotope Geochemistry. *Reviews in Mineralogy and Geochemistry* 82, 219-287.
- Torres, M., Wallmann, K., Trehu, A., Bohrmann, G., Borowski, W., Tomaru, H., 2004. Gas hydrate growth, methane transport, and chloride enrichment at the southern summit of Hydrate Ridge, Cascadia margin off Oregon. *Earth and Planetary Science Letters* 226, 225-241.
- Vogt, P., Cherkashev, G., Ginsburg, G., Ivanov, G., Milkov, A., Crane, K., Sundvor, A., Pimenov, N., Egorov, A., 1997. Haakon Mosby mud volcano provides unusual example of venting. *EOS, Transactions American Geophysical Union* 78, 549-557.
- Vogt, P.R., Jung, W.Y., 2004. The Terceira Rift as hyper-slow, hotspot-dominated oblique spreading axis: A comparison with other slow-spreading plate boundaries. *Earth and Planetary Science Letters* 218, 77-90.
- Wallmann, K., Drews, M., Aloisi, G., Bohrmann, G., 2006. Methane discharge into the Black Sea and the global ocean via fluid flow through submarine mud volcanoes. *Earth and Planetary Science Letters* 248, 544-559.
- Wallmann, K., Riedel, M., Hong, W.L., Patton, H., Hubbard, A., Pape, T., Hsu, C.W., Schmidt, C., Johnson, J.E., Torres, M.E., Andreassen, K., Berndt, C., Bohrmann, G., 2018. Gas hydrate dissociation off Svalbard induced by isostatic rebound rather than global warming. *Nature Communications* 9, 83.
- Wallmann, K., Suess, E., Westbrook, G.H., Winckler, G., Cita, M.B., MEDRIFF-consortium, 1997. Salty brines on the Mediterranean sea floor. *Nature* 387, 31-32.
- Westbrook, G., Smith, M., 1983. Long decollements and mud volcanoes: Evidence from the Barbados Ridge Complex for the role of high pore-fluid pressure in the development of an accretionary complex. *Geology* 11, 279-283.
- Wimpenny, J., Colla, C.A., Yin, Q.-Z., Rustad, J.R., Casey, W.H., 2014. Investigating the behaviour of Mg isotopes during the formation of clay minerals. *Geochimica et Cosmochimica Acta* 128, 178-194.
- Xu, W., Germanovich, L.N., 2006. Excess pore pressures resulting from methane hydrate dissociation in marine sediments: A theoretical approach. *Journal of Geophysical Research* 111, doi:10.1029/2004JB003600.
- Zitellini, N., Gràcia, E., Matias, L., Terrinha, P., Abreu, M.A., DeAlteriis, G., Henriët, J.P., Dañobeitia, J.J., Masson, D.G., Mulder, T., Ramella, R., Somoza, L., Diez, S., 2009. The quest for the Africa-Eurasia plate boundary west of the Strait of Gibraltar. *Earth and Planetary Science Letters* 280, 13-50.

II. Genesis of mud volcano fluids in the Gulf of Cadiz using a novel basin-scale model approach

Christopher Schmidt^a, Ewa Burwicz^a, Christian Hensen^a, Klaus Wallmann^a, Sara Martínez-Loriente^{b,c},
Eulàlia Gràcia^c

^aGEOMAR Helmholtz Centre for Ocean Research Kiel, Wischhofstr. 1-3, 24148 Kiel, Germany

^biCRAG (Irish Centre for Research in Applied Geosciences), UCD School of Earth Sciences, Belfield, Dublin 4, Ireland

^cB-CSI, Institut de Ciències del Mar, CSIC, Pg. Marítim de la Barceloneta, 37-49, 08003 Barcelona, Spain

Published in 2018 *Geochimica et Cosmochimica Acta*, v. 243, p. 186 -204

Abstract

Mud Volcanism and fluid seepage are widespread phenomena in the Gulf of Cadiz (SW Iberian Margin). In this seismically active region located at the boundary between the African and Eurasian plates, fluid flow is typically focused on deeply rooted active strike-slip faults. The geochemical signature of emanating fluids from various mud volcanoes (MVs) has been interpreted as being largely affected by clay mineral dehydration and recrystallization of Upper Jurassic carbonates. Here we present the results of a novel, fully-coupled 1D basin-scale reactive-transport model capable of simulating major fluid forming processes and related geochemical signatures by considering the growth of the sediment column over time, compaction of sediments, diffusion and advection of fluids, as well as convective and conductive heat flow. The outcome of the model is a realistic approximation to the development of the sediment pore water system over geological time scales in the Gulf of Cadiz. Combined with a geochemical reaction transport model for clay mineral dehydration and calcium carbonate recrystallization, we were able to reproduce measured concentrations of Cl, strontium and $^{87}\text{Sr}/^{86}\text{Sr}$ of emanating mud volcano fluids. These results support previously made qualitative interpretations and add further constraints on fluid forming processes, reaction rates and source depths. The geochemical signature at Porto MV posed a specific problem, because of insufficient constraints on non-radiogenic $^{87}\text{Sr}/^{86}\text{Sr}$ sources at this location. We favour a scenario of basement-derived fluid injection into basal Upper Jurassic carbonate deposits (Hensen et al., 2015). Although the mechanism behind such basement-derived flow, e.g. along permeable faults, remains speculative at this stage, it provides an additional source of low $^{87}\text{Sr}/^{86}\text{Sr}$ fluids and offers an idea on how formation water from the deepest sedimentary strata above the basement can be mobilized and eventually initiate the advection of fluids feeding MVs at the seafloor. The dynamic reactive-transport model presented in this study provides a new tool addressing the combined simulation of complex physical-geochemical processes in sedimentary systems. The model can easily be extended and applied to similar geological settings, and thus help us to provide a fundamental understanding of fluid dynamics and element recycling in sedimentary basins.

II.1 Introduction

Fluid seepage and mud volcanoes (MVs) have been ubiquitously observed on- and offshore on earth. Several thousand MVs worldwide have been described in diverse tectonic environments. To date, the majority of these features are located in compressional tectonics settings (e.g. Kopf, 2002; Mazzini and Etiope, 2017; Milkov, 2000). Cold seeps and MVs play an important role for the global element budget of hydrocarbons, such as CO₂ and CH₄ and some other major elements such as Sr, B or Li (Kopf, 2003; Milkov et al., 2003). The emanated fluid composition of MVs typically differs from seawater (Kopf, 2002). However, deviations from seawater are not uniform and vary according to underlying processes, such as the transformation of clay minerals (Hensen et al., 2004; Kastner et al., 1991), microbial mineralization of organic matter (Fehn et al., 2007; Martin et al., 1993; Tomaru et al., 2007), high temperature interactions with sediment and rocks (Martin et al., 1991; Mazzini et al., 2017), dissolution and recrystallization of carbonates (Castellini et al., 2006; Luff and Wallmann, 2003; Martin et al., 1996), formation and dissociation of gas hydrates (Hensen et al., 2004; 2007 ; Kopf, 2002; Paull et al., 2015), and rise of salt-diapirs and dissolution of evaporites (Charlou et al., 2003; Haffert et al., 2013; Reitz et al., 2007).

During the last two decades numerous multidisciplinary studies have been carried out to better understand mud volcanism and underlying processes in the Gulf of Cadiz (GoC; Fig. II.1; Bartolome et al., 2012; Gràcia et al., 2003a, b, 2010; Haffert et al., 2013; Hensen et al., 2007; 2015; Martínez-Loriente et al., 2013; 2018; Medialdea et al., 2009; Nuzzo et al., 2009; Pinheiro et al., 2003; Scholz et al., 2009; 2010a; 2010b; Somoza et al., 2003; Toyos et al., 2016). Here, most of the known MVs are found along lineaments crossing the accretionary wedge, e.g. Captain Arutyunov MV (CAMV) or Porto MV (Fig. II.1). Only a few MVs, including Abzu MV, Tiamat MV, and M. Ivanov MV (also referred as ATI MVs), were discovered along a major strike-slip fault system outside the accretionary wedge (Fig. II.1), and hence outside their typical tectonic setting (Hensen et al., 2015).

In general, most of the MVs on the accretionary wedge show a strong dilution of conservative elements, e.g. Cl compared to modern seawater (Haffert et al., 2013; Hensen et al., 2007; 2015 ; Scholz et al., 2009). In combination with a characteristic $\delta^{18}\text{O}/\delta\text{D}$ signature, the pore water freshening is a clear indicator for clay mineral dehydration (i.e. smectite to illite transformation; Hensen et al., 2015). Clay mineral dehydration is most pronounced on the upper continental margin and decreasing westward (Scholz et al., 2010b). Some MVs on the upper slope show highly enriched Cl concentrations due to the dissolution of evaporites

(e.g. CAMV and Mercator MV in Fig. II.1; Haffert et al., 2013; Hensen et al., 2007). MVs in the west of the GoC, such as ATI MVs and Porto MV show higher δD and lower $\delta^{18}O$ values accompanied by a strong enrichment of Sr with a low Sr isotope ratio. These findings have been interpreted as recrystallization of carbonates (Hensen et al., 2015).

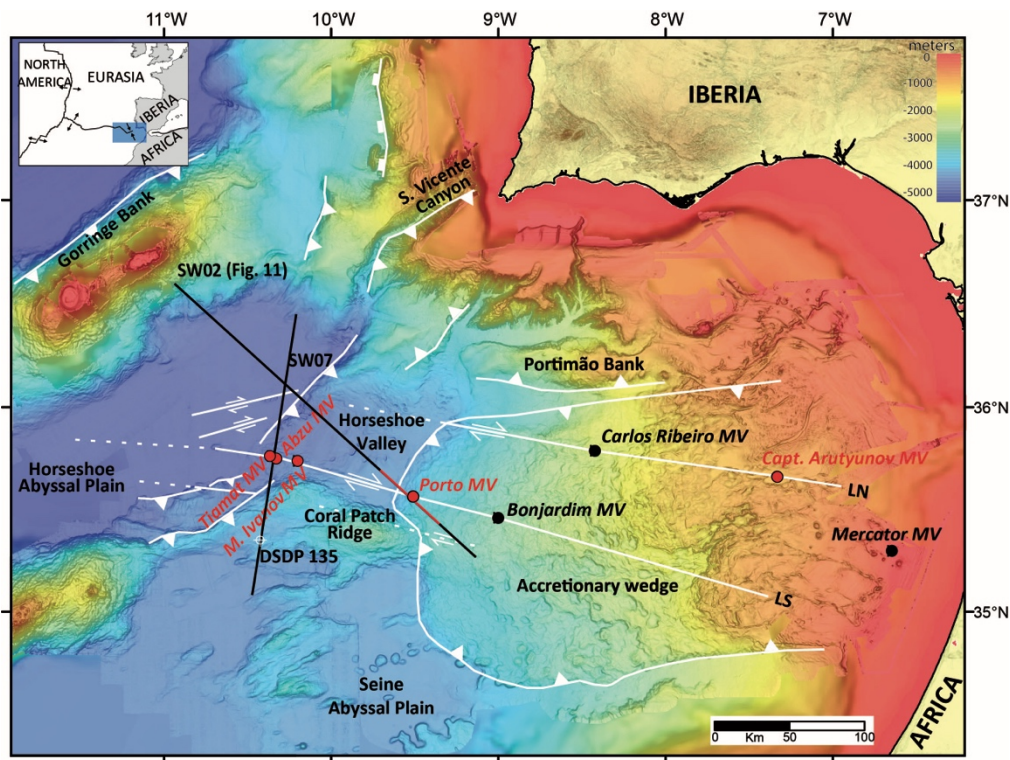


Figure II.1: Bathymetric map (modified after Hensen et al., 2015) of the Gulf of Cadiz and the surrounding areas in the NE Atlantic Ocean from a ~ 90 m digital grid (Zitellini et al., 2009). White lines depict the main tectonic features in the region LS: lineament south; LN: lineament north (Bartolome et al., 2012). Black circles represent some selective MVs, while red circles label the 5 representative MVs used in this study. Black lines represent the seismic line SW02 (Martínez-Loriente et al., 2018) across the Horseshoe abyssal plain and over Porto MV, and seismic line SW07 (Hensen et al., 2015) across ATI MVs and DSDP site 135.

To explain the fluid composition observed at Porto MV the advection of crustal derived fluids with $^{87}Sr/^{86}Sr$ ratios of 0.704 or below has been hypothesized (Hensen et al., 2015; Scholz et al., 2009). Fluid advection through oceanic crust of an age older than 140 Ma is a process that has not been verified by geochemical evidence of active seepage up to date. Results of previous studies (e.g. Stein et al., 1995) propose that fluid advection in oceanic crust older than ≈ 65 Ma is usually inhibited by thick layers of impermeable sediments accumulating over an old oceanic crust. However, Von Herzen (2004) showed that fluid advection along strong topographic contrasts in the crust is possible in oceanic crust older than 65 Ma. Furthermore, seismic studies at the Tydeman fracture zone in the tropical Atlantic Ocean (e.g. Calvert and Potts, 1985) indicate that fluid flow through several faults

affecting oceanic crust older than 80 Ma maybe still active, and Fisher and Von Herzen (2005) show evidence for fluid advection in 106 Ma old oceanic crust of the Madeira Abyssal Plain.

The approach of the current manuscript is to use numerical methods to improve a general, quantitative understanding of fluid formation processes in sedimentary basins related to geochemical processes and the potential role of fluid advection through old oceanic crust. Mud volcano fluids typically provide a window into the processes occurring underneath. To date, however, interpretations were mostly based on conventional methods only, such as property-property plots of fluid data or simple numerical models used to draw conclusions about fluid sources or fluid advection rates in surface sediments. To overcome this lack of knowledge, we designed a novel, basin-scale reactive transport model to simulate and quantify important fluid forming processes, such as the ubiquitous smectite to illite transformation, constrained by geochemical tracers in the pore fluid. The procedure described below enables the determination of the quantitative interaction of major processes affecting pore fluid geochemistry, and provides a more reliable approximation to the formation at depth of mud volcano fluids and their implications for processes that induce upward advection.

II.2 Geological setting of the Gulf of Cadiz

The GoC, located SW of the Iberian Peninsula in the NE Atlantic Ocean, has undergone a complex tectonic history (Maldonado et al., 1999). The opening of the Central Atlantic Ocean in the Early Jurassic (e.g. Rovere et al., 2004), represented the development from a passive continental margin into a convergent margin (Duarte et al., 2013; Gràcia et al., 2003b). The WNW - ESE running South West Iberian Margin (SWIM) fault system, a diffusive deep rooted strike-slip fault system (Bartolome et al., 2012), marks the boundary between the African and Eurasian plates (Zitellini et al., 2009). The convergence between the African and Eurasian plates in the GoC started in the Oligocene and continues with a present-day convergence of 4 to 5 mm a⁻¹ (Argus et al., 1989; Schettino and Turco, 2009). In the late Tortonian, the progression of the Gibraltar Arc into the Atlantic Ocean, and the coeval subduction and detachment of the oceanic plate in the Alboran Sea (Wortel and Spakman, 2000), caused the development of a U-shaped accretionary wedge in the GoC (Duarte et al., 2013). Numerous authors suggested that the progression of the arc into the Atlantic Ocean ceased at the beginning of the Pliocene (e.g. Lonergan and White, 1997). However, Gutscher et al. (2012) suggested that subduction remained active until today. The main tectonic

structures identified in the GoC are NE-SW trending thrust faults (Gràcia et al., 2003b; Martínez-Loriente et al., 2013; 2018; Zitellini et al., 2004), and WNW-ESE trending strike-slip faults (Bartolome et al., 2012; Martínez-Loriente et al., 2013; 2018; Terrinha et al., 2009; Zitellini et al., 2009). The GoC is a seismically active region where two large earthquakes occurred in the last 300 years. For instance, the 1755 the great Lisbon earthquake with an estimated magnitude of $M_w > 8.5$, which combined with a destructive tsunami devastated the city of Lisbon (Baptista et al., 1988). The most recent great earthquake occurred in 1969, in the Horseshoe Abyssal Plain with a magnitude of about $M_w = 7.9-8.0$ (Fukao, 1973). A total of eight events of great magnitude ($M_w \sim 8$) occurred in the area during the Holocene (Gràcia et al., 2010).

The seismo-stratigraphic interpretation of the GoC and the Horseshoe abyssal plain is based on the results of the DSDP Site 135 on the Coral Patch Ridge (Fig. II.1; Hayes et al., 1972). By using multichannel seismic profiles of the SWIM dataset, Martínez-Loriente et al. (2013) defined the seismo-stratigraphy of six main units. The uppermost unit I is composed of Upper Oligocene to Quaternary age sediments. Unit II is characterized by terrigenous sediments from Upper Cretaceous to Lower Eocene age. Units III – IV are built-up of terrigenous sediments from Cretaceous and Lower Cretaceous. Unit V, contain Upper Jurassic carbonates, which are underlain by the basement (Unit VI). The basement is composed of different domains, however, below the area of ATI MVs, the oceanic crust is of Early Jurassic age (Martínez-Loriente et al., 2014). All units highly vary in their thickness. On the basis of geochemical findings, the 10 km thick accretionary wedge (Gutscher et al., 2009) on the easternmost part of the GoC is built mainly of terrigenous material, with no evidence of Upper Jurassic carbonates underneath (Hensen et al., 2015).

II.3 Reactive-transport model

II.3.1 General concept

In this study, we present a newly developed vertical 1D fully-coupled basin-scale reaction-transport model. We approximately reconstruct the sedimentary sequences with their physical properties over time. The reaction-transport part accounts for clay mineral dehydration and carbonate recrystallization, as well as the advection of fluids through aged oceanic crust. Overall, five dissolved (Ca, Cl, K, Na, Sr, and ^{87}Sr) and four solid (smectite, illite, carbonate, strontium) species are considered in the model. We used MATLAB R2014a

(The MathWorks Inc.) to implement the non-steady-state model. An advantage of this model is the adaptive numerical mesh, which simulates the growing sediment column over time with a progressive compaction of the sediments. With this method, we are able to simulate the spatial and temporal evolution of the sedimentary sequences of the GoC. The governing transport equations as well as temperature and pressure equations of the model approach can be found in the appendix A.

II.3.2 Reaction solver

II.3.2.1 Clay dehydration

A widespread dehydration reaction causing substantial pore fluid freshening in marine sediments is the transformation of smectite to illite (Brown et al., 2001). Freshening is caused by the release of interlayer H₂O, which typically ranges from 20 to 25 wt% of the minerals (Fitts and Brown, 1999). Numerous studies, mostly based on deep ODP/IODP drilling data and MV fluids, have shown that this dehydration process causes dilution of conservative elements, e.g. Cl and the release of fluid mobile elements like Li, B and Sr (Chan and Kastner, 2000; Scholz et al., 2009; 2010a). The usual temperature range for this process appears to be between 60°C and 150°C (Hensen et al., 2004; Kastner et al., 1991). For this reaction, various numerical models have been described in the literature. In this study, we use a modified model by Cuadros and Linares (1996) where the reaction rate is defined as:

$$R_{Clay} = S^\alpha * (K^+)^\beta * k \quad (II.1)$$

where S- *smectite* / (*smectite* + *illite*), K⁺- dissolved concentration of K, α and β -rate order parameters for smectite and K, and k- depth dependent rate constant. In contrast to Cuadros (2006), we used an Arrhenius type, temperature dependent reaction rate which reads as follows:

$$k = A * \exp\left(-\frac{E}{R*(T+273.15)}\right) \quad (II.2)$$

where A- frequency factor, E- activation energy, and R- universal gas constant.

The amount of Sr released into the pore fluid is determined after following equation:

$$R_{Sr} = \frac{R_{Clay}}{100} * \rho_s * \left(\frac{1-\theta}{\theta}\right) * 10^6 * M_{Smectite} * X_{Sr} \quad (II.3)$$

where R_{clay} is the reaction rate of Eq. II.1 in (wt %), the factor of 10^6 is introduced to achieve the unit of μM , M_{Smectite} is the molar weight of smectite and X_{Sr} is the portion described as a ratio of Sr in smectite.

II.3.2.2 Carbonate recrystallization

At seafloor pressure and temperature conditions marine carbonate deposits typically undergo a process called recrystallization. This process includes micro-solution and precipitation of carbonates to transfer the carbonate phase into a thermodynamic more stable state (Morse and Mackenzie, 1990). This process has been inferred from observations made on DSDP/ODP drill cores; most notably, the increase of Sr in ambient pore water after deposition (Fantle, 2015; Fantle and DePaolo, 2006; Richter and DePaolo, 1987). Obviously, biogenic carbonates undergo a transformation into a more stable form of calcite. While the composition and texture are largely maintained (Baker et al., 1982), grain growth is concomitant (Morse and Casey, 1988).

For our numerical model approach we adapted a kinetic rate for Sr release due to the recrystallization of bulk carbonate as suggested by Richter and DePaolo (1987):

$$\frac{\delta C_{\text{Sr}}}{\delta t} = \left(ds * \frac{(1-\theta)}{\theta} \right) * R_{\text{age}} * (C_s - K * C_f) \quad (\text{II.4})$$

where C_{Sr} - concentration of Sr released into the pore fluid, C_s and C_f - concentrations of Sr in solid and in fluid respectively, R_{age} - rate parameter, and K - effective distribution coefficient. For numerical reasons we could not use the carbonate concentrations directly. Therefore, we implemented an additional solid species called Sr concentration of carbonates in the model.

The rate parameter for the recrystallization reads as follows

$$R_{\text{age}} = R_{\alpha} + R_{\beta} * \exp\left(\frac{-\text{age}}{R_{\gamma}}\right) \quad (\text{II.5})$$

in 1/Ma where R_{α} , R_{β} and R_{γ} are model constants, and age is the sediment age. R_{α} is the parameter that controls the long-term recrystallization where R_{β} and R_{γ} control the early recrystallization.

II.3.2.3 Fluid injection from basement

The injection from the basement into the basal sediment column for the Porto case study in scenario 4 is solved by using the pressure solver of the numerical model. When activated, at each time step an additional water mass, in $\text{kg s}^{-1} \text{m}^{-2}$, was injected with a distinct

chemical composition to the lowermost model knot. In the following time step, this pressure pulse starts to be equilibrated resulting in an additional advective component in the model column.

II.3.2.4 Strontium isotopes

The strontium isotopic ratio of $^{87}\text{Sr}/^{86}\text{Sr}$ is calculated after Hoefs (2004)

$$\Phi_{87} = \frac{{}^{87}\text{Sr}}{{}^{84}\text{Sr}+{}^{85}\text{Sr}+{}^{86}\text{Sr}+{}^{87}\text{Sr}} = \frac{{}^{87}\text{Sr}}{\text{Sr}} = \frac{R_{87}}{9.43 + R_{87}} \quad (\text{II.6})$$

with Φ_{87} - mol fraction of ^{87}Sr , R_{87} - ratio of $^{87}\text{Sr}/^{86}\text{Sr}$, and the constant 9.43 is defined by the abundance of other Sr isotopes. Due to the fact that the ratio of $^{87}\text{Sr}/^{86}\text{Sr}$ cannot be transported as a species, the bulk concentration of Sr, as well as ^{87}Sr are handled separately in the model domain. From the geological record of $^{87}\text{Sr}/^{86}\text{Sr}$ in marine carbonates (McArthur et al., 2001), the concentration of ^{87}Sr can be defined through earth history using Eq. II.6. The two Sr species, Sr and ^{87}Sr , can react and are transported in the sediment column. At the end of the simulation values of ^{87}Sr and Sr are used to calculate $^{87}\text{Sr}/^{86}\text{Sr}$ as model output.

II.3.3 Boundary conditions and initial conditions

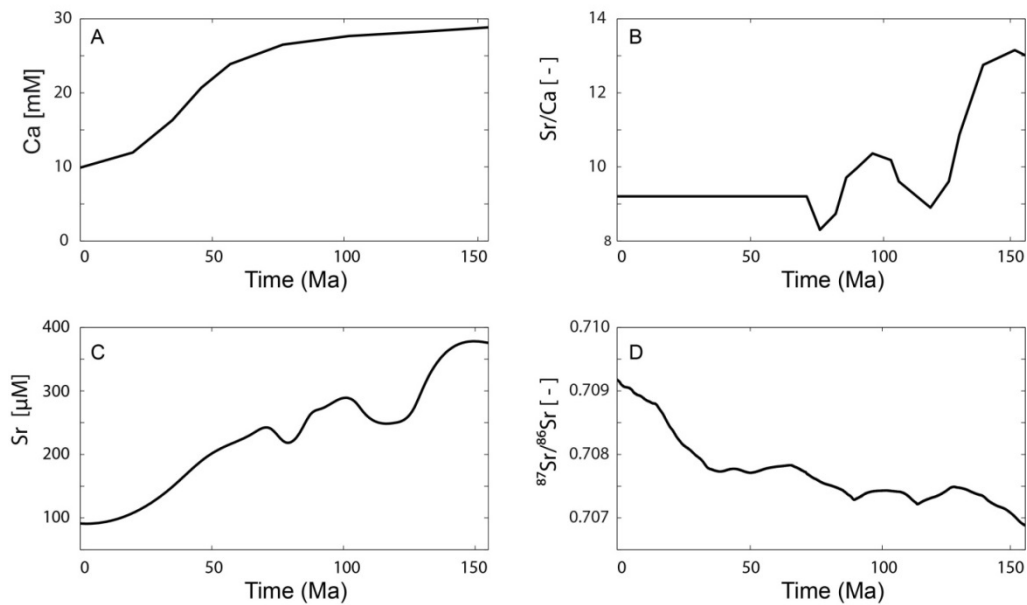
II.3.3.1 Dissolved species

Several upper and lower boundary conditions were applied in the case studies; Table II.1 shows a compilation of all boundary conditions. The upper boundary conditions (UBC) for the dissolved species Cl, Na and K are set to a constant modern seawater-like concentration (Cl = 557 mM; Na = 477 mM; Demicco et al., 2005) and concentration of 10 mM for K (Horita et al., 2002). For Ca, variations through Earth's history in seawater over the past are published by Horita et al. (2002). For Sr, the Sr/Ca ratio from Steuber and Veizer (2002) and the Ca concentration was taken to determine the Sr concentration in seawater over time. The $^{87}\text{Sr}/^{86}\text{Sr}$ ratio of seawater over time is available from McArthur et al. (2001) and has been used to determine the concentration of ^{87}Sr . The variations through time for Ca, Sr/Ca, Sr and $^{87}\text{Sr}/^{86}\text{Sr}$ are shown in Fig. II.2. For all scenarios, the UBC is an open boundary.

Table II.1: Boundary Conditions of all case studies and modelled scenarios

	UBC	LBC	Diffusion LBC	Advection LBC
Case Study 1+2	open	closed	zero gradient diffusion	no flow
Case study 3 (scenario 1-3)	open	closed	zero gradient diffusion	no flow
Case Study 3 (Scenario 4)	open	open	concentration gradient	inflow

UBC: Upper boundary condition; LBC: Lower boundary condition

**Figure II.2: Upper boundary conditions for the last 155 Ma; A: Ca; B: Sr/Ca; C: Sr; D: $^{87}\text{Sr}/^{86}\text{Sr}$**

For the first two case studies and Porto MV case study scenario 1 to 3, closed boundary conditions are applied to the lower boundary, effectively resulting in a zero-gradient boundary condition for diffusive transport and in a no flow boundary condition for advection. In the fourth scenario of Porto MV case study, the lower boundary is treated as an open boundary for diffusion and for advection to allow for fluid inflow through the base of the sediment column. Here, fixed concentrations are applied to the injected fluids. In this scenario, we tested the potential effect of the injection of crustal derived fluids on the pore water composition, predominantly with respect to variations in Sr, $^{87}\text{Sr}/^{86}\text{Sr}$, and Cl. Fluids circulating in the oceanic crust (lower boundary) are difficult to constrain, essentially, because data from this or a similar, deeply buried site are generally unavailable. Useful constraints are only available from hydrothermal vents, ridge flank systems or old, less deeply buried crust sections. Hydrothermal vent solutions typically have $^{87}\text{Sr}/^{86}\text{Sr}$ values between 0.7030-0.7040, Sr concentrations close to or slightly enriched with respect to normal seawater and variable Cl concentrations depending on the occurrence of subsurface phase separation (e.g. Douville et

al., 2002). Known ranges of values from ridge-flank systems (up to $\sim 60^\circ$ C) are between 0.70715-0.70745 for $^{87}\text{Sr}/^{86}\text{Sr}$, Sr concentrations up to 130 μM and normal chlorinity (e.g. Wheat et al., 2000). On the basis of the available measurements and that fact the crustal temperatures are $\sim 150^\circ\text{C}$ below Porto MV, we use a hypothetical fluid composition with $^{87}\text{Sr}/^{86}\text{Sr}$ of 0.706, Sr concentrations of 130 μM and normal seawater chlorinity. In addition to that, several test runs have shown that the impact of a change of $\pm 25 \mu\text{M}$ in Sr and ± 0.002 in the isotope ratio has just a small impact in the overall result.

II.3.3.2 Solid species

The sediment input over the whole model period of ~ 155 Ma was generally characterized by the deposition of smectite, illite, and calcium carbonate. The aim was not to build a detailed reconstruction of the sedimentary history, but rather to analyse the geochemical impact caused by the change from carbonate-dominated sedimentation to terrigenous sedimentation in the early Cretaceous.

Initial conditions for the solid phase were set for smectite to 70 wt% and illite 15 wt%. Since no information on the clay mineral composition at DSDP Site 135 was available, we used data from the DSDP Site 398 at the Vigo Seamount off Northwest Iberia with similar sedimentary units compared to DSDP Site 135 in order to constrain our assumptions. At DSDP Site 398, smectite contents average between 40 and 60 % (Chamley et al., 1979). Further evidence for the deposition of smectite-rich sediments comes from DSDP Site 547 on the Morocco continental margin, where clay mineral content is up to 90 % with a smectite fraction of more than 70 wt% (Chamley and Debrabant, 1984). However, measured smectite contents represent values mostly after smectite to illite transformation occurred so that a higher input (above measured average concentrations) seems to be a reasonable assumption. Sr isotope ratios for clay minerals were defined using the values measured in mud clasts, sampled from the MVs, varying between 0.7095 and 0.7120 (Hensen et al., 2015). Therefore, we used an average isotope ratio of 0.710 in the model.

As for the clay mineral composition, also no bulk data for Jurassic carbonate deposits are available for the Gulf of Cadiz. DSDP Site 135 did not reach the depth of Jurassic deposits. However, the Western Atlantic counterpart to DSDP Site 135, DSDP Site 105 reached Upper Jurassic layers described as clayey limestones (Hollister et al., 1972), suggesting a carbonate content of about 70 wt% . If Upper Jurassic carbonates are present in the sediment column of the model, we assume 70 wt% of calcium carbonate. Carbonate deposits contain isotopic ratio of the time of their deposition. For Upper Jurassic Carbonates a

isotopic ratio of 0.7068 corresponds to the seawater ratio at 155 Ma (Fig. II.2D; McArthur et al., 2001).

Equation II.4 requires the Sr concentration of carbonates. To solve this numerically stable a fourth solid species was introduced. To determine the initial condition, we used the following equation to approximate the Sr concentration of carbonates:

$$C_s = \frac{C_{Carbonate}}{100} * \rho_s * \frac{0.4}{M_{Ca}} * D_{Sr} * \frac{Sr^{2+}}{Ca^{2+}} \quad (II.7)$$

Where C_s is the concentration of Sr in carbonate (in μM), $C_{carbonate}$ is the carbonate concentration (in wt-%), the factor of 0.4 is introduced since only 40 wt-% of CaCO_3 is Ca, M_{Ca} is the molar weight of Calcium, D_{Sr} is the Sr distribution coefficient between seawater and carbonate, Sr^{2+}/Ca^{2+} is the seawater ratio of Sr and Ca. The distribution coefficient for deep sea carbonates after Stoll et al. (1999) is $D_{Sr} = 0.176$.

II.3.4 Solution algorithm

At the beginning of each model run, initial states of lithostatic pressure, pore fluid pressure, effective stress, porosity and temperature are initialized. The two first grid nodes with a cell size of 5 meter are predetermined. Each time step starts with the deposition of a new sediment layer. Therefore, the lithostatic pressure and the pore pressure solutions are updated by using the Finite Element (FE) scheme. Based on the new lithostatic and pore pressure calculations, a new effective stress is obtained for each of the grid nodes. The change in the effective stress field determines the degree of porosity reduction (i.e. compaction), which is performed on every mesh node.

Finally, the reference frame adjustment takes place and results in the growing of the sediment column and the new top node marking the seafloor. Based on the new pressure, the density of fluids, permeability, and the Darcy velocity for the fluid is recalculated. Darcy velocity is used to determine the state of the boundary condition at every time step. Upper boundary conditions adapt automatically according to the presence of the potential venting induced by the additional pore fluids entering the system (i.e. pore fluid re-freshening due to the smectite-illite transition). The temperature equation is solved for diffusion (FE) and advection (Finite Volume- FV) for the solid and fluid phase. The diffusion coefficients are determined using the new temperature profile. Advection and diffusion of each solute are solved separately using a FV and a FE scheme, respectively.

The last part of the solution algorithm contains the geochemical reactions. To maintain the numerical stability of the code, a sub-stepping method is applied to the geochemical reaction solver. This method adjusts the main model time-step to the rates of kinetically-resolved chemical reactions, which are commonly much faster than the transport steps. The sub-steps are solved within the main model loop. First, the smectite-illite transformation with the release of freshwater and Sr is accomplished, followed by the recrystallization of carbonates, and the release of Sr into the ambient pore waters. At the end of each time step, the isotope ratio for Sr is computed.

II.4 Model case studies

The numerical model approach is tested in three case studies, which show a characteristic fluid composition for their location within the GoC. In a first case study based on CAMV, we tested the ability of the model to simulate clay dehydration, which apart from evaporite dissolution (not considered in this study), is the dominant fluid forming process on the upper continental slope. The ATI MVs were used as a case study to test the interplay of carbonate recrystallization and clay dehydration as source for the mud volcano fluids. For Porto MV, we tested the combination of both mineral reaction and the advective inflow of fluids through altered oceanic crust. Parameters used for different model scenarios of the reaction package can be found in the appendix A.

II.4.1 Case study I: Captain Arutyunov MV

CAMV is located on the upper continental margin at 850 m water depth. Using Cl concentrations corrected for evaporite dissolution after Hensen et al. (2007), this MV shows very low Cl concentrations of ≈ 160 mM. At the same time, Sr concentrations are well above 790 μM with a pronounced radiogenic isotopic ratio of 0.7099 on average. The underlying sediments of the MV are of terrigenous origin within the accretionary wedge. The sediment column has a thickness of up to 9 km (Gutscher et al., 2009), and the oldest sediments above the crust are presumably of Late Cretaceous age (Hensen et al., 2015). Based on the age of the sediments, the model run time is set to 135 Ma. The key reaction is clay dehydration, where the activation energy and the frequency factor of the Arrhenius type reaction rate equation (Eq. II.2), as well as the temperature are the most crucial parameters. Values for the activation energy and the frequency factor, which can be found in the literature, are distributed over a broad range. After Cuadros and Linares (1996) the activation energy needed for the transformation of smectite to illite can be between 13,000 and 140,000 J mol^{-1} . The frequency

factor varies over several orders of magnitude (Huang et al., 1993; Pytte and Reynolds, 1989). Below, we show three model runs for CAMV to calibrate the reaction to the measured data. The three scenarios consider: (1) low activation energy combined with a low frequency factor, (2) high activation energy combined with a high frequency factor, and (3) medium activation energy combined with a low frequency factor.

In the first scenario, the transformation from smectite to illite starts almost on the seafloor, at a temperature of 4 °C (Fig. II.3). According to the present-day thermal limits of the reaction of 50 to 160 °C (shaded area in Fig. II.3), this scenario is unrealistic. With a high activation energy tested in the second scenario, we see the opposite effect on the reaction. The smectite to illite transformation starts at a temperature of more than 80°C. Medium activation energy like in scenario 3, results in a smectite to illite transformation which begins at about 50°C in 1.5 km sediment depth. The highest decrease of smectite and increase of illite can be observed between 4 and 6 km depth. Downwards, the reaction slows down again due to the smaller smectite amount in the sediment.

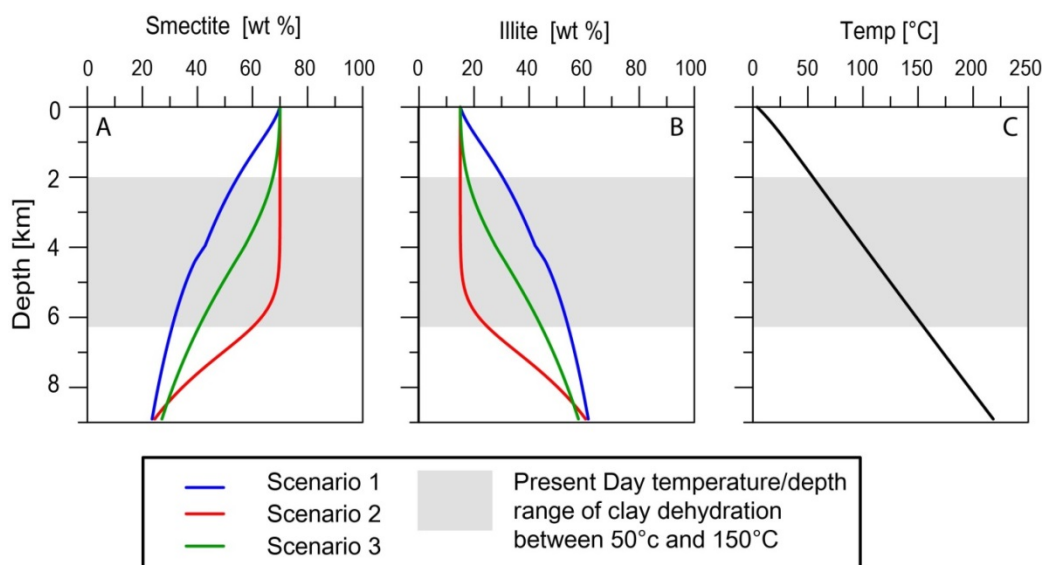


Figure II.3: Depth profile for solids of CAMV (A and B) and Temperature profile (C) for all three scenarios. Shaded area marks depth range for present-day smectite-illite transformation, below this area smectite-illite transformation is completed.

Nevertheless, all three scenarios result in low Cl concentrations with less than 200 mM (Fig. II.4A), but the profiles show a different behaviour for the various scenarios. The Sr concentration released by the reaction is controlled by the reaction rate (see Eq. II.3; Fig. II.4B). The isotopic ratio of $^{87}\text{Sr}/^{86}\text{Sr}$ released from clays is set to 0.7100 in all scenarios (according to data reported by Hensen et al., 2015). This value is reached from a depth of 4 km downwards (Fig. II.4 C). The profiles reveal considerable differences that are explained

by the differing onset of clay-mineral dehydration and diffusive exchange with seawater. Comparing the modelling results to measured concentrations of CAMV, it is clear that the model approach is able to reproduce the observed fluid signature for all three scenarios, in a sediment depth between 5.5 km and 7.5 km (Fig. II.4). In summary, the third scenario delivers the most satisfying results. In comparison to previous studies where this numerical model of clay dehydration has been applied (e.g. Cuadros, 2006), the observed decrease of smectite in this scenario is the most realistic one.

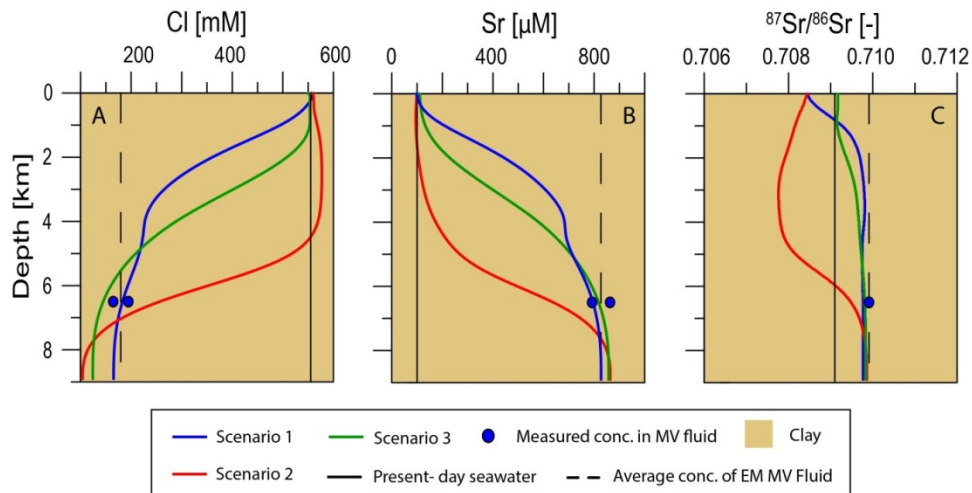


Figure II.4: Depth profiles of dissolved Cl (A), Sr (B) and $^{87}\text{Sr}/^{86}\text{Sr}$ (C) for CAMV. Measured concentrations are plotted in identified source depth. Black solid line is the average measured concentration of MV. Dashed line marks the modern seawater composition

The third critical parameter for clay dehydration is the temperature. The model considers convection and conduction of heat to determine the temperature distribution using a heat flow at the lower boundary of the model domain, and the constant T_0 value at the seafloor surface. Measurements of modern heat flow data by Grevemeyer et al. (2009) show a value of $\sim 45 \text{ mW m}^{-2}$ in the east and $\sim 60 \text{ mW m}^{-2}$ in the west for the GoC. However, applying only modern values to the time span of plate forming, this may cause an underestimation of the thermal state of the sediments, as at young crustal ages, the heat flow values may reach up to 300 mW m^{-2} (e.g. Stein and Stein, 1993). According to plate cooling models (e.g. Hasterok, 2013), the heat flow decreases fast at the beginning and reaches levels similar to modern heat flow values 50 to 60 Ma after plate formation. In the following, we test two variations for CAMV with (1) high heat flux of 300 mW m^{-2} in the beginning decreasing with time to present day heat flux, and (2) a constant heat flux 45 mW m^{-2} over time (Fig. II.5) to see the impact of a high heat flow at the beginning of the model run time.

The fast decrease of heat flux from plate cooling models to a 135 Ma oceanic plate can be observed in Fig. II.5, where the heat flow drops to a level of 45 mW m⁻² after 55 Ma. Therefore, both tested scenarios have for at least the last 80 Ma of model run time a heat flow equivalent to the present one.

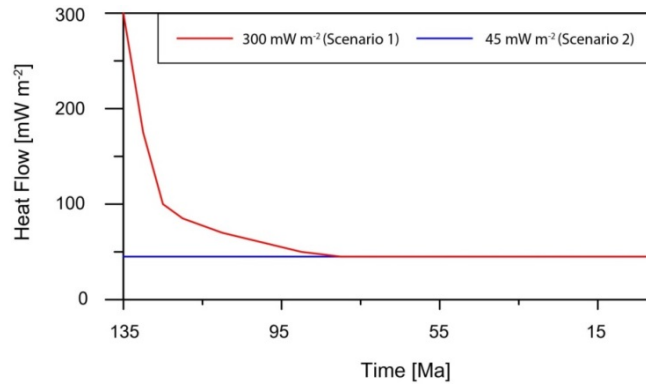


Figure II.5: Heat flow variations vs. time (Ma) for CAMV

The temperature profile for the scenario with the elevated heat flow shows a positive temperature offset of up to 30 °C for the first 35 Ma compared to the low, constant heat flow scenario (Fig. II.6). After 50 to 60 Ma, the difference between both scenarios is negligible. The higher temperature at the beginning results in an earlier dehydration of smectite. This causes a stronger decrease of Cl by up to 40 mM in the first 35 Ma of model run time (Fig. II.6). However, with a decreasing smectite content also the rate of dehydration drops. Therefore, with the same amount of smectite transformed into illite at the end of the model run time, the effect of lower Cl values also disappears after ≈65 Ma. At this stage, the plate cooled down to its present-day heat flux. Hence, most of the sediments have likely not experienced a higher heat flow than 45 – 65 mW m⁻². As a consequence, and for simplicity, a constant heat flow over time has been chosen for all subsequent scenarios.

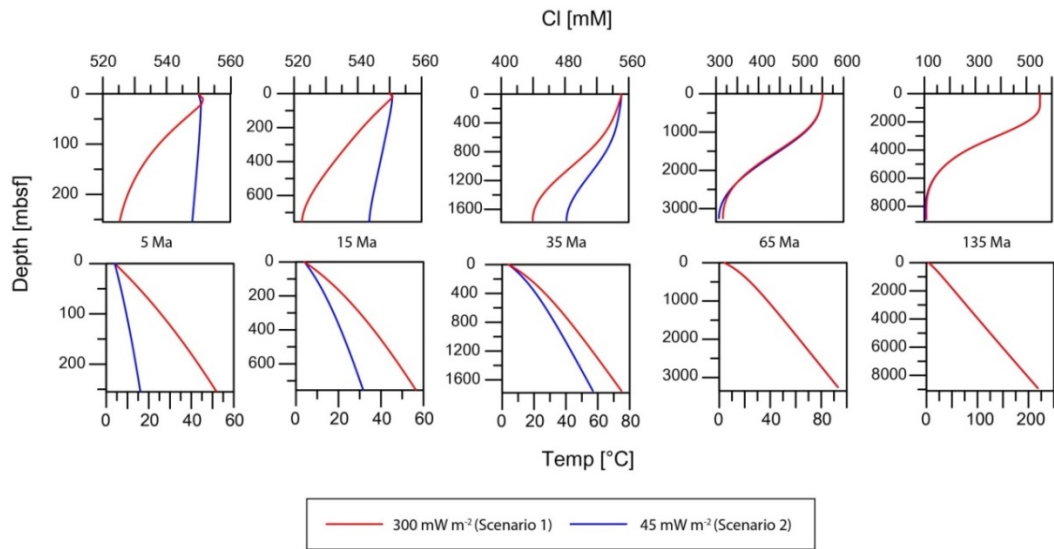


Figure II. 6: Cl vs. depth and temperature vs. depth profiles for model runtime after 5 Ma, 15 Ma, 35 Ma, 65 Ma and 135 Ma for high heat flow (300 mW m⁻², Scenario 1) and constant heat flow (45 mW m⁻², Scenario 2) of CAMV.

Overall, the implemented reaction transport module is able to simulate a fluid composition within the sedimentary units that is similar to the one at CAMV and other MVs on the accretionary wedge, reported by Hensen et al. (2015) and Scholz et al. (2009). The rate of clay-mineral dehydration could be constrained by the temperature distribution and key control factors from previous studies, resulting in a main reaction window between 50 to 150 °C as suggested by Cuadros and Linares (1996).

II.4.2 Case study 2: ATI MVs

The three ATI MVs are located in the south-eastern part of the Horseshoe Valley at a water depth of ~4500 m (Fig. II.1). Emanating fluids of the MVs show a decrease of about 50 mM in Cl compared to modern seawater. Sr concentrations vary between 500 μM and 1000 μM, whereas the ⁸⁷Sr/⁸⁶Sr ratios are close to 0.7075 for all three MVs. According to Hensen et al. (2015), the two main processes affecting the fluid genesis are clay mineral dehydration and recrystallization of Upper Jurassic carbonates.

The sedimentary structure for the basin model of the ATI MVs is derived from multichannel seismic profile SW07 from the ESF funded SWIM cruise 2006 (Hensen et al., 2015; Martínez-Lorient et al., 2013). It consists of about ~1.3 km of Upper Jurassic carbonates followed by ~3.7 km of terrigenous sediments. The carbonates are underlain by oceanic crust, which has been formed during the Jurassic (Martínez-Lorient et al., 2014) and

are characterized by the low Sr isotope ratio reported for the Upper Jurassic. The overall run time for the model is set to 155 Ma, while during the first 30 Ma mainly carbonate with a small amount of clay (7.5 wt% smectite and 2.5 wt% illite) is deposited, the last 125 to 0 Ma are followed by a sequence of predominantly terrigenous clay sedimentation.

The numerical model approach of Richter and DePaolo (1987) for the recrystallization of carbonates has been used by other authors e.g. Fantle et al. (2010; 2015); Fantle and DePaolo (2006); and Richter and Liang (1993). The effective distribution coefficient K in Eq. II.4, defined as the ratio of the Sr concentration in the carbonate, to the Sr concentration in fluid, is the most crucial parameter to control the reaction. Aforementioned authors typically used values between 12 and 20 for this parameter, derived from existing Sr^{2+} data of pore fluids and Sr concentrations of carbonates of ODP/IODP drill cores, while reported values for an effective distribution coefficient from experimental data range between <15 to >50 (Katz et al., 1972; Lorens, 1981). Since DSDP Site 135 did not reach the carbonate deposits there is no data set for the Sr content of carbonates in the working area. As a consequence, two values for K have been tested for the ATI MVs (Fig. II.7).

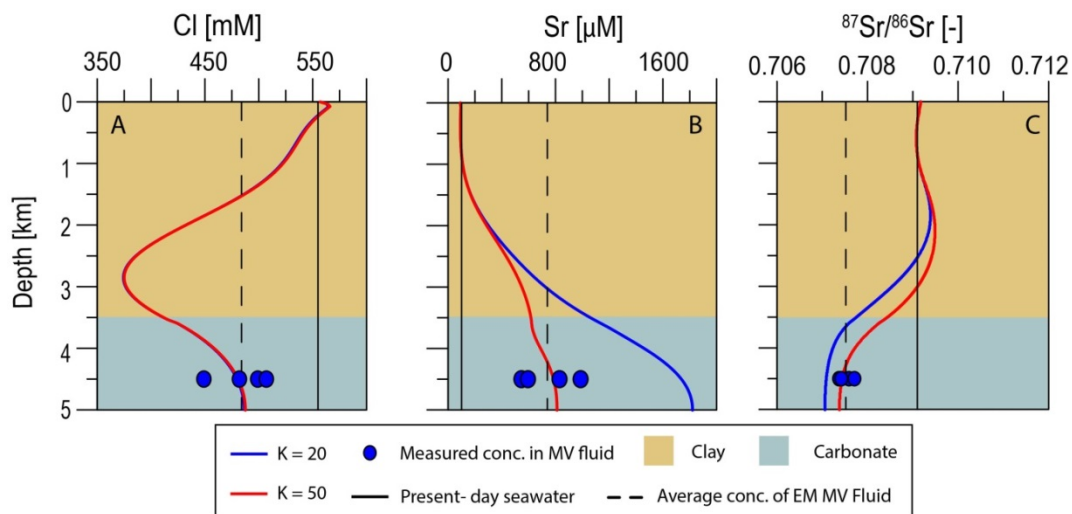


Figure II.7: Depth profiles of dissolved Cl (A), Sr (B) and $^{87}\text{Sr}/^{86}\text{Sr}$ (C) for ATI MVs with varying K values. Measured concentrations are plotted at the estimated source depth. Dashed line marks the modern seawater composition.

During the recrystallization of carbonates no fresh water is released and hence, there is no effect on conservative elements by dilution. This explains why Cl concentration depth profiles for both scenarios are identical (Fig. II.7A). The lower Cl concentration of about 495 mM at maximum depth compared to seawater (550 mM), results from a diffusive equilibration from the part of the model column where clay minerals are present. In this model section Cl shows a minimum of ~ 400 mM. The Cl values present in the part of

carbonate sediments, are in the range of the observed emanating fluid composition of the MVs. Applying effective distribution coefficients of $K = 20$, results in Sr concentrations within the fluid of $\sim 1850 \mu\text{M}$ (Fig. II.7B). Concentrations above $1000 \mu\text{M}$ have not been observed, but the highest concentration measured is $978 \mu\text{M}$ and the large scatter of data implies that also higher concentrations are not unlikely. An effective distribution coefficient of 50 leads to Sr concentrations representing the average observed concentrations of emanating fluids in a depth range from 3.0 to 5.0 km.

The combination of a high isotopic ratio from the clay dehydration and a medium isotope ratio from the carbonate recrystallization, should lead to a ratio lying between the two sources. Both tested model scenarios are able to reproduce the observed isotopic ratios, where $K = 20$ leads to the lowest ratio and $K = 50$ to the highest ratio. However, the variation between the scenarios is fairly small and the isotope ratio for all scenarios plots between 0.7070 and 0.7075 in the presumed source area (Fig. II.7C).

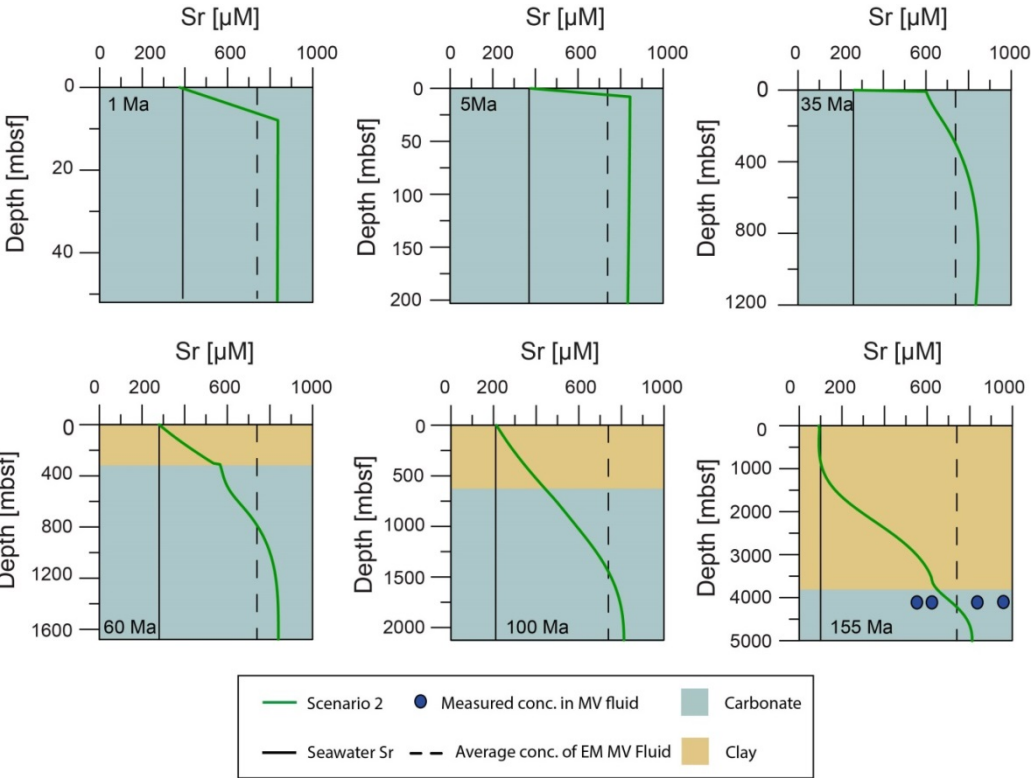


Figure II. 8: Sr concentrations depth profiles for 6 time steps at 1 Ma, 5 Ma, 35 Ma, 60 Ma, 100 Ma and 155 Ma model run time, for third scenario of ATI MV with an effective distribution coefficient of 50. Dashed line is indicating the seawater Sr concentration for the point in time (see Fig. II.2C). For the last time step the measured concentrations are plotted (blue points) at the estimated source depth.

Figure II.8 shows the Sr evolution over time for the second scenario of the ATI MVs. Reaction rates for recrystallization are highest right after deposition, the Sr concentration rises to about 850 μM in the lower part of the model domain within the first few million years. With ongoing sedimentation of terrigenous material, the Sr concentration decreases in the upper part of the modelling domain. Essentially, it becomes obvious that the major geochemical signal we see today in the emanating MV fluids has largely been formed shortly after the deposition of the carbonates.

II.4.3 Case study 3: Porto MV

Porto MV is located at the toe of the accretionary wedge at 3800 m water depth (Fig. II.1) and shows the most complex combination of geochemical tracers investigated in this study. Endmember MV fluids are characterized by low Cl concentrations of 350 mM, Sr concentrations of about 400 μM , and a $^{87}\text{Sr}/^{86}\text{Sr}$ ratio of 0.7078.

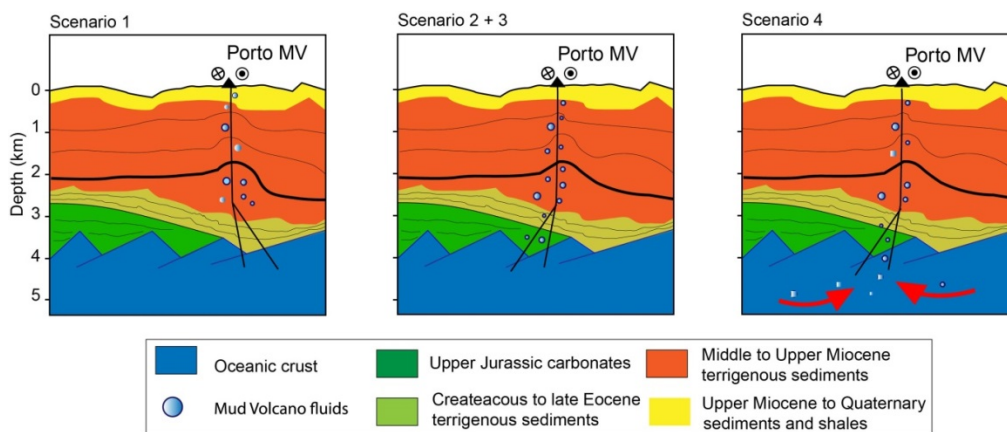


Figure II.9: Schematic sketches of the four scenarios tested for the Porto MV.

Results of the first scenario (Fig. II.9; sedimentation of terrigenous clay over 135 Ma forming a sedimentary column of ~ 3.8 km thickness) clearly indicate that the fluid composition, specifically the $^{87}\text{Sr}/^{86}\text{Sr}$ ratio (Fig. II.10C), cannot be explained by smectite to illite transformation only. An additional Sr source with a low to medium isotope ratio (e.g. from carbonate recrystallization as considered in case study 2) is required to obtain a better fit. Previously, Hensen et al. (2015) suggested that Upper Jurassic carbonates are absent in this area. However, Martínez-Loriente et al. (2018) showed that the area is marked by a number of horst and graben structures, which are illustrated by a depth-migrated seismic line crossing Porto MV (Fig. II.11). According to the stratigraphic interpretation, Upper Jurassic carbonates may be present to some extent in the graben structures northwest of Porto MV (kilometer 140 -160 in seismic profile SW02). Southeast of Porto there is no evidence for the

existence of Upper Jurassic carbonates; sediments there are generally of Mesozoic age and their composition cannot be clearly identified.

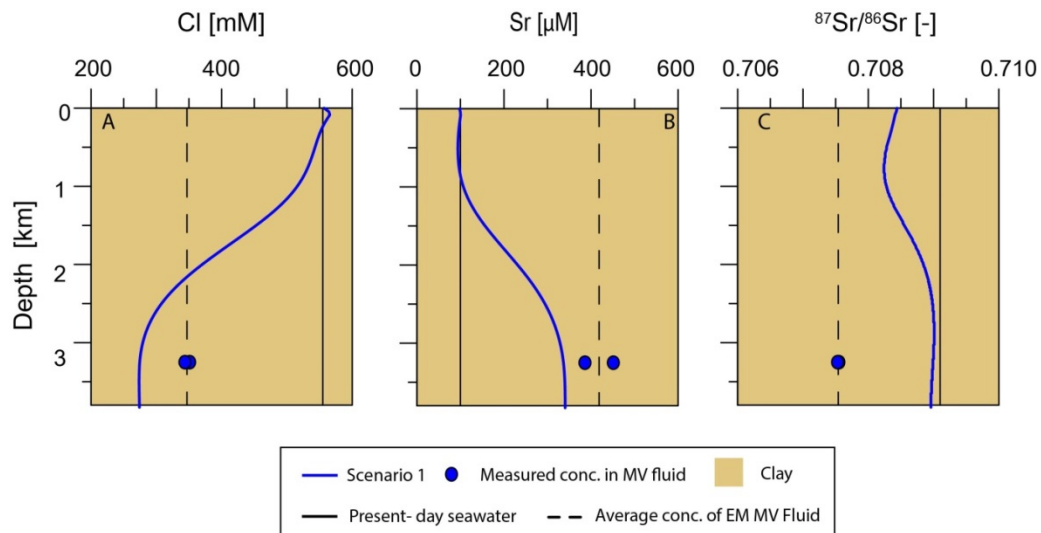


Figure II.10: Depth profiles of dissolved Cl (A), Sr (B) and $^{87}\text{Sr}/^{86}\text{Sr}$ (C) for the first scenario of Porto MV. Measured concentrations are plotted at the estimated source depth of MV fluids. Dashed line marks the modern seawater composition.

Based on this evidence, we tested two scenarios explicitly considering carbonate recrystallization occurring in carbonate layers of about 240 m (Fig. II.12 A-C) and 670m (Fig. II.12 D-F) thickness below the overlying ~ 3.6 km and 3,2 km of terrigenous sediments (Fig. II.9). The run time was set to 155 Ma considering the longer time of sediment deposition since the Upper Jurassic. The results show that a relatively thin layer of carbonate is not sufficient to obtain an acceptable fit to the data (Scenario 2). Recrystallization rates result in a good fit to the Sr concentrations (Fig II.12 B), although fail to obtain sufficiently low $^{87}\text{Sr}/^{86}\text{Sr}$ ratios (Fig. II.12 C). Vice versa, enhanced carbonate recrystallization due to a thick carbonate layer (Scenario 3) result in a good fit to the data with only slightly over-predicted Sr concentrations (Fig. II.12 E). However, the evidence for the existence of thick carbonate deposits at this location is weak. Generally, the alteration of mafic materials like volcanic ash is known to create low isotopic $^{87}\text{Sr}/^{86}\text{Sr}$ ratios in pore fluids. However, such deposits have not been reported for the GoC (Scholz et al., 2009). Alternatively, admixing of fluids from the underlying oceanic crust has been proposed (Hensen et al., 2015; Scholz et al., 2009). Although such a scenario remains speculative as the precise mechanism and the driving force for an upward advection are currently not known, we simulated such hypothetical injection into basal sediments (for about 30 Ma years) assuming concentrations and isotope values of crustal fluids as detailed in section II.3.3. In addition to the smectite to illite transformation in the terrigenous section, we combined carbonate recrystallization within a carbonate layer of

240 m thickness and the injection of fluids from the oceanic crust (Fig. II.9). With this combination of parameters, we also achieved a good approximation to the measured MV endmember data (Fig. 12 II.G – I), with a predicted source area of the MV fluids located above the carbonate sequence at roughly 3.25 km sediment depth. Assuming fluid advection through aged oceanic crust, major unknown parameters are the onset and the velocity of the flow. For our hypothetical scenario, we assume that it is related to the onset of subduction of the oceanic crust beneath the Gibraltar Arc, which started in the Tortonian (e.g. Duarte et al., 2013). Interestingly, mud volcanism in the GoC is reported to occur since the Mid-Tortonian (Toyos et al., 2016). The continuing convergence of the Eurasian and African plates could have provided the development of suitable conditions for focussed fluid advection, for example the opening of permeable fault systems. Analogously, the existence of MVs in front of the Barbados accretionary wedge has been ascribed to the reorganization of the fluid-flow regime in the igneous oceanic crust due to the change of tectonic stress along a fracture zone (see section II.4.4; Sumner and Westbrook, 2001).

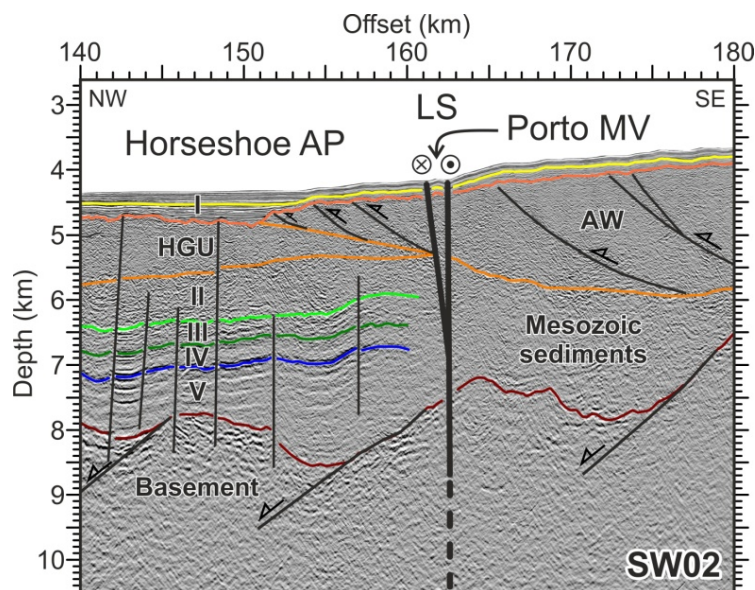


Figure II.11: Stratigraphic interpretation of pre-stack depth migrated multichannel seismic profile SW02 crossing Porto MV (modified from Martínez-Loriente et al., 2018). AW: Accretionary wedge, LS: Lineament South; HGU: Horseshoe gravitational unit; I: Upper Oligocene to Quaternary; II: Upper Cretaceous to Lower Eocene; III: Cretaceous; IV: Lower Cretaceous; V: Upper Jurassic. See Fig. II.1 for location.

It must be admitted at this stage that a sufficient pressure gradient leading to the upward advection of fluids from the oceanic crust can likely only be assumed along deep-reaching high permeability zones such as the LS fault (Figures II.1, II.11). However, a fully appropriate simulation of such a scenario would require at least a 2D model approach, which is beyond the scope of the present study. Nevertheless, the results of our simplified model

approach show that the injection of crustal-derived fluids offers a potential explanation for the observed fluid composition at Porto MV. In addition, the existence of such a transport pathway provides also a general mechanism to mobilize fluids from the oldest carbonate units deposited on top of the basement, since in situ fluid mobilization in such sediments is unlikely to occur.

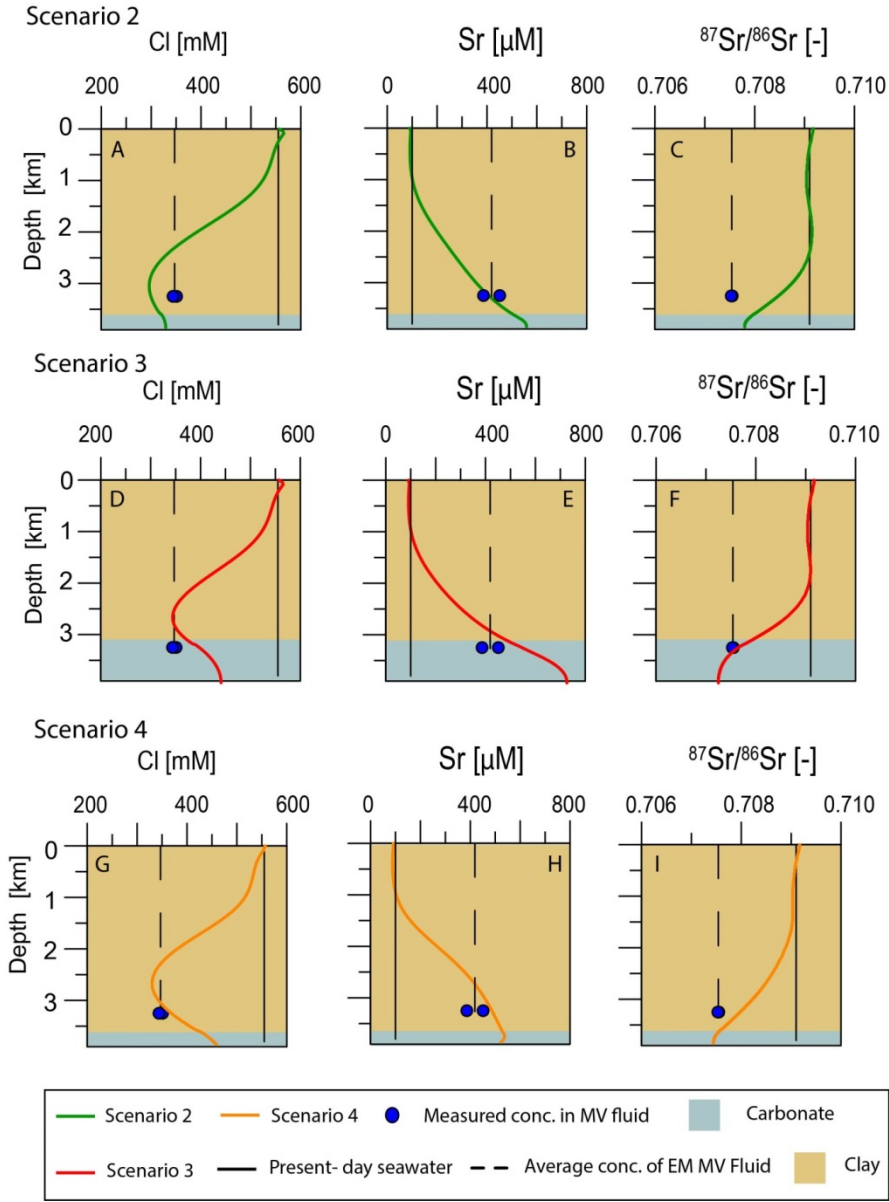


Figure II.12: Depth profiles for solutes Cl and Sr and isotope ratio of $^{87}\text{Sr}/^{86}\text{Sr}$, for second (A- C), third (D – F) and fourth (G- I) scenarios of Porto MV. Measured concentration is plotted in the estimated source depth. Dashed line marks the modern seawater composition.

II.4.4 Summary of case studies

Overall, all three case studies reveal that the numerical approach is appropriate to reproduce measured endmember concentrations of MV fluids at certain subsurface depth levels, indicating possible source regions of the fluids. The simulation results of all case

studies are summarized together with fluid endmember data from respective mud volcanoes in cross plots of Cl vs Sr and $^{87}\text{Sr}/^{86}\text{Sr}$ in Figure II.13, where the simulated data point always represents the concentration in the depth horizon with the closest match to the data. For the CAMV case study the best fit was obtained at 6.5 km (Fig. II.4), for ATI at 4.5 km (Fig. II.7), and for Porto at 3.25 km sediment depth (Fig. II.12). Generally, these results confirm previously made, but less constrained, estimates of the source depths of fluids or their approximate stratigraphic origin (e.g. Hensen et al., 2007; 2015; Pinheiro et al., 2005; Scholz et al., 2009).

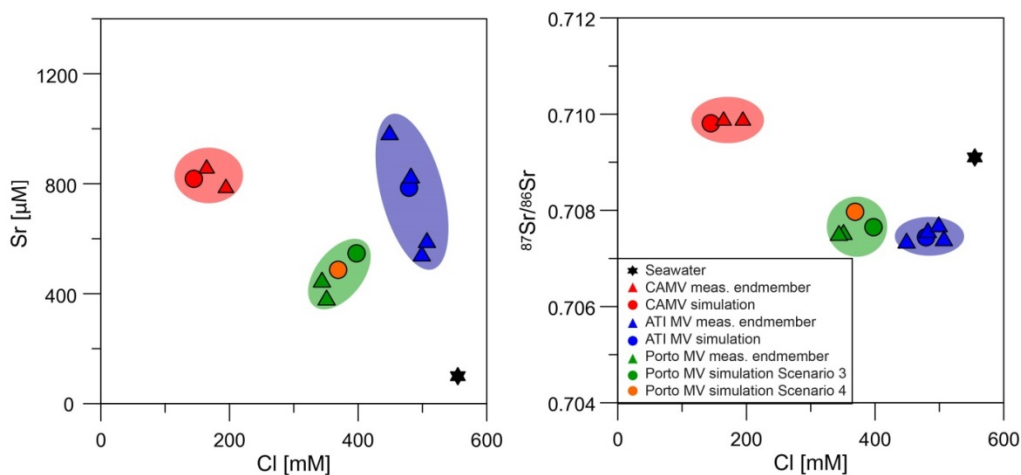


Figure II.13: Endmember plots of measured vs. modelled data; A: Cl vs Sr. B: Cl vs. $^{87}\text{Sr}/^{86}\text{Sr}$.

The source depth of fluids decreases to the west and seems to be correlated with the total sediment thickness (Gutscher et al., 2009), which is a rough indicator for the potential of producing low-salinity fluids by clay-mineral dehydration (Scholz et al., 2010b), being one of the major processes driving fluid advection and mud volcanism on the accretionary wedge. Analogously, this may imply that - due to the reduced potential of clay-mineral dehydration below the distal mud volcanoes - other process like fluid flow through the oceanic crust (as discussed for the Porto case study) might be necessary to initiate mud volcanism in this area. The predicted source depth in the ATI case study and Porto scenario 4 is located within the Upper Jurassic carbonates. As indicated above, carbonate recrystallization is a process affecting the fluid composition, but not generating fluids. Hence, also in the ATI area fluid injection from the oceanic basement might stimulate fluid flow and by this capturing chemical signals even from the oldest sedimentary strata above the basement (cf. Hensen et al., 2015).

Interestingly, the mechanisms described above do not seem to represent an isolated, special case only, but can be considered of being of broader significance. Deep-seated fluids expelled at MVs located offshore the deformation front of the Barbados Accretionary Prism

have been generally ascribed to be the result of dewatering processes occurring in the subducting slab sediments and migrating upward along major fault systems such as the décollement (e.g. Dia et al., 1995; Godon et al., 2004). However, a closer look at the geotectonic setting shows a close analogy to the situation observed in the Gulf of Cadiz. Similar to ATI MVs and Porto MV being aligned along the LS fault, Barbados MVs are aligned parallel to the Mercurus Fracture Zone in front of the accretionary prism. Sumner and Westbrook (2001) alternatively suggested that mud volcanism in this area was initiated by changes in plate motion along this fracture zone and driven by water released by the smectite to illite transformation affected by the circulation of fluids in the oceanic crust. Altogether, these observations call for a reassessment of previously made conclusions on fluid sources of the Barbados MVs and, in general, a closer investigation of the potential fluid flow in aged oceanic crust (>65 Ma). Numerical modelling as presented in this study may play a key role to identify and quantify major physical and geochemical processes involved.

II.5 Conclusions and implications

With our novel, fully-coupled, basin-scale model approach, we are able to simulate ubiquitous fluid forming processes, largely affecting the pore water geochemistry in deeply buried marine sedimentary environments. Using fluid data from MVs in the GoC we were able to constrain reaction rates and source depths of fluid generation. In summary, the most important aspects are:

- The numerical model approach is able to reproduce fluid signatures that have been observed in MV fluids on the upper continental slope and the deep sedimentary basin.
- Clay dehydration results in the dilution of conservative elements and the enrichment of fluid mobile Sr with radiogenic $^{87}\text{Sr}/^{86}\text{Sr}$ ratios. Carbonate recrystallization produces Sr enriched fluids with a distinct $^{87}\text{Sr}/^{86}\text{Sr}$ ratio shortly after the deposition of carbonates. With these reactions most of the fluid compositions measured at MVs within the GoC can be described satisfactorily and approximate source depths can be assigned.
- Fluid injection from the basement as suggested by Hensen et al. (2015) might play a role at the distant MVs in order to explain the geochemical signature at Porto MV and more generally, as a mechanism of mobilizing pore water from the oldest strata above the basement.

Overall, we were able to substantiate previously made conventional geochemical interpretations and the understanding of fluid genesis in the area. This novel model approach provides a powerful tool to analyse fluid generation and geochemical processes in sedimentary basins and is easily transferable to other regions and geochemical systems. Future models of this type will be expanded to 2D to enable adequate simulations of fluid generation and potential advection along low-permeability conduits. Finally, analogies to observations at the Barbados accretionary margin imply that fluid circulation in old oceanic crust – in combination with the occurrence of strike-slip fault systems and fracture zones -is a process with currently unknown importance to fluid dynamics and element cycling in sedimentary systems, which deserves systematic investigation in the future.

Acknowledgements

The manuscript benefited from additional support by the project FLOWS (EU-COST Action 1301). E.G. thanks financial support under project CTM2015-70155-R (INSIGHT). The manuscript benefited from constructive reviews of A. Mazzini, J. Ishibashi and an anonymous reviewer.

References

- Argus, D.F., Gordon, R.G., Demets, C. and Stein, S. (1989) Closure of the Africa-Eurasia-North America plate motion circuit and tectonics of the Gloria fault. *Journal of Geophysical Research* 94, 5585-5602.
- Baker, P.A., Gieskes, J.M. and Elderfield, H. (1982) Diagenesis of Carbonates in Deep-Sea Sediments--Evidence From SR/CA Ratios and Interstitial Dissolved SR²⁺ Data. *Journal of Sedimentary Research* 52.
- Baptista, M.A., Heitor, S., Miranda, J.M., Miranda, P. and Mendes Vitor, L. (1988) The 1755 Lisbon tsunami; evaluation of the tsunami parameters. *Journal of Geodynamics* 25, 143-157.
- Bartolome, R., Gràcia, E., Stich, D., Martínez-Loriente, S., Klaeschen, D., Mancilla, F., Lo Iacono, C., Dañobeitia, J.J. and Zitellini, N. (2012) Evidence for active strike-slip faulting along the Eurasia-Africa convergence zone: Implications for seismic hazard in the southwest Iberian margin. *Geology* 40, 495-498.
- Brown, K.M., Saffer, D.M. and Bekins, B.A. (2001) Smectite diagenesis, pore water freshening, and fluid flow at the toe of the Nankai wedge. *Earth Planet. Sci. Lett.* 194, 97-109.
- Calvert, A.J. and Potts, C.G. (1985) Seismic evidence for hydrothermally altered mantle beneath old crust in the Tydeman fracture zone. *Earth Planet. Sci. Lett.* 75, 439-449.
- Castellini, D.G., Dickens, G.R., Snyder, G.T. and Ruppel, C.D. (2006) Barium cycling in shallow sediment above active mud volcanoes in the Gulf of Mexico. *Chemical Geology* 226, 1-30.

Chamley, H. and Debrabant, P. (1984) Mineralogical and geochemical investigations of sediments on the Mazagan Plateau, Northwestern African Margin (Leg- 79, Deep- Sea Drilling Project) Initial Reports of the Deep Sea Drilling Project 79, 497-508.

Chamley, H., Debrabant, P., Foulon, J., d'Argoud, G.G., Latouche, C., Maillet, N., Maillot, H. and Sommer, F. (1979) Mineralogy and geochemistry of Cretaceous and Cenozoic Atlantic sediments off the Iberian peninsula (Site 398, DSDP Leg 47B). *Init. Repts. DSDP 47*, 429-449.

Chan, L.-H. and Kastner, M. (2000) Lithium isotopic compositions of pore fluids and sediments in the Costa Rica subduction zone: implications for fluid processes and sediment contribution to the arc volcanoes. *Earth Planet. Sci. Lett.* 183, 275-290.

Charlou, J.L., Donval, J.P., Zitter, T., Roy, N., Jean-Baptiste, P., Foucher, J.P. and Woodside, J. (2003) Evidence of methane venting and geochemistry of brines on mud volcanoes of the eastern Mediterranean Sea. *Deep Sea Research Part I.* 50, 941-958.

Cuadros, J. (2006) Modeling of smectite illitization in burial diagenesis environments. *Geochimica et Cosmochimica Acta* 70, 4181-4195.

Cuadros, J. and Linares, J. (1996) Experimental kinetic study of the smectite-to-illite transformation. *Geochimica et Cosmochimica Acta* 60, 439-453.

Demicco, R.V., Lowenstein, T.K., Hardie, L.A. and Spencer, R.J. (2005) Model of seawater composition for the Phanerozoic. *Geology* 33, 877-880.

Dia, A.N., Castrec, M., Boulègue, J. and Boudou, J.P. (1995) Major and trace element and Sr isotope constraints on fluid circulations in the Barbados accretionary complex. Part I: Fluid origin. *Earth Planet. Sci. Lett.* 134, 69-85.

Douville, E., Charlou, J., Oelkers, E., Bienvenu, P., Colon, C.J., Donval, J., Fouquet, Y., Prieur, D. and Appriou, P. (2002) The rainbow vent fluids (36°14' N, MAR): the influence of ultramafic rocks and phase separation on trace metal content in Mid-Atlantic Ridge hydrothermal fluids. *Chemical Geology* 184, 37-48.

Duarte, J.C., Rosas, F.M., Terrinha, P., Schellart, W.P., Boutelier, D., Gutscher, M.-A. and Ribeiro, A. (2013) Are subduction zones invading the Atlantic? Evidence from the southwest Iberia margin. *Geology* 41, 839-842.

Fantle, M., Maher, K. and DePaolo, D. (2010) Isotopic approaches for quantifying the rates of marine burial diagenesis. *Reviews of Geophysics* 48.

Fantle, M.S. (2015) Calcium isotopic evidence for rapid recrystallization of bulk marine carbonates and implications for geochemical proxies. *Geochimica et Cosmochimica Acta* 148, 378-401.

Fantle, M.S. and DePaolo, D.J. (2006) Sr isotopes and pore fluid chemistry in carbonate sediment of the Ontong Java Plateau: Calcite recrystallization rates and evidence for a rapid rise in seawater Mg over the last 10 million years. *Geochimica et Cosmochimica Acta* 70, 3883-3904.

Fehn, U., Moran, J.E., Snyder, G.T. and Muramatsu, Y. (2007) The initial $^{129}\text{I}/\text{I}$ ratio and the presence of "old" iodine in continental margins. *manuskript*.

Fisher, A.T. and Von Herzen, R.P. (2005) Models of hydrothermal circulation within 106 Ma seafloor: Constraints on the vigor of fluid circulation and crustal properties, below the Madeira Abyssal Plain. *Geochemistry, Geophysics, Geosystems* 6.

Fitts, T.G. and Brown, K.M. (1999) Stress-induced smectite dehydration: ramifications for patterns of freshening and fluid expulsion in the N. Barbados accretionary wedge. *Earth Planet. Sci. Lett.* 172, 179-197.

Fukao, Y. (1973) Thrust Faulting at a Lithospheric Plate Boundary Portugal Earthquake of 1969. *Earth Planet. Sci. Lett.* 18, 205-216.

Godon, A., Jendrzejewski, N., Castrec-Rouelle, M., Dia, A., Pineau, F., Boulegue, J. and Javoy, M. (2004) Origin and evolution of fluids from mud volcanoes in the Barbados accretionary complex. *Geochimica et Cosmochimica Acta* 68, 2153-2165.

Gràcia, E., Dañobeitia, J., Verges, J. and Bartolome, R. (2003a) Crustal architecture and tectonic evolution of the Gulf of Cadiz (SW Iberian margin) at the convergence of the Eurasian and African plates. *Tectonics* 22, doi:10.1029/2001TC901045.

Gràcia, E., Danobeitia, J., Verges, J. and PARCIFAL-TEAM (2003b) Mapping active faults offshore Portugal (36°N-38°N): implications for seismic hazard assessment along the southwest Iberian margin. *Geology* 31, 83-86.

Gràcia, E., Vizcaino, A., Escutia, C., Asioli, A., Rodes, A., Pallas, R., Garcia-Orellana, J., Lebreiro, S. and Goldfinger, C. (2010) Holocene earthquake record offshore Portugal (SW Iberia): testing turbidite paleoseismology in a slow-convergence margin. *Quaternary Science Reviews* 29, 1156-1172.

Grevemeyer, I., Kaul, N. and Kopf, A. (2009) Heat flow anomalies in the Gulf of Cadiz and off Cape San Vicente, Portugal. *Marine and Petroleum Geology* 26, 795-804.

Gutscher, M.-A., Dominguez, S., Westbrook, G.K., Le Roy, P., Rosas, F., Duarte, J., Terrinha, P., Miranda, J., Graindorge, D. and Gailler, A. (2012) The Gibraltar subduction: A decade of new geophysical data. *Tectonophysics* 574, 72-91.

Gutscher, M.-A., Dominguez, S., Westbrook, G.K. and Leroy, P. (2009) Deep structure, recent deformation and analog modeling of the Gulf of Cadiz accretionary wedge: Implications for the 1755 Lisbon earthquake. *Tectonophysics* 475, 85-97.

Haffert, L., Haeckel, M., Liebetrau, V., Berndt, C., Hensen, C., Nuzzo, M., Reitz, A., Scholz, F., Schönfeld, J., Perez-Garcia, C. and Weise, S.M. (2013) Fluid evolution and authigenic mineral paragenesis related to salt diapirism - The Mercator mud volcano in the Gulf of Cadiz. *Geochimica et Cosmochimica Acta* 106, 261-286.

Hasterok, D. (2013) A heat flow based cooling model for tectonic plates. *Earth Planet. Sci. Lett.* 361, 34-43.

Hayes, D.E., Pimm, A.C., Beckmann, J.P., Benson, W.E., Berger, W.H., Roth, P.H., Supko, P.R. and von Rad, U. (1972) Site 135, DSDP, Initial Reports U.S. Government Printing Office, Washington, D.C, pp. 15-48.

Hensen, C., Nuzzo, M., Hornibrook, E., Pinheiro, L.M., Bock, B., Magalhães, V.H. and Brückmann, W. (2007) Sources of mud volcano fluids in the Gulf of Cadiz - indications for hydrothermal imprint. *Geochimica et Cosmochimica Acta* 71, 1232-1248.

Hensen, C., Scholz, F., Nuzzo, M., Valadares, V., Gràcia, E., Terrinha, P., Liebetrau, V., Kaul, N., Silva, S., Martínez-Loriente, S., Bartolome, R., Piñero, E., Magalhães, V.H., Schmidt, M., Weise, S.M., Cunha, M., Hilario, A., Perea, H., Rovelli, L. and Lackschewitz, K. (2015) Strike-slip faults mediate the rise of crustal-derived fluids and mud volcanism in the deep sea. *Geology* 43, 339-342.

Hensen, C., Wallmann, K., Schmidt, M., Ranero, C.R. and Suess, E. (2004) Fluid expulsion related to mud extrusion off Costa Rica continental margin - a window to the subducting slab. *Geology* 32, 201-204.

Hoefs, J. (2004) *Stable Isotope Geochemistry*, 5 ed. Springer-Verlag Berlin Heidelberg.

Hollister, C.D., Ewing, J.I., Habib, D., Hathaway, J.C., Lancelot, Y., Luterbacher, H., Paulus, F.J., Poag, C.W., Wilcoxon, J.A. and Worstell, P. (1972) Site 105 - Lower continental rise hills, Deep Sea Drilling Program, Initial Reports Washington, D.C., pp. 219-312.

Horita, J., Zimmermann, H. and Holland, H.D. (2002) Chemical evolution of seawater during the Phanerozoic: Implications from the record of marine evaporites. *Geochimica et Cosmochimica Acta* 66, 3733-3756.

Huang, W.-L., Longo, J.M. and Pevear, D.R. (1993) An experimentally derived kinetic model for smectite-to-illite conversion and its use as a geothermometer. *Clays and Clay Minerals* 41, 162-177.

Kastner, M., Elderfield, H. and Martin, J.B. (1991) Fluids in convergent margins: what do we know about their composition, origin, and role in diagenesis and importance for oceanic chemical fluxes? *Phil. Trans. R. Soc. London, Ser. A* 335, 243-259.

Katz, A., Sass, E., Starinsky, A. and Holland, H. (1972) Strontium behavior in the aragonite-calcite transformation: An experimental study at 40–98 C. *Geochimica et Cosmochimica Acta* 36, 481-496.

Kopf, A. (2002) Significance of mud volcanism. *Reviews of Geophysics* 40, 1-52.

Kopf, A. (2003) Global methane emission through mud volcanoes and its past and present impact on the Earth's climate. *International Journal of Earth Sciences* 92, 806-816.

Loneragan, L. and White, N. (1997) Origin of the Betic-Rif mountain belt. *Tectonics*. *Tectonics* 16, 504-522.

Lorens, R.B. (1981) Sr, Cd, Mn and Co distribution coefficients in calcite as a function of calcite precipitation rate. *Geochimica et Cosmochimica Acta* 45, 553-561.

Luff, R. and Wallmann, K. (2003) Fluid flow, methane fluxes, carbonate precipitation and biogeochemical turnover in gas hydrate-bearing sediments at Hydrate Ridge, Cascadia Margin: Numerical modeling and mass balances. *Geochimica et Cosmochimica Acta* 67, 3403–3421.

Maldonado, A., Somoza, L. and Pallares, L. (1999) The Betic orogen and the Iberian-African boundary in the Gulf of Cadiz: geological evolution (central North Atlantic). *Marine Geology* 155, 9-43.

Martin, J.B., Gieskes, J.M., Torres, M. and Kastner, M. (1993) Bromine and iodine in Peru margin sediments and pore fluids: Implications for fluid origins. *Geochimica et Cosmochimica Acta* 57, 4377-4389.

- Martin, J.B., Kastner, M. and Elderfield, H. (1991) Lithium: sources in pore fluids of Peru slope sediments and implications for oceanic fluxes. *Marine Geology* 102, 281-292.
- Martin, J.B., Kastner, M., Henry, P., Le Pichon, X. and Lallement, S. (1996) Chemical and isotopic evidence for sources of fluids in a mud volcano field seaward of the Barbados accretionary wedge. *Journal of Geophysical Research* 101, 20325-20345.
- Martínez-Loriente, S., Gràcia, E., Bartolome, R., Sallarès, V., Connors, C., Perea, H., Lo Iacono, C., Klaeschen, D., Terrinha, P., Dañobeitia, J.J. and Zitellini, N. (2013) Active deformation in old oceanic lithosphere and significance for earthquake hazard: Seismic imaging of the Coral Patch Ridge area and neighboring abyssal plains (SW Iberian Margin). *Geochem. Geophys. Geosyst.* 14.
- Martínez-Loriente, S., Gràcia, E., Bartolome, R., Perea, H., Klaeschen, D., Dañobeitia, J.J., Zitellini, N., Wynn, R.B. and Masson, D.G. (2018) Morphostructure, tectono-sedimentary evolution and seismic potential of the Horseshoe Fault, SW Iberian Margin. *Basin Research* 30, 382-400.
- Martínez-Loriente, S., Sallarès, V., Gràcia, E., Bartolome, R., Dañobeitia, J.J. and Zitellini, N. (2014) Seismic and gravity constraints on the nature of the basement in the Africa-Eurasia plate boundary: New insights for the geodynamic evolution of the SW Iberian margin. *Journal of Geophysical Research: Solid Earth* 119, 127-149.
- Mazzini, A. and Etiope, G. (2017) Mud volcanism: An updated review. *Earth-Science Reviews* 168, 81-112.
- Mazzini, A., Scholz, F., Svensen, H., Hensen, C. and Hadi, S. (2017) The geochemistry and origin of the hydrothermal water erupted at Lusi, Indonesia. *Marine and Petroleum Geology*.
- McArthur, J.M., Howarth, R.J. and Bailey, T.R. (2001) Strontium Isotope Stratigraphy: LOWESS Version 3: Best Fit to the Marine Sr-Isotope Curve for 0–509 Ma and Accompanying Look-up Table for Deriving Numerical Age. *The Journal of Geology* 109, 155-170.
- Medialdea, T., Somoza, L., Pinheiro, L.M., Fernandez-Puga, M.C., Vazquez, J.T., Leon, R., Ivanov, M.K., Magalhaes, V., Diaz-del-Rio, V. and Vegas, R. (2009) Tectonics and mud volcano development in the Gulf of Cadiz. *Marine Geology* 261, 48-63.
- Milkov, A.V. (2000) Worldwide distribution of submarine mud volcanoes and associated gas hydrates. *Marine Geology* 167, 29-42.
- Milkov, A.V., Sassen, R., Apanasovich, T.V. and Dadashev, F.G. (2003) Global gas flux from mud volcanoes: a significant source of fossil methane in the atmosphere and the ocean. *Geophysical Research Letters* 30, 1037, doi:10.1029/2002GL016358.
- Morse, J.W. and Casey, W.H. (1988) Ostwald Processes and Mineral Paragenesis in Sediments. *American Journal of Science* 288, 537-560.
- Morse, J.W. and Mackenzie, F.T. (1990) *Geochemistry of Sedimentary Carbonates*. Elsevier.
- Nuzzo, M., Hornibrook, E.R.C., Gill, F., Hensen, C., Pancost, R.D., Haeckel, M., Reitz, A., Scholz, F., Magalhães, V.H., Brückmann, W. and Pinheiro, L.M. (2009) Origin of light volatile hydrocarbon gases in mud volcano fluids, Gulf of Cadiz — Evidence for multiple

sources and transport mechanisms in active sedimentary wedges. *Chemical Geology* 266, 359-372.

Paull, C.K., Dallimore, S.R., Caress, D.W., Gwiazda, R., Melling, H., Riedel, M., Jin, Y.K., Hong, J.K., Kim, Y.G., Graves, D., Sherman, A., Lundsten, E., Anderson, K., Lundsten, L., Villinger, H., Kopf, A., Johnson, S.B., Clarke, J.H., Blasco, S., Conway, K., Neelands, P., Thomas, H. and Cote, M. (2015) Active mud volcanoes on the continental slope of the Canadian Beaufort Sea. *Geochem. Geophys. Geosyst.* 16, 3160-3181.

Pinheiro, L.M., Ivanov, M., Kenyon, N., Magalhães, V.H., Somoza, L., Gardner, J.M., Kopf, A., Van Rensbergen, P., Monteiro, J.H. and Euromargins-MVSEIS-Team (2005) Structural control of mud volcanism and hydrocarbon-rich fluid seepage in the Gulf of Cadiz: results from the TTR-15 and other previous cruises, CIESM Workshop Monograph, pp. 53-58.

Pinheiro, L.M., Ivanov, M.K., Sautkin, A., Akhmanov, G., Magalhaes, V.H., Volkonskaya, A., Monteiro, J.H., Somoza, L., Gardner, J.V., Hamouni, N. and Cunha, M.R. (2003) Mud volcanism in the Gulf of Cadiz: results from the TTR-10 cruise. *Marine Geology* 195, 131-151.

Pytte, A.M. and Reynolds, R.C. (1989) The thermal transformation of smectite to illite, in: Naeser, N.D., McCulloh, T.H. (Eds.), *Thermal history of sedimentary basins*. Springer, New York, pp. 133-140.

Reitz, A., Haeckel, M., Wallmann, K., Hensen, C. and Heeschen, K. (2007) Origin of salt-enriched pore fluids in the northern Gulf of Mexico. *Earth Planet. Sci. Lett.* 259, 266-282.

Richter, F.M. and DePaolo, D.J. (1987) Numerical models for diagenesis and the Neogene Sr isotopic evolution of seawater from DSDP Site 590B. *Earth Planet. Sci. Lett.* 83, 27-38.

Richter, F.M. and Liang, Y. (1993) The rate and consequences of Sr diagenesis in deep-sea carbonates. *Earth Planet. Sci. Lett.* 117, 553-565.

Rovere, M., Ranero, C., Sartori, R., Torelli, L. and Zitellini, N. (2004) Seismic images and magnetic signature of the Late Jurassic to Early Cretaceous Africa-Eurasia plate boundary off SW Iberia. *Geophysical Journal International* 158, 554-568.

Schettino, A. and Turco, E. (2009) Breakup of Pangaea and plate kinematics of the central Atlantic and Atlas regions. *Geophysical Journal International* 178, 1078-1097.

Scholz, F., Hensen, C., De Lange, G.J., Haeckel, M., Liebetrau, V., Meixner, A., Reitz, A. and Romer, R.L. (2010a) Lithium isotope geochemistry of marine pore waters - Insights from cold seep fluids. *Geochimica et Cosmochimica Acta* 74, 3459-3475.

Scholz, F., Hensen, C., Lu, Z. and Fehn, U. (2010b) Controls on the $^{129}\text{I}/\text{I}$ ratio of deep-seated marine interstitial fluids: 'Old' organic versus fissiogenic ^{129}I . *Earth Planet. Sci. Lett.* 294, 27-36.

Scholz, F., Hensen, C., Reitz, A., Romer, R.L., Liebetrau, V., Meixner, A., Weise, S.M. and Haeckel, M. (2009) Isotopic evidence ($^{87}\text{Sr}/^{86}\text{Sr}$, $\delta^7\text{Li}$) for alteration of the oceanic crust at deep-rooted mud volcanoes in the Gulf of Cadiz, NE Atlantic Ocean. *Geochimica et Cosmochimica Acta* 73, 5444-5459.

Somoza, L., Díaz-del-Río, V., León, R., Ivanov, M., Fernández-Puga, M.C., Gardner, J.M., Hernández-Molina, F.J., Pinheiro, L.M., Rodero, J., Lobato, A., Maestro, A., Vázquez, J.T.,

Medialdea, T. and Fernández-Salas, L.M. (2003) Seabed morphology and hydrocarbon seepage in the Gulf of Cadiz mud volcano area: Acoustic imagery, multibeam and ultra-high resolution seismic data. *Mar. Geol.* 195, 153-176.

Stein, C.A. and Stein, S. (1993) A model for the global variation in the oceanic depth and heat flow with lithospheric age. *Nature* 359.

Stein, C.A., Stein, S. and Pelayo, A. (1995) Heat flow and hydrothermal circulation, in: Humphris, S.E., Zierenberg, R.A., Mullineaux, L.S., Thomson, R.E. (Eds.), *Seafloor hydrothermal systems: Physical, chemical, biological, and geological interactions*. American Geophysical Union, Washington DC, pp. 425-445.

Steuber, T. and Veizer, A. (2002) Phanerozoic record of plate tectonic control of seawater chemistry and carbonate sedimentation. *Geology* 30, 1123-1126.

Stoll, H.M., Schrag, D.P. and Clemens, S.C. (1999) Are seawater Sr/Ca variations preserved in Quaternary foraminifera? *Geochimica et Cosmochimica Acta* 63, 3535-3547.

Sumner, R.H. and Westbrook, G.K. (2001) Mud diapirism in front of the Barbados accretionary wedge: the influence of fracture zones and North America - South America plate motions. *Marine and Petroleum Geology* 18, 591-613.

Terrinha, P., Matias, L., Vicente, J., Duarte, J., Luis, J., Pinheiro, L., Lourenco, N., Diez, S., Rosas, F., Magalhaes, V., Valadares, V., Zitellini, N., Roque, C. and Victor, L.M. (2009) Morphotectonics and strain partitioning at the Iberian-Africa plate boundary from multibeam and seismic reflection data. *Marine Geology* 267, 156-174.

Tomaru, H., Lu, Z., Snyder, G.T., Fehn, U., Hiruta, A. and Matsumoto, R. (2007) Origin and age of pore waters in an actively venting gas hydrate field near Sado Island, Japan Sea: Interpretation of halogen and ^{129}I distributions. *Chemical Geology* 236, 350-366.

Toyos, M.H., Medialdea, T., León, R., Somoza, L., González, F.J. and Meléndez, N. (2016) Evidence of episodic long-lived eruptions in the Yuma, Ginsburg, Jesús Baraza and Tasyo mud volcanoes, Gulf of Cádiz. *Geo-Marine Letters* 36, 197-214.

Von Herzen, R. (2004) Evidence for continuing hydrothermal circulation in old crust, in: Davis, E.E., Elderfield, H. (Eds.), *Hydrogeology of the oceanic lithosphere*. Cambridge University Press, Cambridge, pp. 414-447.

Wheat, C.G., Elderfield, H., Mottl, M.J. and Monnin, C. (2000) Chemical composition of basement fluids within an oceanic ridge flank: Implications for along-strike and across-strike hydrothermal circulation. *Journal of Geophysical Research: Solid Earth* 105, 13437-13447.

Wortel, M. and Spakman, W. (2000) Subduction and slab detachment in the Mediterranean-Carpathian region. *Science* 290, 1910-1917.

Zitellini, N., Gràcia, E., Matias, L., Terrinha, P., Abreu, M.A., DeAlteriis, G., Henriot, J.P., Dañobeitia, J.J., Masson, D.G., Mulder, T., Ramella, R., Somoza, L. and Diez, S. (2009) The quest for the Africa-Eurasia plate boundary west of the Strait of Gibraltar. *Earth Planet. Sci. Lett.* 280, 13-50.

Zitellini, N., Rovere, M., Terrinha, P., Chierici, F., Matis, L. and Team, a.B. (2004) Neogene through Quaternary tectonic reactivation of SW Iberian passive margin. *Pure and Applied Geophysics* 161, 565-587.

III Insights into pore fluid geochemistry of the Azores Plateau: From early diagenesis to hydrothermal vents

Christopher Schmidt¹, Christian Hensen¹, Christian Hübscher, Klaus Wallmann¹, Steffen Kutterolf¹,
Volker Liebetrau¹, Mark Schmidt¹, and Thor Hansteen¹

1 GEOMAR Helmholtz-Centre for Ocean Research Kiel, 24148 Kiel, Germany

2 Department of Geophysics, University of Hamburg, 20146 Hamburg, Germany

To be submitted to Marine Geology

Abstract

The Azores Plateau is an active magmatic region in the Central North Atlantic Ocean. To date, no pore waters have been sampled from deep-sea sediments in this area. In this study, we present a comprehensive data set of major element composition and $^{87}\text{Sr}/^{86}\text{Sr}$ of pore waters from 22 gravity cores (GCs). In addition to that we analyzed sediments for their mineral (XRD) and their major element composition. Based on distinct characteristics in their pore water geochemistry we can subdivide background GCs of the Azores Plateau into two major groups. Ash rich GCs do not show any variations to seawater values except of a minor increase in Sr. In contrast ash poor GCs generally show a decreasing trend in Ca with increasing depth, accompanied by a minor SO_4 decrease and a more pronounced Sr increase. Three GCs were taken in three basins of the Terceira Rift, a hyper slow spreading center marking the northern boundary of the Azores Plateau. Those GCs are marked by a high total alkalinity and a down-core decrease in Ca, SO_4 and Sr concentrations. At four sample locations we observed a decrease in Mg and SO_4 accompanied with a Ca increase in the pore waters, a pattern typical for hydrothermal fluids. Multi-channel seismic data suggest that sill intrusions are present in the subsurface close to the core locations. Our observations offer preliminary indications of the existence of submarine hydrothermal systems on the Azores Plateau remote to the Mid- Atlantic Ridge. Overall, our study presents indications for hydrothermal activity and provides an overview on early diagenetic processes (e.g. calcium carbonate recrystallization, ash weathering, organic matter degradation) that occur in deep-sea sediments deposited on the Azores Plateau.

III.1 Introduction

The geological evolution of the Azores Plateau, located in the Central North Atlantic Ocean (Fig. III.1) has recently received high attention in many geoscientific disciplines e.g. geophysics and petrology (e.g. Beier et al., 2019; Beier et al., 2008; Marques et al., 2012; Marques et al., 2018; Vogt and Jung, 2004; Weiß et al., 2015). The magmatic and seismic activity, the interaction of the Mid-Atlantic ridge and the thickened oceanic crust have been studied in detail while very little is known about the sedimentary history, pore water geochemistry and prevailing diagenetic processes due to the lack of sediment sampling campaigns on the Azores Plateau. For technical reasons sediment sampling by gravity coring is a challenging task here, as numerous eruptions of volcanos of the Azores Archipelago lead to an abundant occurrence of ash and tephra layers in the upper sediment column. So far, only data for one gravity core (GC) has been published for the Azores Plateau, focusing on the reconstruction of paleo-climatic conditions (Vlag et al., 2004).

The alteration of ashes may significantly affect the composition of ambient pore waters. The formation of Mg-smectites and zeolites typically causes depletions in Mg as well as changes in K, Ca and Na, respectively (Gieskes and Lawrence, 1981). These and other ash alteration processes have been studied in a number of regions including the Pacific margin of Central America and Chile (Schacht et al., 2008; Scholz et al., 2013), the Sea of Okhotsk (Wallmann et al., 2008) and the Canary Islands (De Ros et al., 1997).

Igneous bodies like sills, dikes and small intrusions and formation of related hydrothermal systems are also common phenomena in magmatically active regions like the Azores Plateau. Weiß et al. (2015) documented numerous sills and volcanic cones present in and on the seafloor around São Miguel and the eastern Terceira Rift, the northern boundary of the Azores Plateau. Even though intensive search for hydrothermal vents has been carried out, only one submarine vent has been described in the Terceira Rift (D. Joao de Castro Seamount, Cardigos et al., 2005). Indications for one additional deep submarine system, which seems to be in a waning state, were presented for the Terceira Rift (Schmidt et al., In rev.). In addition to that, various hydrothermal springs and intertidal systems were described for the Azores archipelago (Couto et al., 2015).

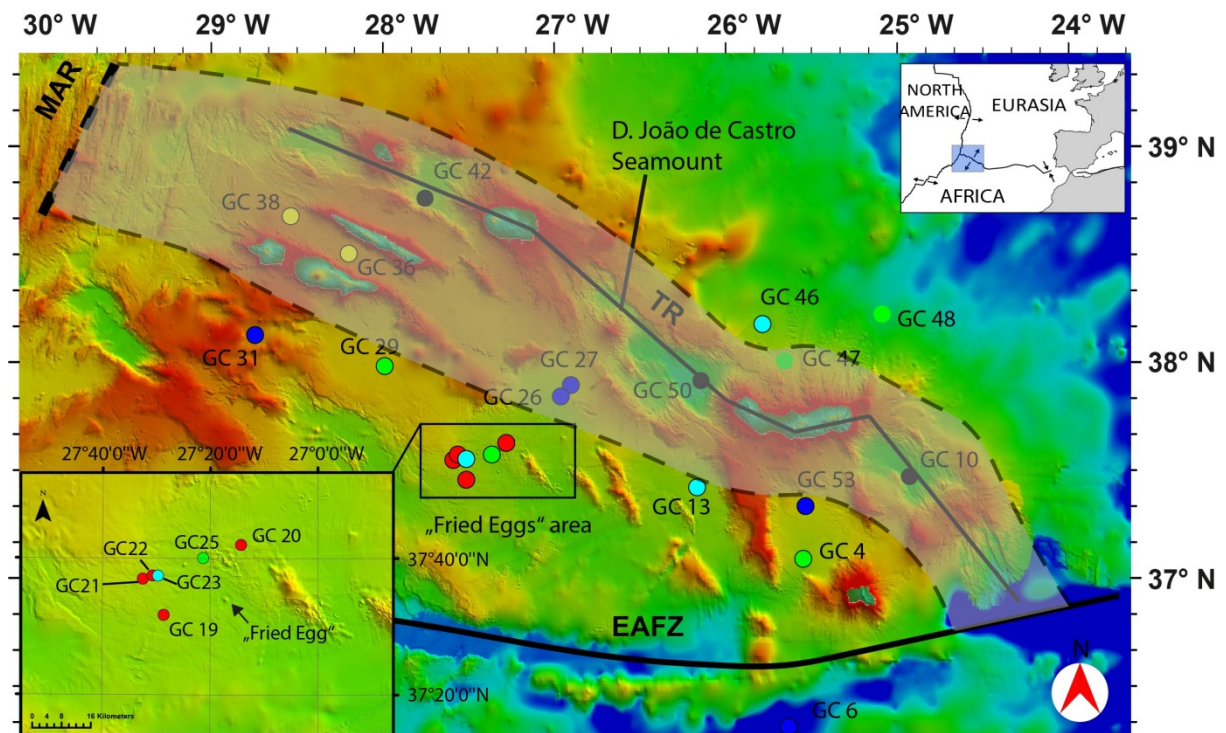


Figure III.1. Map of the Azores Plateau, grey area covers the diffuse plate boundary of the Terceira Rift; EAFZ: East Azores Fracture Zone; MAR: Mid-Atlantic Ridge, colors for sample locations indicate: green: ash rich; blue: ash poor; red: ash poor “Fried Eggs”; black: Terceira Rift and yellow: hydrothermal

During R/V Meteor cruise M141/1 “Azores Tephra”, we collected 22 GCs and analyzed them for their sediment and pore water geochemistry (Fig. III.1). Here, we present for the first time a comprehensive data set focusing on pore water geochemistry of the Azores Plateau. Our data suggest various processes in the sediment column including organic matter degradation, ash alteration and calcium carbonate recrystallization. In combination with multichannel-seismic data from two previous R/V Meteor cruises (M79/2 and M113/1, Hübscher, 2013; Hübscher et al., 2016) our geochemical data provide strong indications for four submarine hydrothermal systems on the Azores Plateau.

III.2 Regional Setting

The Azores Plateau, a topographic anomaly marked roughly by the 2000 m isobaths in the Central Atlantic Ocean, is located at the triple junction of the Eurasian, Nubian, and North American plates (Fig. III.1). The Mid-Atlantic Ridge crosses the plateau and divides it in a smaller western and larger eastern section. Our study region comprises the plateau to the east of the Mid-Atlantic Ridge. The Terceira Rift marks the northern boundary and the East Azores Fracture Zone (EAFZ) is the southern boundary of the plateau. The Terceira Rift and

EAFZ join east of São Miguel, which results in the triangular shape of the plateau, and continue to the east into the Gloria Fault.

The origin of the volcanism in the Azores area and thus the formation of the Azores Plateau has been explained either by a thermal plume from the deep mantle (Haase and Beier, 2003; Schilling, 1975; Widom and Shirey, 1996) or by excess melting of the mantle due to comparatively high volatile contents (a "wetspot"; Bonath, 1990). It appears likely that a combination of thermal and chemical heterogeneities favors partial melting, thus underlining the importance of enduring plume-ridge interactions (e.g. Métrich et al., 2014). Present volcanic activity is located within the Terceira Rift (Kueppers and Beier, 2018), and all the Azores islands except Santa Maria in the East are considered volcanically active. The geochemical compositions of the volcanics are diverse and range from basaltic and alkali basaltic to rhyolitic compositions (e.g. Beier et al., 2010; Haase and Beier, 2003; White et al., 1979).

III.3 Materials and Methods

III.3.1 Sediment and pore water sampling

For sediment sampling GCs of 5 to 18 m length were used equipped with a plastic liner. The sampling interval was chosen depending on the total recovery but normally did not exceed 20 cm. In the case that prominent ash layers were present in the core, Rhizones from Rhizosphere were used to sample the pore water. Sediment samples were not taken from the splitting surface and in contact with the liner to avoid contamination with seawater. Sediment samples were squeezed in the cold room using an argon gas squeezer operated at 5 to 7 bar. The pore water was filtered through 0.2µm cellulose Whatmann filters. A list of all cores with their locations and water depth is provided in Tab. III.1.

Table III.1 Geographical locations, water depth and recovery of GCs taken during M141/1

Station	Core	Latitude	Longitude	Water depth (m)	Recovery (cm)
Ash rich GCs					
1144-1	GC4	37°9.056'N	25°26.595'W	2300	445
1188-1	GC25	37°37.384'N	27°35.774'W	2800	548
1198-1	GC29	38°3.301'N	27°58.883'W	1820	380
1238-1	GC47	38°4.528'N	25°32.313'W	2000	420
1240-1	GC48	38°16.044'N	24°53.251'W	3400	365
Ash poor GCs					
1148-1	GC6	36°22.244'N	25°32.770'W	4000	666
1192-1	GC26	37°55.070'N	26°54.333'W	2240	905
1194-1	GC27	37°58.194'N	26°50.668'W	2100	887
1204-1	GC31	38°12.925'N	28°45.934'W	1200	900
1249-1	GC53	37°29.442'N	26°14.375'W	2374	1115
“Fried Eggs”					
1174-1	GC19	37°31.720'N	27°28.599'W	2200	1090
1176-1	GC20	37°41.981'N	27°14.273'W	2850	1175
1180-1	GC21	37°36.997'N	27°32.488'W	2850	545
1182-1	GC22	37°37.485'N	27°30.697'W	2940	605
Terceira Rift					
1156-1	GC10	37°31.421'N	24°47.553'W	2860	410
1226-1	GC42	38°57.393'N	27°39.491'W	2460	213
1244-1	GC50	37°58.345'N	26°05.046'W	2800	166
Hydrothermally influenced					
1162-3	GC13	37°29.608'N	26°04.801'W	2320	900
1184-1	GC23	37°37.456'N	27°29.684'W	2850	548
1215-3	GC36	38°34.678'N	28°12.548'W	1250	247
1219-2	GC38	38°44.810'N	28°34.236'W	1200	484
1236-1	GC46	38°14.851'N	25°40.205'W	2450	758

III.3.2 Pore water analyses

Total alkalinity (TA) and ammonium (NH_4) were analyzed on board. TA was determined by titration with 0.02 N HCL and a methyl red indicator using a METHONOM titration unit 876 Dosimat plus. The solution was bubbled with argon gas to remove CO_2 and H_2S . Analyses for pore water NH_4 were completed onboard using a Hitachi U2800A spectrophotometer. NH_4 was measured as indophenol blue, followed standard procedures (Grasshoff et al., 1999). The IAPSO seawater standard was used for calibration, applying a calibration curve with 8 standards covering the concentration range between 0 and 332.62 μM . 1 cm^3 of sample or standard was made up to 5 cm^3 with pure water and 0.2 cm^3 phenol solution. After 2 minutes 0.1 cm^3 citrate buffer and 0.2 cm^3 DTT reagent were added. After mixing, the samples were kept at 30-40°C for 1-2 hours before the absorbance is measured at 630 nm.

In shore-based laboratories at GEOMAR cation concentrations were determined in acidified subsamples using Inductively Coupled Plasma Optical Emission Spectrometry (ICP-OES)). Anion concentrations were analyzed using Ion Exchange Chromatography. A full description of the methods used is given at <https://www.geomar.de/en/research/fb2/fb2-mg/benthic-biogeochemistry/mg-analytik/>.

III.3.3 Isotope analyses

Sr isotope ratios ($^{87}\text{Sr}/^{86}\text{Sr}$) were measured by thermal ionization mass spectrometry (TIMS, TRITON, ThermoFisher Scientific) at GEOMAR on aliquots of the acidified ICP-OES pore water samples. According to the prior element concentration analyses (ICP-OES) individual sample amounts equivalent to approx. 1500 ng Sr (usually in the range of tens to hundreds of μl pore water) were dried down in 2 ml of a 1 plus 2 mixture of 30 % H_2O_2 (supra pure) and 8 N HNO_3 (double distilled from p.a. quality). The separation of Sr followed a highly selective one step ion exchange chromatography using SrSpec resin (Eichrom) at whole procedure blanks of max. 60 pg. Before loading 100 to 200 ng Sr mixed with TaCl5 activator on Re single filaments for TIMS measurements the Sr eluate was dried down in the $\text{H}_2\text{O}_2/\text{HNO}_3$ mixture as described above. Repeated analyses of the standard NIST SRM 987 were used for performance monitoring and normalization of the measured $^{87}\text{Sr}/^{86}\text{Sr}$ ratios applying a standard value of 0.710248 and reaching a reproducibility of ± 0.000010 (2SD, n=10) throughout the study.

III.3.4 Head space gas analyses

Headspace gas composition of 20 ml glass vials containing 3 cm³ of sampled sediment and additional 6 ml NaCl-solution were prepared according to Sommer et al. (2009). The vials were stored upside down at room temperature until measurement by using gas chromatography at GEOMAR. 100 µl of headspace gas was injected into a Shimadzu gas chromatograph (GC-2014), equipped with flame ionization detector and thermal conductivity detector (carrier gas: He 5.0; HayeSep™ Q 80/100 column, column length: 2 m; column diameter: 1/8"). The detection limit for CO₂ was 100 ppmV. Precision was about 4 % (2SD).

III.3.5 Solid phase

For the chemical bulk analyses, sediments were dried at 65°C for 24 hours and homogenized. 100 mg of each sample was filled into a Savillex vessel and treated with 2 cm³ HF, 2 cm³ HNO₃ and 3 cm³ HClO₄ at 185°C and another 1 cm³ of HNO₃ was added after 8 hours and evaporated to near dryness. Afterwards the sample was re-dissolved in 3 ml 5% HNO₃ and heated to 60 °C for 4 hours and transferred into acid-cleaned HDPE vials. Samples were measured at GEOMAR laboratories using ICP-OES. The full method description is available at: <https://www.geomar.de/en/research/fb2/fb2-mg/benthic-biogeochemistry/mg-analytik/acid-digestion/> and described in Scholz et al. (2016).

In addition, selected cores were analyzed with X-ray diffraction (XRD) at GEOMAR using the Philips Diffractometer Goniometer 4 with automatic divergent slot and monochromator. Mineral analyses were performed using the X PowderX software (Version 2017.01.xx) by J.D. Martin (Martín, 2004). XRD analyses for GC29 were made for the background sediments and not for the ash layers.

III.3.6 Seismic data

The reflection seismic data had been collected during RV Meteor expedition M79/2 (Hübscher, 2013) and M113/1 (Hübscher et al., 2016). Four GI-Guns created the seismic signal and a digital seismic cable of 600 m active length (144 channels) recorded the data. Processing included bandpass-filtering, energy balancing, nmo-correction, stacking, time-migration and fx-deconvolution. For an overview of the marine seismic method, see Hübscher and Gohl (2014).

III.3.7 Numerical reaction transport model

Two numerical reaction transport model approaches were performed using Mathematica 11.3 (Wolfram Research, 2018).

III.3.7.1 AOM Model

The model is capable to simulate organic matter breakdown, SO_4 reduction and methane turnover based on the numerical model described by Wallmann et al. (2006). The included solute species are Ca, TA, SO_4 , CH_4 . The model is run to steady state conditions and fixed boundary conditions are imposed at the upper boundary (0 cm), and lower boundary (max depth). Lower boundary concentrations and rates were adjusted to fit the model curve to measured data. A detailed list of all used parameters can be found in the Appendix B.

III.3.7.2 Carbonate recrystallization model

The second reaction transported model was used to simulate recrystallization of calcium carbonate and the release of Sr during this reaction. The model is a simplified version of the model described in Schmidt et al. (2018). The carbonate recrystallization is based on the model of Richter and DePaolo (1987), a detailed list with the applied parameters to the model can be found in the Appendix B.

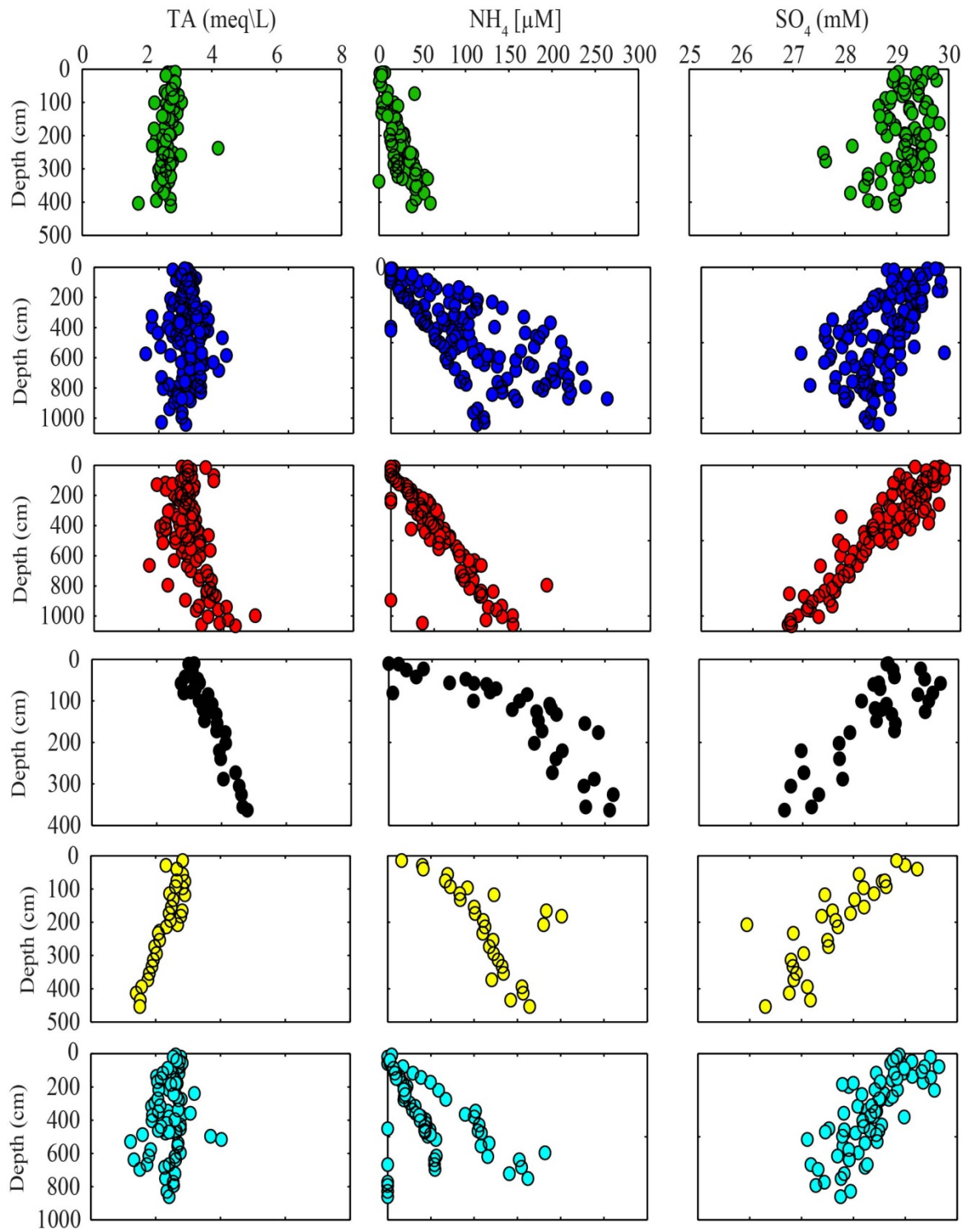
III.3.8 End member calculation

Pore water sampling by gravity coring results in a mixture of seawater and diagenetic pore waters or hydrothermal influenced fluids, coming from depth. To compare the sampled hydrothermally influenced fluids to other studies a theoretical fluid end member (EM) is calculated. The EM is calculated as binary mixing between seawater and the theoretical hydrothermal fluid composition. Mg is quantitatively removed from fluids during hydrothermal reactions hence Mg was set to 0 mM in the calculation for the EM. EM concentrations were then determined for SO_4 and Ca.

III.4 Results

III.4.1 Pore water chemistry

Based on pore water concentrations of TA, NH_4 , Ca, Mg SO_4 and Sr the 22 GCs were subdivided into 4 groups. Those groups are (i) ash rich GCs, (ii) ash poor GCs with a subgroup of GCs taken close to the “Fried Eggs” area and area with several Ma old volcanic cones, (iii) GCs taken in the Terceira Rift, and (iv) hydrothermally influenced GCs. In Fig. III.2 element depth profiles for TA, NH_4 , Mg, Ca SO_4 and Sr are shown. In the following we will describe the characteristic pore water patterns for each group.



● Ash rich GCs
 ● Ash Poor GCs
 ● Ash Poor GCs „Fried Eggs“
 ● Terceira Rift
● Hydrothermal (GC 36, GC 38)
 ● Hydrothermal (GC 13, GC 23, GC 46)

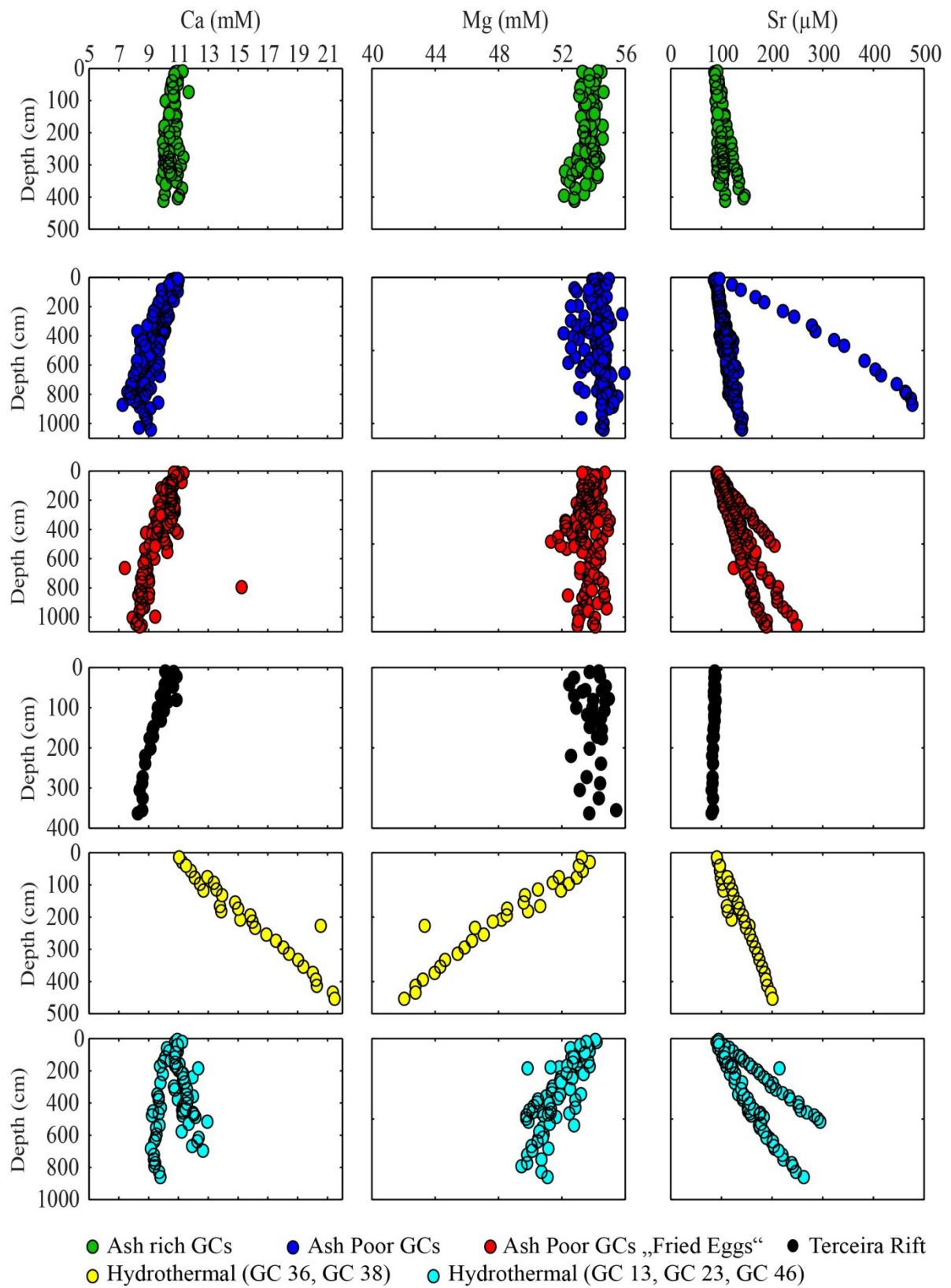


Figure III.2. Pore water depth profiles for TA, NH₄, Mg, Ca Sr and SO₄ for each group.

III.4.1.1 Background GCs Azores Plateau

III.4.1.1.1 Ash rich

Five GCs (GC4, GC25, GC29, GC47, and GC48) across the Azores Plateau show prominent volcanic ash and tephra layers. In general, these GCs are marked by no significant changes with depth in TA, Ca and Mg but a small increase in NH₄ to up to 100 μM. Only GC25 shows a small peak in Si in 100 cm below seafloor (bsf), whereas all other cores do not have such a peak. All cores show a Sr increase of about 10 μM from seawater. Only GC47 shows a stronger increase to 150 μM at 400 cm bsf (Fig. III.2).

III.4.1.1.2 Ash poor

Five of the GCs (GC6, GC26, GC27, GC31, and GC53) are characterized by the absence of prominent volcanic ash layers in the sediments. TA shows no deviation with depth, but NH₄ is higher with up to 200 μM. Ca concentrations decrease with depth by 2-3 mM with respect to seawater while Mg is constant and shows no deviations from seawater, whereas SO₄ is decreasing. Sr is increasing for all cores to concentrations of up to 150 μM. GC31 however, shows a strong increase to 477 μM.

III.4.1.1.3 Ash poor “Fried Eggs”

Overall six GCs were taken in the area named Fried Eggs on the Central Azores Plateau. Four of the GCs (GC19, GC20, GC21 and GC22) are characterized by the absence of prominent ash layers. In general, they are comparable to the other ash poor cores. However, a small increase in TA and clear decrease in SO₄ can be observed. There is an also a more pronounced increase in Sr over depth reaching concentrations of up to 250 μM.

III.4.1.2 Background GCs Terceira Rift

Three GCs (GC10, GC42 and GC50) were taken in three rift basins of the Terceira Rift. The recovery for all cores is small with less than 400 cm. TA is increasing in all cores up to 6 meq/L and NH₄ reaches up to 300 μM. Mg shows no deviation with depth, whereas Ca is decreasing from seawater values to about 8.3 mM. Sr concentrations are decreasing here from seawater values by 10 μM to about 80 μM. SO₄ shows a decrease of 1 mM with depth.

III.4.1.3 Hydrothermally influenced GCs

Five GCs (GC13, GC23, GC36, GC38 and GC46) from various locations across the Azores Plateau show trends in pore water geochemistry that differ from all other cores. In general, GC36 and GC38 show the strongest deviations for all elements (Fig III.2), GC23 and GC46 show the same, but less pronounced trends. All GCs show an increase in Ca, with the

strongest deviation from seawater of up to ~ 22 mM in GC38. In contrast, Mg and SO₄ decrease over depth in all GCs. For GC38, deviations from seawater are very pronounced (13 mM for Mg and 3 mM for SO₄). GC13 shows a slightly different trend for some elements.

III.4.2 Isotope data

Most of the cores also show no change for ⁸⁷Sr/⁸⁶Sr with depth and stay around modern seawater values of 0.709176 (Banner, 2004) or slightly below. However, GC36 and GC38 show a deviation to more non-radiogenic values with depth. The lowest measured ⁸⁷Sr/⁸⁶Sr is 0.708058 in GC38 (Fig. III.3).

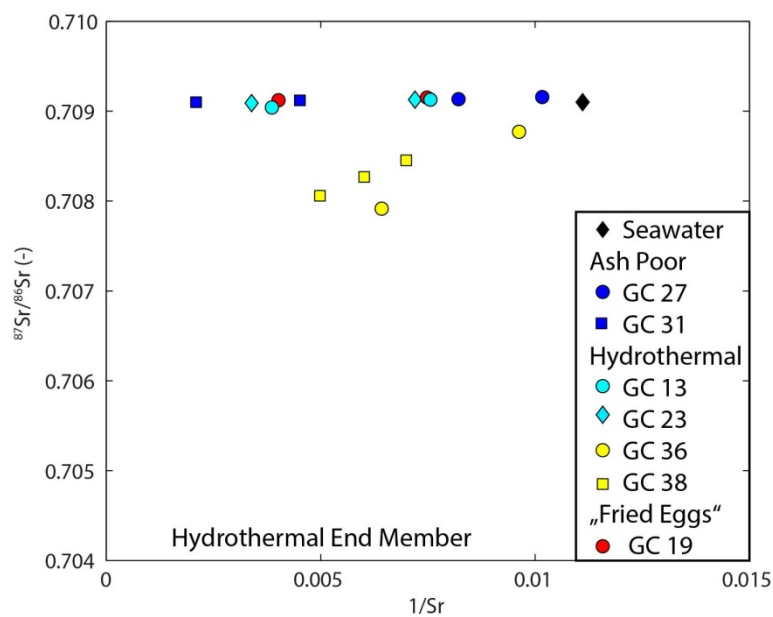


Figure III.3. ⁸⁷Sr/⁸⁶Sr vs 1/Sr for selected GCs, black diamond shows seawater composition

III.4.3 Head space gas

CO₂ measurements reveal no differences between GCs (Appendix B). All measured GCs show small concentrations with less than 2000 ppm. The highest measured values are in a hydrothermal GC38 with up to 4000 ppm.

III.4.3 Solid phase

All GCs were analyzed for their major element composition. A detailed list of solid phase data is given in the supplemental data 2. TOC concentrations are always below 1 % (Fig. III.4A), whereas CaCO₃ shows an increase with depth of up to 85 wt% (Fig III.4B). The GCs are similar in their major element composition (Fig. III.5). However, GCs taken in the TR and two GCs from the western Plateau (GC29 and GC31) are lower in K₂O and higher in CaO* and Na₂O. CaO* is the Ca bound to silicates and was calculated subtracting Ca bound to

carbonates from total Ca, after $\text{CaCO}_3 = 8.33 * \text{TIC}$ (Scholz et al., 2013). These cores are also marked by a lower K/Al ratio (Fig. III.4C). The chemical index of alteration (CIA, Nesbitt and Young, 1982) has been applied to characterize the effects of early diagenesis on sediment composition. It is calculated by: $\text{CIA} = \text{Al}_2\text{O}_3 / (\text{Al}_2\text{O}_3 + \text{K}_2\text{O} + \text{Na}_2\text{O} + \text{CaO}^*) \times 100$. The CIA is generally low for all GCs with values of 50 % to 60 % (Fig. III.5).

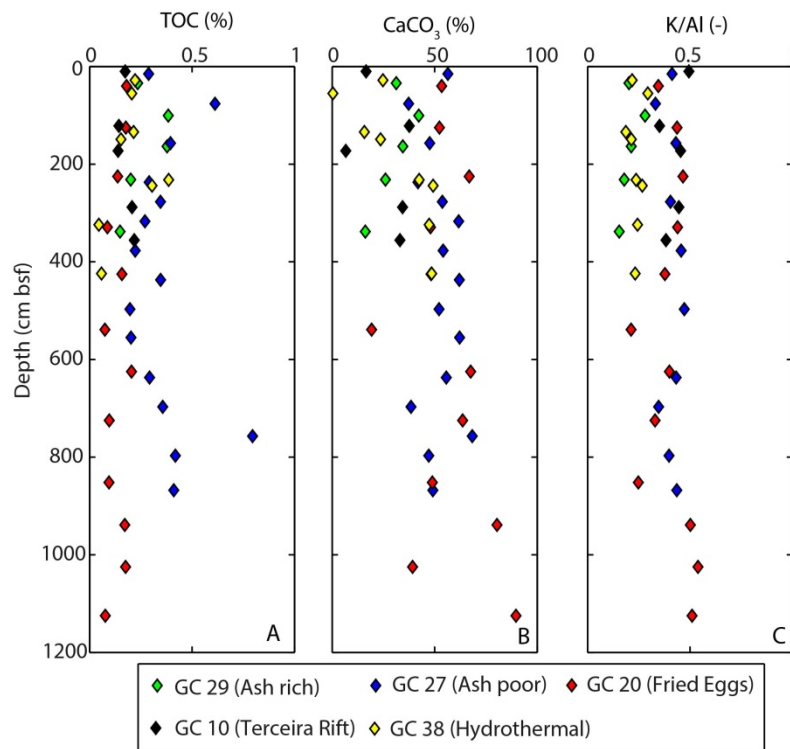


Figure III.4. Depth profiles solids TOC, CaCo3, K/Al for a representative GC for each defined group; ash rich GCs (GC29); ash poor GCs (GC27); Fried Eggs (GC20), Terceira Rift (GC10); hydrothermal GCs (GC38)

For each group, a representative core has been analysed by XRD for mineral composition analyses. In general, data from all GCs reveal a similar mineral composition and distribution. The main mineral phases are calcite, aragonite, feldspar, some pyroxene and minor illite and quartz. XRD pattern of the mineralogical composition for each core can be found in the appendix B.

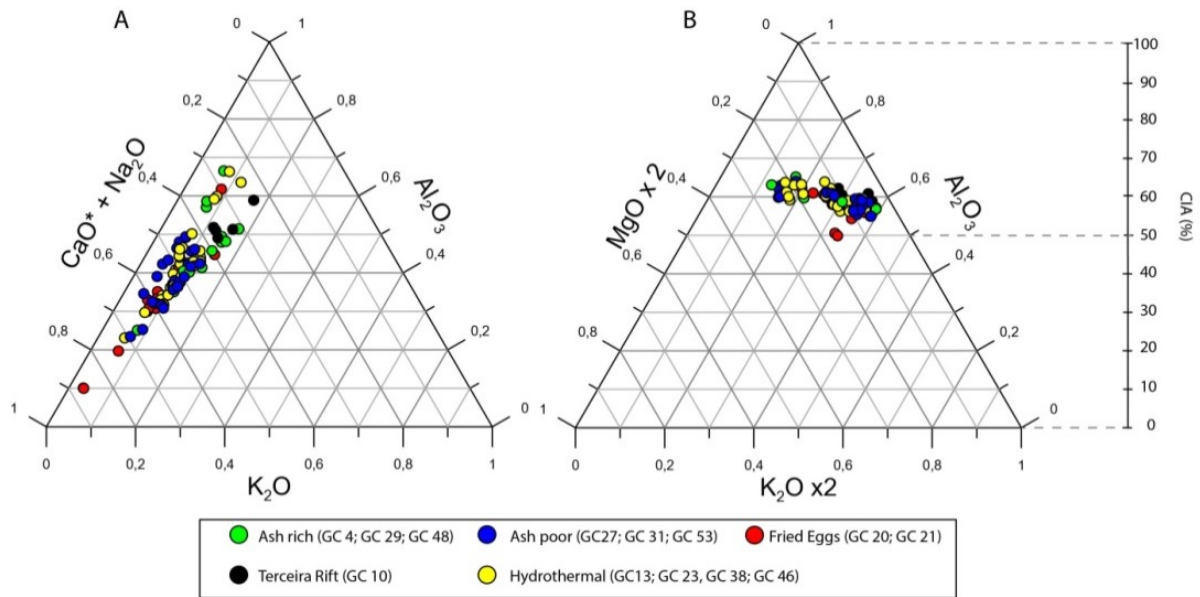


Figure III.5. Solid Phase Tertiary plot with CIA

III.4.4 Seismic lines

III.4.4.1 M113-75

Seismic profile M113-75 runs perpendicular to the TR (Fig. III.6A). A sequence of sub-parallel reflections with strong reflection amplitudes overlies wavy reflections with generally much weaker reflection amplitudes. However, high-amplitude reflection patches are interspersed. The northeastern part of the profile reveals reflections from a cone-like feature. Reflections from its summit crosscut the seafloor reflection, which is typical of out-of-plane reflections. The profile does obviously not directly cross the summit. Ca. 300 ms TWT beneath the seafloor, strong reflections onlap at both sides of the cone. The wavelet has the same polarity than the seafloor reflection. On the southwestern flank, reflection amplitudes above the strong reflection are increased. Assuming an average p-wave velocity of 1800-2200 m/s, the 300 ms TWT correspond to a depth of approximately 270 to 330 m.

III.4.4.2 M113-73

The GC36 site had been determined from profile M113-73 that runs between and parallel to the islands of Pico and Sao Jorge (Fig. III.6B). The upper 100 ms TWT show strong reflection amplitudes are wavy and partly disrupted by low amplitude reflections. 120 ms TWT and 200 ms TWT beneath the seafloor phase reversed reflections are present.

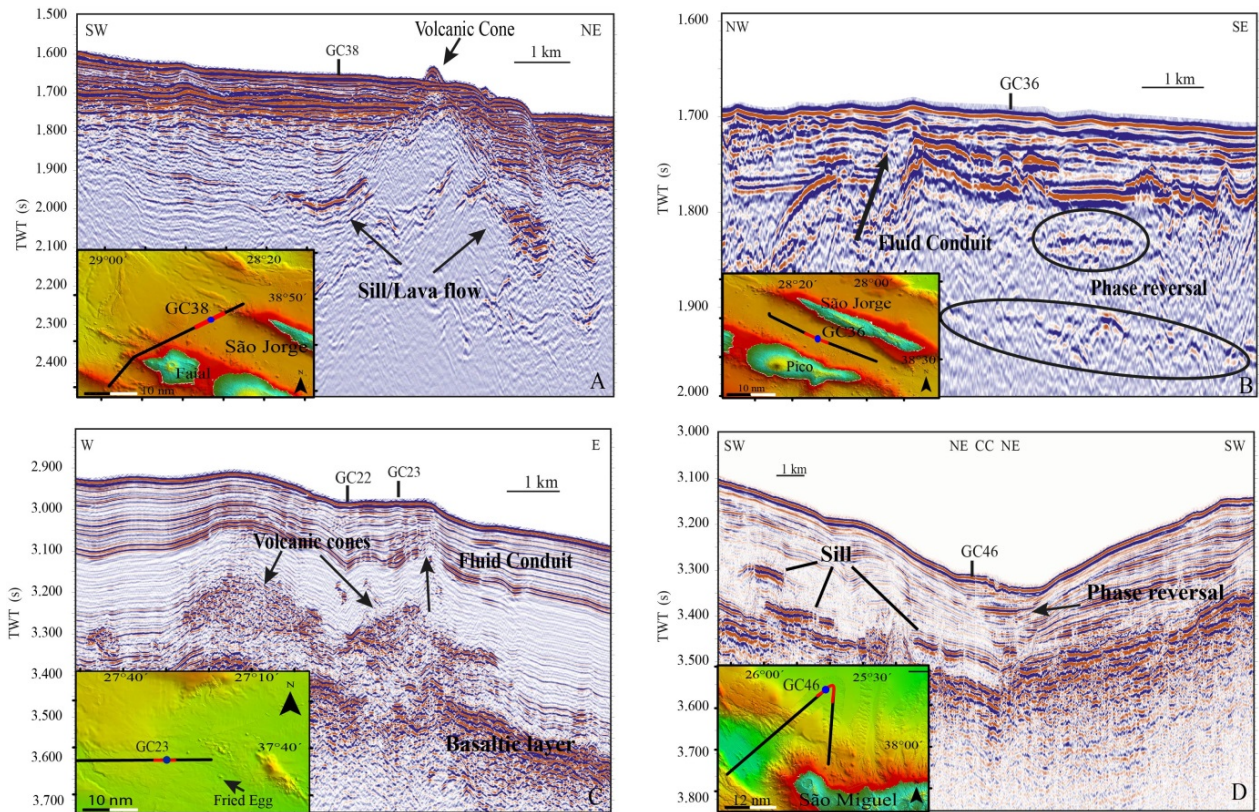


Figure III.6. Multi-channel seismic lines over assumed hydrothermal systems; A: GC38; B: GC36; C: GC23; D: GC46;

III.4.4.3 M113-17

GC23 is located in the central plateau (Fig. III.6C). A package of high reflection amplitudes is covered by ca. 500 ms TWT of wavy strata. The upper third reveals stronger reflection amplitudes than the lower part. Intercalated into these lower strata there are two cone-like high-amplitude reflection packages. Strata to the sides terminate against these packages. The upper third of the sediment cover reveals amplitude anomalies up to the seafloor.

III.4.4.4 M79-20/21

The GC46 site is located close to the northern margin of the TR but outside of it (Fig. III.6D). Reflections in the upper 300 ms TWT are generally low but include several segments of high-amplitude reflections with a positive polarity. Just close to the coring site a strong reflection patch with a reversed polarity is present.

III.4.4.5 M79-30

The seismic line M79-30 is located west of the Monaco Bank (Fig. III.7) and was previously described in Weiß et al. (2016). The area is highly affected by mass transport deposits. Between 320 and 350 ms TWT phase reversed reflections are present.

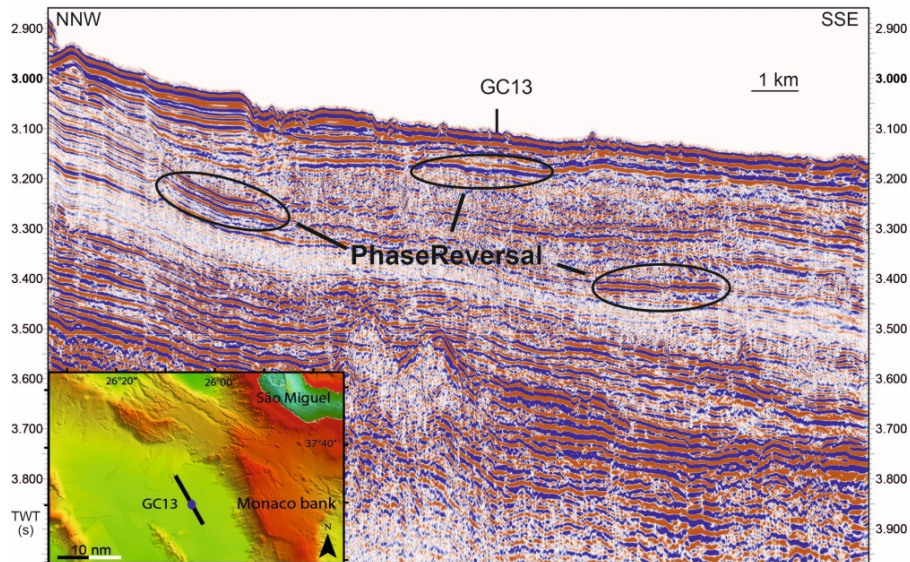


Figure III.7. Multi-channel seismic line M79-30 crossing over core location of GC13. No sill implements are visible in the subsurface, but phase reversal indicating free gas is present

III.5 Discussion

In the following, we will discuss general patterns of pore waters from surface sediments of the Azores Plateau and of three basins of the Terceira Rift. Furthermore, we will show evidence of sediment hosted hydrothermal systems on the Azores Plateau remote the Mid-Atlantic Ridge and will put those findings in a geological context of this region.

III.5.1 Background GCs Azores Plateau

III.5.1.1 Ash rich GCs

Overall, we sampled 5 GCs where we could not observe any prominent change in pore water geochemistry with depth. The sample locations are distributed across the plateau, all GCs were taken in areas with massive ash layers in the near surface sediments (Fig. III.8). The core recovery was less than 5 m (Table III.1) for each GC.

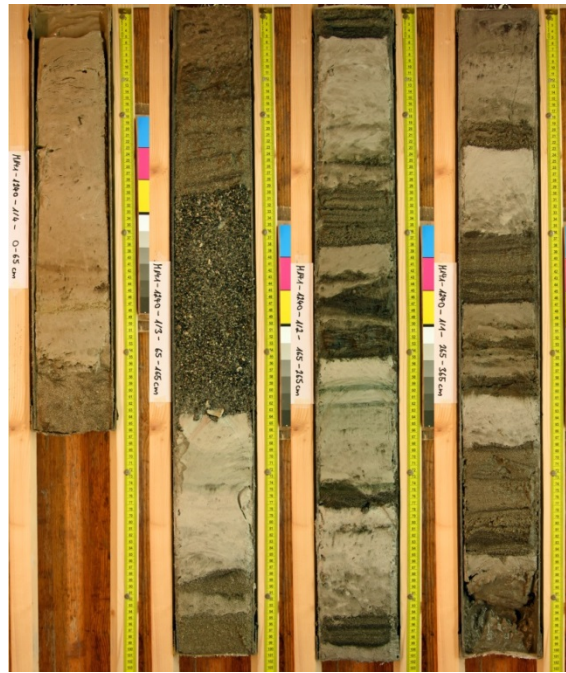


Figure III.8. Core section photo for ash rich GC48

Based on XRD measurements, no significant changes in the mineralogy compared to other GCs can be observed (no typical alteration minerals like Mg-smectites and zeolites are present; see Appendix B). In addition, a first optical description of the ash layers in our GCs shows that they generally contain fresh glass. Thus, we assume that alteration has not started in the near surface sediments yet. This could be caused by several phenomena. The TOC content is low in the upper meters (Fig. III.4A) and organic matter breakdown, providing CO₂ as a main driver for ash alteration (Wallmann et al., 2008), is lacking or is simply too low. This interpretation is supported by low CO₂ concentrations in the GCs. Similar findings are presented by Schacht et al. (2008) who studied the impact pore water of ash weathering on the pore water geochemistry surface sediments offshore Nicaragua.

III.5.1.2 Ash poor GCs

All GCs in this group are marked by the absence of prominent ash layers in the near surface sediments (Fig. III.9), which led to higher recovery of sediments with up to 11 m. Compared to ash rich GCs, all of the GCs show a decrease in pore water Ca with increasing depth, reaching concentrations as low as 7 mM (GC31). A comparison of the Ca concentration in the upper 4 m between ash rich and ash poor cores is provided in Fig. III.10. Consequently, the Ca decrease cannot be explained by the difference in core recovery. The observed decrease in Ca could have two reasons.



Figure III.9. Core section photo for ash poor GC6

A major process removing Ca from pore waters is the precipitation of calcium carbonate. Breakdown of organic matter results in higher bicarbonate production, which can lead to the precipitation of CaCO_3 (Han et al., 2004; Wallmann et al., 2006). The combined processes typically result in decreasing Ca and SO_4 concentrations and an increase of TA in pore water. An increase in TA cannot be observed in the GCs, however, SO_4 shows a trend to lower concentrations. Generally, the organic matter input on the Azores Plateau is low due to low productivity conditions in central Atlantic Ocean (Fig III.4A), which contradict the hypothesis. To check the plausibility if organic matter degradation can act as driver of the observed pore water patterns we applied a numerical reaction transport model. The model includes SO_4 reduction and anaerobic oxidation of methane (AOM), a table with input parameter and boundary conditions can be found in the Appendix B. With the chosen parameters the modeled pore water profiles of Ca, SO_4 and TA profiles could be fitted to the measured concentrations in the upper sediments. Furthermore the results suggest that the Sulfate Methane Transition Zone (SMTZ) could be located at a sediment depth of about 120 mbsf (Fig. III.11 A-C). The depth of SMTZ can vary depending on numerous factors, such as changes in the sedimentation rates and the sediment composition over time and/or the presence of pore water advection. Hence, a deep sourced AOM can cause the observed pore water profiles. However, in the setting of the Azores Plateau also another process could cause the deviations.

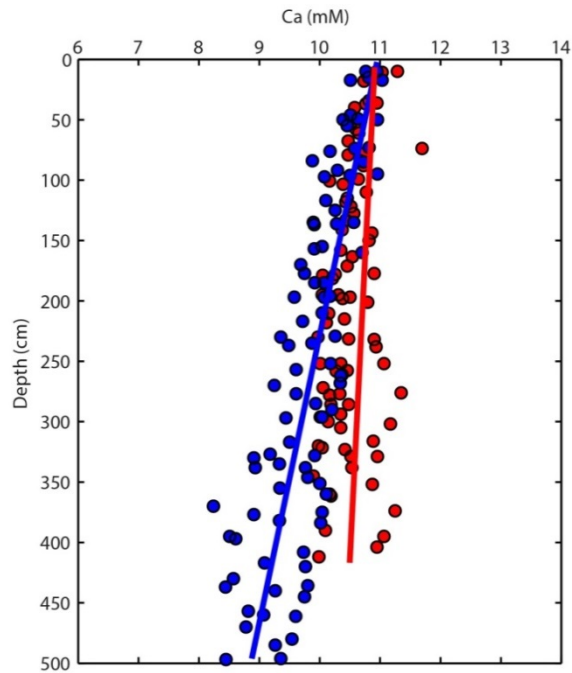


Figure III.10. Ca depth profiles for upper 4 m bsf for GCs from ash rich GCs (red) and ash poor GCs (blue)

An alternative explanation for the observed Ca depletion could offer the weathering of volcanic ash which may lead to calcite and zeolite formation. Near surface sediments do not show any major ash layers, but in deeper sediments volcanic deposits may exist. In DSDP Site 397 near the Canary Islands, De Ros et al. (1997) observed weathering of ash and bioclastic components with seawater to diagenetic calcite and phillipsite consuming pore water Ca. Similar reactions have been observed at other locations (Karpoff et al., 2002; Karpoff et al., 2007). A similar process of deeper located ash layers could be possible on the Azores Plateau as well. However, no data on ash plume dispersal for older Pleistocene volcanic eruptions are available.

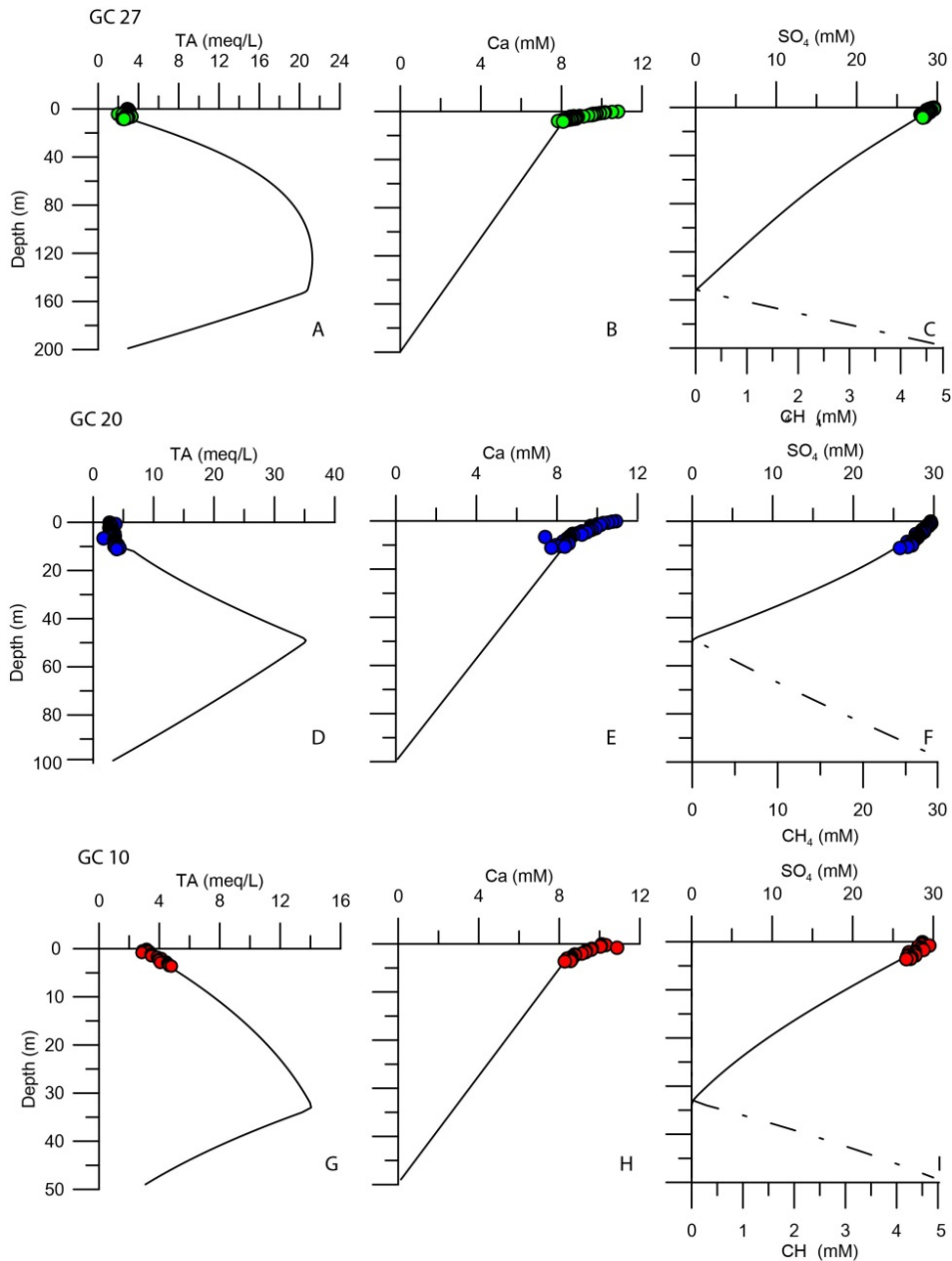


Figure III.11. Results of AOM model A: Ash poor GC27; B: Fried Eggs GC20 and C: Terceira Rift GC10

In conclusion, we can show that Ca deviations are caused by processes occurring below the cored sediment section. Reactions in deeper parts of the sediments are likely contributing to the observed pore water pattern. Presumably, carbonate precipitation induced by AOM and/or ash alteration below the cored depth are responsible for the observed down-core decrease in dissolved Ca.

A second prominent deviation in the pore waters is the Sr enrichment in all ash-poor GCs from the Azores Plateau (Fig. III.2). GC31 is specifically remarkable with a vast enrichment in pore water Sr up to nearly 500 μM , and thus being four times higher than present-day seawater (91 μM). The most straightforward way of interpreting of the deviations

is Sr enrichment through calcium carbonate recrystallization, e.g. the transformation of aragonite to calcite (Casella et al., 2017; Katz et al., 1972). This interpretation is supported by XRD analyses for GC31 revealing that the fraction of aragonite in the sediments is decreasing with depth while the calcite fraction is similarly increasing (Fig. III.12). For Ca this process is isochemical while Sr is released into the ambient pore water (e.g. Richter and DePaolo, 1987). Sr released from carbonates has a distinct $^{87}\text{Sr}/^{86}\text{Sr}$ signature of the seawater of the time the carbonate minerals precipitated. $^{87}\text{Sr}/^{86}\text{Sr}$ signature of GCs does show only small decreases from present day seawater (0.709175) to the minimum $^{87}\text{Sr}/^{86}\text{Sr}$ of 0.709100 in GC31 (Fig. III.3). According to Banner (2004) this $^{87}\text{Sr}/^{86}\text{Sr}$ value was present ~ 1.5 Ma ago. Taking the average sedimentation rate of 3.5 cm ka^{-1} for the Azores Plateau (Vlag et al., 2004), the signal could originate from the upper 50 m bsf.

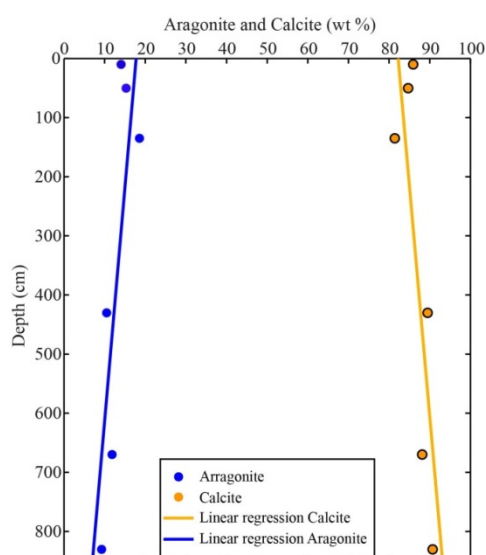


Figure III.12. XRD results for Aragonite and calcite content of GC31 vs. depth

As a proof of concept we applied a numerical model for carbonate recrystallization (Schmidt et al., 2018). The results show that modeled Sr concentrations reproduce measured Sr in the upper sediment column (Fig. III.13 A and B). Also a small decrease in $^{87}\text{Sr}/^{86}\text{Sr}$ can be achieved by the model. Differences in the Sr enrichment in the GCs can be caused by variations in the bulk calcium carbonate content of the sediments and the aragonite to calcite ratio.

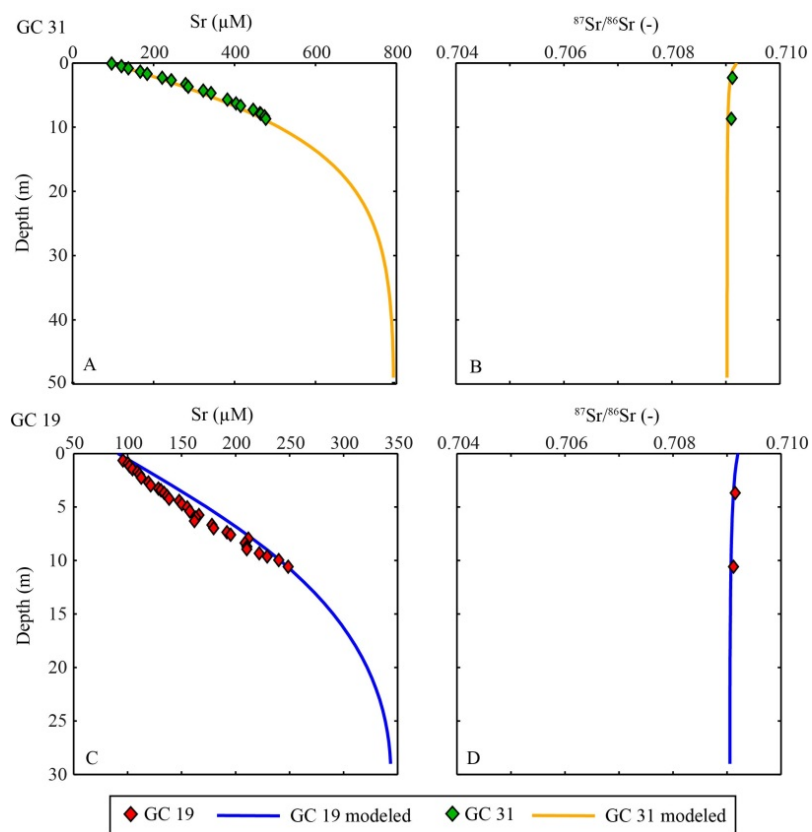


Figure III.13. Modelling results for calcium carbonate recrystallization of Sr and $^{87}\text{Sr}/^{86}\text{Sr}$ for GC31 (A+B) and GC19 (C+D)

III.5.1.3 “Fried Eggs” GCs

The “Fried Eggs” are several Ma old volcanic cones surrounded by moat channels present on the seafloor on the central southern Azores Plateau (Stakemann et al., 2017). In the perimeter of up to 50 km we sampled six GCs, based on multi-channel seismic profiles, showing fluid escape structures and other indications for hydrothermal activity. Five of the GCs do not show signs of a hydrothermal imprint, GC23 has an indication of hydrothermal fluids and will be discussed in section III.5.4 and GC25 is rich in thick ash layers in the near surface sediments.

Sediments sampled in the other four GCs can be compared to the ash poor GCs. Sampled pore waters are also marked by a decrease in Ca but show a pronounced down-core decrease in SO_4 . The TOC content is slightly higher here compared to the other GCs. The observed patterns in pore water composition (Fig. III.2) can be explained by the two processes, AOM and ash alteration at larger subsurface depth, as discussed in the previous section.

Numerical simulations of organic matter breakdown and AOM for those cores resulted in a SMTZ depth of 50 m bsf (GC20; Fig. III.11 D - F). Compared to the other ash poor GCs, this is about 70 meters shallower. This difference could be explained by the slightly higher organic matter in the sediments, or elevated temperatures induced by magmatic activity might have warmed the sediments what could result in enhanced organic matter break down (e.g. Berndt et al., 2016). However, as discussed before also weathering of deeper volcanic ash layers cannot be excluded.

GCs taken close to the “Fried Eggs” all show strong Sr enrichments of up to $\sim 230 \mu\text{M}$ (Fig III.2). The observed Sr increase is stronger compared to the other GCs taken on the Azores Plateau. This increase can be explained again by calcium carbonate recrystallization as shown by the recrystallization model (Fig. III.13 C and D).

III.5.2 Background GCs Terceira Rift

The Terceira Rift marks the ~ 150 km wide, diffuse Eurasian Nubian plate boundary (Fig. III.1; Marques et al., 2013). Several basins are located within this diffuse zone. In three basins, short (< 3 m) sediment cores could be recovered. The presence of active volcanoes within short distance has resulted in massive volcanic deposits in the near surface sediments. Pore waters in the basins of the Terceira Rift are remarkably different from those retrieved at other locations on the Azores Plateau. All GCs show a small increase in TA, while SO_4 , Ca and Sr are decreasing. As discussed above, the increase in TA can be caused by organic matter degradation and AOM. Numerical modelling shows that AOM is likely to occur here in 30 m sediment depth (GC10; Fig III.11 G- I). Compared to the GCs on the Azores Plateau, this is the shallowest subsurface SMTZ. One explanation could offer a higher heat flux in the basins of the rift than on the Azores Plateau. Unfortunately, no heat flow data are available either for the Terceira rift or for the Azores Plateau, but in general rifts show higher heat flow values than the surrounding plate (Morgan, 1982). Again, higher temperatures could cause an enhanced organic matter breakdown (Wellsbury et al., 1997), resulting in the location of the SMTZ closer to the seafloor. A major difference to background GCs on the Azores Plateau is the decrease in Sr downcore in the basins of the Terceira Rift. The cored sediment sections there contain a higher amount of ash and less hemi-pelagic sediments and calcium carbonate recrystallization is apparently inhibited, which may explain the relatively low Sr concentrations compared to the other GCs. Furthermore, the decrease in Ca indicates a precipitation of authigenic carbonates in the subsurface, which could also cause a decrease of Sr by co-precipitation.

III.5.3 Hydrothermally influenced GCs

In general, the Azores Plateau is a magmatically active region, but recent magmatic activity has been largely limited to the islands of the Azores Archipelago together with a small number of submarine eruptions. Magma emplacement is accompanied by volcanic-tectonic seismicity (Lengliné et al., 2008) and can be therefore an indicator for intrusion activity in the subsurface. The most recent magmatic activity of the Azores Plateau is known from the island of Faial (1958, Machado et al., 1962), and submarine eruptions offshore of the islands of Pico (1963) and São Jorge (1964). Accordingly, high seismicity has been recorded in this area for the past 30 years (Gaspar et al., 2015).

Typical Mid-Oceanic Ridge hydrothermal fluids are characterized by the absence of Mg and SO₄, while Ca is enriched (e.g. Alt and Honnorez, 1984). In total, we sampled four gravity cores (GC23, GC36, GC38 and GC46) on the Azores Plateau showing a similar pattern in the pore waters of shallow subsurface sediments (Fig III.2).

GC38 sampled west of São Jorge and GC36 sampled between São Jorge and Faial, are both located within the diffuse plate boundary of the Terceira Rift within the region of known submarine eruptions. GC23 and GC46 were sampled in regions with low seismic activity and no other signs of active magmatism.

In the following all GCs and their implication in the geological context of the Azores Plateau will be discussed.

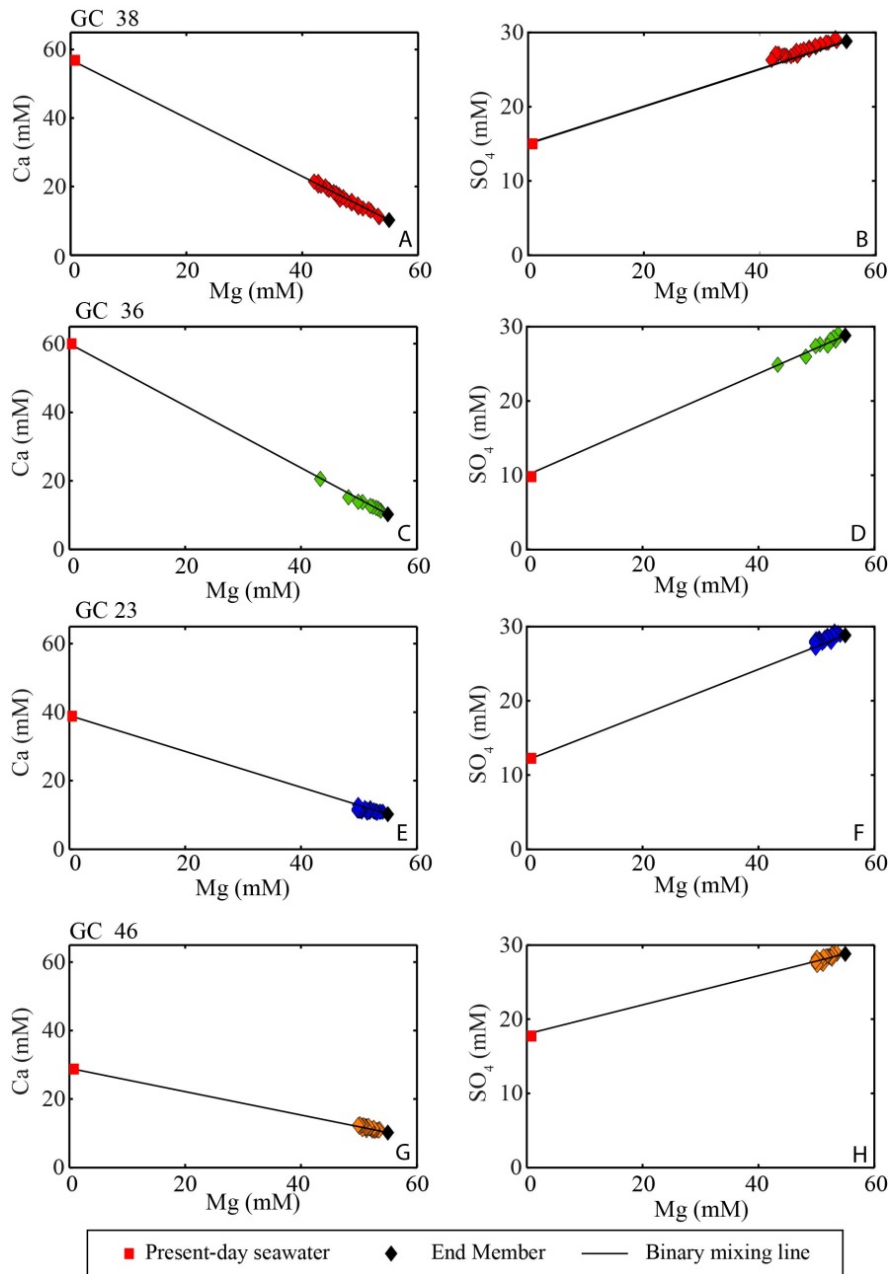


Figure III.14. Endmember plots of Mg, Ca and SO₄ for GC38 (A+B), GC36 (C+D), GC23 (E+F) and GC46 (G+H)

III.5.3.1 Hydrothermal vent west of São Jorge (GC38)

Close to the sampling location a cone-like feature (Fig. III.6A) is present at the seafloor, likewise to volcanic cones as described by Weiß et al. (2015). The uppermost sediments, characterized by high reflection amplitudes, have been considered as hemi-pelagic sediments with intercalated ashes. The strata with low reflection amplitudes below represent pelagic sediments. The strong reflections at both flanks at about 300 ms TWT beneath seafloor have a positive polarity and are consequently caused by an intercalated layer, which is characterized by high acoustic impedance. We consequently interpret these strong

reflections as either as sills or lava flows. Amplitude anomalies above the sills/lava flows SW of the cone had been considered as a possible indicators for rising fluids when selecting the GC38 site.

Pore waters at this location show the strongest variation in their major element composition and isotopic signature compared to present day seawater. The calculated EM fluid composition shows a maximum Ca concentration of 60 mM (Fig III.14 A). In contrast, SO₄ does not show a quantitative removal from fluids, with an EM concentration of 15 mM (Fig. III.14B). One explanation for the calculated EM concentrations could be an additional Mg sink and Ca source. Hydrothermal fluids of sediment hosted systems are normally modified by interaction with the ambient sediment. For example weathering of intercalated ashes of the hemi-pelagic sediments would cause an Mg removal and Ca release into the ambient pore water (Schacht et al., 2008).

⁸⁷Sr/⁸⁶Sr ratios for GC38 are decreasing from modern seawater values to 0.708058 in 454 cm bsf (Fig. III.3). The hydrothermal fluid EM for ⁸⁷Sr/⁸⁶Sr can generally be assumed to be below 0.7040 (Palmer and Edmond, 1989), whereas the calculated EM ratio for GC38 is 0.7072. This value implies a mixing of Sr from various sources in GC38. Hemi-pelagic sediments at this location can be also affected by calcium carbonate recrystallization as shown for the other GCs. A mixing between ambient pore water affected by carbonate recrystallization with a ⁸⁷Sr/⁸⁶Sr of about 0.7091 and a hydrothermal fluid with an lower ⁸⁷Sr/⁸⁶Sr could explain the calculated EM for the fluid.

Overall, GC38 has strong indications for a hydrothermal system in the vicinity of the sample location.

III.5.3.2 Hydrothermal vent between São Jorge and Pico (GC36)

Seismic Profile M113-73 shows that phase reversals are present in the subsurface (Fig. III.6B), beneath sampling location of GC36. Phase reversals are caused by negative acoustic impedance contrasts and indicate fluids, trapped by, e.g., impermeable strata. When selecting the coordinates of GC36 we considered disrupted reflections above as potential fluid pathways. The potential heat source however is not resolved in the seismic profile indicating a deep sourced fluid circulation.

Fluid composition shows a strong deviation from seawater for GC36 (Fig. III.2). The calculated EM for Ca is about 60 mM (Fig III.14C). The SO₄ decrease in GC36 is stronger than in GC38 with an EM concentration of 10 mM (Fig 1 III.4D). The ⁸⁷Sr/⁸⁶Sr EM for GC36

is with 0.7067 slightly lower than in GC38. Again, similar to GC38 a modification of hydrothermal fluids by sediments is likely.

III.5.3.3 “Fried Eggs” hydrothermal vent (GC23)

GC23 was taken in the vicinity (~40 km distance) of the volcanic “Fried Egg” structures. As discussed in section III.5.1.3 several GCs were sampled showing indications for deep AOM, with decreasing Ca and SO₄ concentrations and a vast Sr enrichment caused by calcium carbonate recrystallization. GC23, in contrast, shows a different fluid pattern with depth. The slightly decreasing Mg and SO₄ and increasing Ca could be explained by hydrothermal input. The calculated EM for GC23, however, shows a smaller increase in Ca and decrease in SO₄ compared to GC36 and GC38 (Fig. III.14 E and F). However, the Sr-enrichment is much stronger while the decrease in ⁸⁷Sr/⁸⁶Sr is not that pronounced (Fig. III.3). The high Sr concentrations can be explained by calcium carbonate recrystallization as discussed before for the other GCs in this area. For this hydrothermal vent this causes an admixture of Sr-enriched ambient pore waters carrying a higher ⁸⁷Sr/⁸⁶Sr signature, to the hydrothermal fluids.

In the seismic profile shown in Fig. III.6C, the lowermost high-amplitude reflection unit is considered as a basaltic layer, representing the uppermost part oceanic crust. The low-reflection amplitude unit above comprises presumably hemi-pelagic or pelagic sediments. The upper sequence with high-reflection is interpreted as a mix of pelagic and ash layers. The cone-shaped high amplitude reflection packages represent either intrusions or extrusions. Since the pelagic layers laterally terminate at the cones, we favor the interpretation of extrusions such as volcanic cones.

Moreover, we can observe a fluid conduit reaching to the seafloor providing a fluid pathway to the surface. GC23 was sampled directly in the vicinity of such a fluid conduit. The GC22 core discussed above was taken in ~1 km distance. GC22 does not show any indications for admixing of hydrothermal fluids, implying a local fluid discharge near GC23.

Volcanic activity and magma ascent are typically accompanied by seismicity. In the past 30 years no seismic activity was recorded for this region (Gaspar et al., 2015). Furthermore, the volcanic cones are fully buried by sediments and must be several Ma old, thus present volcanic activity is unknown. However, emplacement of an igneous intrusion could have happened longer time ago. The time for cooling of such a body is highly dependent on various parameters such as size and ambient temperature. Modelling results of

Galerne and Hasenclever (2019) show that venting of hot fluids is still possible after some ten thousands of years. This could offer an explanation for the presence of hydrothermal fluids in the presently volcanically inactive region.

III.5.3.4 Hydrothermal vent north of the Hirondelle Basin (GC46)

Fluid composition of GC46 shows also a potential imprint of hydrothermal fluids. EM concentrations are comparable to GC23 (Fig III.14 G and H) with a Ca enrichment to 30 mM and a decrease in SO₄ to 20 mM for the EM.

The intercalated high-amplitude reflections with the same polarity than the seafloor reflection are interpreted as sills (Fig. III.6D). The core location is north of the TR where only minor seismic activity is reported (Gaspar et al., 2015), indicating minor magmatic activity there. No submarine eruptions are reported for this region. Similar to GC23, an emplacement of the observed sills, could have happened long time ago and the observed intrusions may be several thousand years old. This GC shows only weak indications of hydrothermal fluid discharge, but based on the seismic profile there is some potential for active fluid venting in the area.

III.5.3.5 West of Monaco Bank (GC13)

For GC13, taken west of the Monaco Bank, we observe slightly decreasing SO₄ and Mg concentrations without increasing Ca concentrations with depth. Sr concentrations are increasing while the ⁸⁷Sr/⁸⁶Sr shows only a minor decrease with respect to seawater. The multi-channel seismic profile M79-30 does not show any intrusions in this area (Fig. III.7). However, three patches where phase reversal occurs can be observed in the same sediment layers. A magmatic body could have been emplaced in deeper crust driving a fluid circulation cell. However, the seismic profile does not show any indications for existing fluid conduits in the sediment. The Monaco bank is located in a distance of ca. 100 km from the core location. According to Weiß et al. (2015) many sills and volcanic cones are present on the eastern site of this bank hosting possibly associated hydrothermal systems. The western flank of the Monaco Bank, facing to the sample location, is marked by numerous mass transport deposits (Weiß et al., 2016). The uneven surface in the seismic profile (Fig. III.7) indicates a mass transport deposit at this location, nevertheless, the deviations in the pore waters cannot be caused by such deposits. Taken all this together GC13 may be best explained by a hydrothermal input. However, either the weak fluid concentration represents traces of an extinct old hydrothermal system, or the sampling location is distal from the fluid vent.

III.6 Conclusions and Outlook

Surface sediments of the Azores Plateau show a broad range of pore water characteristics. The main findings are:

- There are indications for two hydrothermal systems between Pico, Faial and Sao Jorge. Fluids are characterised by a strong increase in Ca while Mg and SO₄ are depleted. Those findings are in line with multi-channel seismic interpretations of the two locations, where magmatic intrusions are present in the subsurface.
- Two other cores also indicate the existence of hydrothermal systems on the southern plateau and north of the Terceira Rift. Overall, the indications there are less pronounced, but multi-channel seismic records support the presence of hydrothermal circulation systems. However, those two systems are comparatively far away from regions where active magmatism has been postulated.
- Background GCs can be divided into two groups. GCs with thick ash layers present do not show any deviations of pore waters compared to seawater.
- GCs where thick ash layers were missing show in contrast a down core decrease in Ca and SO₄. These deviations could be caused either by organic matter degradation or weathering of deeper located ash deposits
- Calcium carbonate recrystallization is affecting most of the background sediments in the region resulting in enriched Sr concentrations in the pore fluids.

Overall, we present the first comprehensive pore water data set for the Azores Plateau which can serve as basis for future studies. Especially, indications for hydrothermal activity need to be further substantiated, which requires a more sophisticated sampling approach (high-resolution mapping, video-controlled sampling) than applied for the present study.

Acknowledgments, Samples, and Data

We would like to thank captain D. Korte and his crew for the excellent support on-board RV Meteor. Many thanks to our colleagues T. Schott, K. Meier E. Horstmann and T. Lux for their great help on board. We would also like to thank B. Domeyer, A. Bleyer, J. Heinze, and R. Surberg for on-shore analyses at GEOMAR. The cruise M141/1 was funded by the Deutsche Forschungsgemeinschaft (DFG) and the Bundesministerium für Bildung und Forschung (BMBF) with additional support of FLOWS (EU-COST ES 1301).

References

- Alt, J.C., Honnorez, J., 1984. Alteration of the upper oceanic crust, DSDP site 417: mineralogy and chemistry. *Contributions to Mineralogy and Petrology* 87, 149-169.
- Banner, J.L., 2004. Radiogenic isotopes: systematics and applications to earth surface processes and chemical stratigraphy. *Earth Science Review* 65, 141-194.
- Beier, C., Bach, W., Busch, A.V., Genske, F.S., Hübscher, C., Krumm, S.H., 2019. Extreme intensity of fluid-rock interaction during extensive intraplate volcanism. *Geochimica et Cosmochimica Acta* 257, 26-48.
- Beier, C., Haase, K.M., Abouchami, W., Krienitz, M.S., Hauff, F., 2008. Magma genesis by rifting of oceanic lithosphere above anomalous mantle: Terceira Rift, Azores. *Geochemistry, Geophysics, Geosystems* 9.
- Beier, C., Turner, S., Plank, T., White, W., 2010. A preliminary assessment of the symmetry of source composition and melting dynamics across the Azores plume. *Geochemistry, Geophysics, Geosystems* 11.
- Berndt, C., Hensen, C., Mortera-Gutierrez, C., Sarkar, S., Geilert, S., Schmidt, M., Liebetrau, V., Kipfer, R., Scholz, F., Doll, M., 2016. Rifting under steam—How rift magmatism triggers methane venting from sedimentary basins. *Geology* 44, 767-770.
- Bonath, E., 1990. Not so hot" hot spots" in the oceanic mantle. *Science* 250, 107-111.
- Cardigos, F., Colaço, A., Dando, P.R., Ávila, S.P., Sarradin, P.M., Tempera, F., Conceição, P., Pascoal, A., Serrão Santos, R., 2005. Shallow water hydrothermal vent field fluids and communities of the D. João de Castro Seamount (Azores). *Chemical Geology* 224, 153-168.
- Casella, L.A., Griesshaber, E., Yin, X., Ziegler, A., Mavromatis, V., Müller, D., Ritter, A.-C., Hippler, D., Harper, E.M., Dietzel, M., 2017. Experimental diagenesis: insights into aragonite to calcite transformation of *Arctica islandica* shells by hydrothermal treatment. *Biogeosciences* 14, 1461-1492.
- Couto, R.P., Rodrigues, A.S., Neto, A.I., 2015. Shallow-water hydrothermal vents in the Azores (Portugal). *Revista de Gestão Costeira Integrada-Journal of Integrated Coastal Zone Management* 15.
- De Ros, L.F., Morad, S., Al-Aasm, I.S., 1997. Diagenesis of siliciclastic and volcanoclastic sediments in the Cretaceous and Miocene sequences of the NW African margin (DSDP Leg 47A, Site 397). *Sedimentary Geology* 112, 137-156.
- Galerie, C., Hasenclever, J., 2019. Distinct degassing pulses during magma invasion in the stratified Karoo Basin—New insights from hydrothermal fluid flow modelling. *Geochemistry, Geophysics, Geosystems*.
- Gaspar, J., Queiroz, G., Ferreira, T., Medeiros, A., Goulart, C., Medeiros, J., 2015. Earthquakes and volcanic eruptions in the Azores region: geodynamic implications from major historical events and instrumental seismicity. *Geological Society, London, Memoirs* 44, 33-49.

- Gieskes, J.M., Lawrence, J.R., 1981. Alteration of volcanic matter in deep-sea sediments: evidence from the chemical composition of interstitial waters from deep-sea drilling cores. *Geochimica et Cosmochimica Acta* 45, 1687-1703.
- Haase, K.M., Beier, C., 2003. Tectonic control of ocean island basalt sources on São Miguel, Azores? *Geophysical Research Letters* 30.
- Han, X., Suess, E., Sahling, H., Wallmann, K., 2004. Fluid venting activity on the Costa Rica Margin: New results from authigenic carbonates. *International Journal of Earth Sciences* 93, 596-611.
- Hübscher, C., 2013. *Tragica: Cruise No. M79/2, August 26-September 21, 2009, Ponta Delgada (Azores/Portugal)-Las Palmas (Canary Islands/Spain). DFG-Senatskomm. f. Ozeanographie.*
- Hübscher, C., Beier, C., Al-Hseinat, M., Batista, L., Blum, M., Bobsin, M., 2016. Azores Plateau—Cruise No. M113/1—December 29, 2014—January 22, 2015—Ponta Delgada (Portugal)—Ponta Delgada (Portugal). *METEOR-Berichte M 113.*
- Hübscher, C., Gohl, K., 2014. Reflection/Refraction seismology. *Encycl. Mar. Geosciences.*
- Karpoff, A.M., Destrigneville, C., Bartier, D., Déjardin, P., 2002. Phyllosilicates and zeolite assemblages in the carbonate periplatform of the Great Bahama Bank: origin and relation to diagenetic processes (ODP Leg 166, Sites 1006 and 1007). *Marine Geology* 185, 55-74.
- Karpoff, A.M., Destrigneville, C., Stille, P., 2007. Clinoptilolite as a new proxy of enhanced biogenic silica productivity in lower Miocene carbonate sediments of the Bahamas platform: Isotopic and thermodynamic evidence. *Chemical Geology* 245, 285-304.
- Katz, A., Sass, E., Starinsky, A., Holland, H., 1972. Strontium behavior in the aragonite-calcite transformation: An experimental study at 40–98 C. *Geochimica et Cosmochimica Acta* 36, 481-496.
- Kueppers, U., Beier, C., 2018. *Volcanoes of the Azores: Revealing the Geological Secrets of the Central Northern Atlantic Islands.* Springer.
- Lengliné, O., Marsan, D., Got, J.L., Pinel, V., Ferrazzini, V., Okubo, P.G., 2008. Seismicity and deformation induced by magma accumulation at three basaltic volcanoes. *Journal of Geophysical Research: Solid Earth* 113.
- Machado, F., Parsons, W.H., Richards, A.F., Mulford, J.W., 1962. Capelinhos eruption of Fayal volcano, Azores, 1957–1958. *Journal of Geophysical Research* 67, 3519-3529.
- Marques, F., Catalão, J., DeMets, C., Costa, A., Hildenbrand, A., 2013. GPS and tectonic evidence for a diffuse plate boundary at the Azores Triple Junction. *Earth and Planetary Science Letters* 381, 177-187.
- Marques, F., Scott, S., Madureira, P., Conceição, P., Lourenço, N., Rosa, C., 2012. The Terceira Rift, Azores: a melt inclusion study of submarine lavas.
- Marques, F.O., Hildenbrand, A., Hübscher, C., 2018. Evolution of a volcanic island on the shoulder of an oceanic rift and geodynamic implications: S. Jorge Island on the Terceira Rift, Azores Triple Junction. *Tectonophysics* 738-739, 41-50.
- Martín, J., 2004. *XPowderX™*, Version 2017.01.xx ed. XPowder Software, Granada, Spain.

Métrich, N., Zanon, V., Créon, L., Hildenbrand, A., Moreira, M., Marques, F.O., 2014. Is the 'Azores hotspot' a wet spot? Insights from the geochemistry of fluid and melt inclusions in olivine of Pico basalts. *Journal of Petrology* 55, 377-393.

Morgan, P., 1982. Heat flow in rift zones. *Continental and oceanic rifts* 8, 107-122.

Nesbitt, H.W., Young, G., 1982. Early Proterozoic climates and plate motions inferred from major element chemistry of lutites. *Nature* 299, 715.

Palmer, M.R., Edmond, J.M., 1989. The strontium isotope budget of the modern ocean. *Earth and Planetary Science Letters* 92, 11-26.

Richter, F.M., DePaolo, D.J., 1987. Numerical models for diagenesis and the Neogene Sr isotopic evolution of seawater from DSDP Site 590B. *Earth and Planetary Science Letters* 83, 27-38.

Schacht, U., Wallmann, K., Kutterolf, S., Schmidt, M., 2008. Volcanogenic sediment-seawater interactions and the geochemistry of pore waters. *Chemical Geology* 249, 321-338.

Schilling, J.-G., 1975. Azores mantle blob: rare-earth evidence. *Earth and Planetary Science Letters* 25, 103-115.

Schmidt, C., Burwicz, E., Hensen, C., Wallmann, K., Martinez-Loriente, S., Gracia, E., 2018. Genesis of mud volcano fluids in the Gulf of Cadiz using a novel basin-scale model approach. *Geochimica et Cosmochimica Acta* 243, 186-204.

Schmidt, C., Hensen, C., Wallmann, K., Liebetrau, V., Tatzel, M., Schurr, S.L., Kutterolf, S., Haffert, L., Geilert, S., Hübscher, C., Lebas, E., Heuser, A., Schmidt, M., Strauss, H., Vogl, J., Hansteen, T., In rev. Origin of high Mg and SO₄ fluids in sediments of the Terceira Rift, Azores – indications for caminite dissolution in a waning hydrothermal system. *Geochemistry, Geophysics, Geosystems*.

Scholz, F., Hensen, C., Schmidt, M., Geersen, J., 2013. Submarine weathering of silicate minerals and the extent of pore water freshening at active continental margins. *Geochimica et Cosmochimica Acta* 100, 200-216.

Scholz, F., Löscher, C.R., Fiskal, A., Sommer, S., Hensen, C., Lomnitz, U., Wuttig, K., Göttlicher, J., Kossel, E., Steininger, R., 2016. Nitrate-dependent iron oxidation limits iron transport in anoxic ocean regions. *Earth and Planetary Science Letters* 454, 272-281.

Sommer, S., Linke, P., Pfannkuche, O., Schleicher, T., Schneider v. Deimling, J., Reitz, A., Haeckel, M., Flögel, S., Hensen, C., 2009. Seabed methane emissions and the habitat of frenulate tubeworms on the Captain Arutyunov mud volcano (Gulf of Cadiz). *Marine Ecology Progress Series* 382, 69-86.

Stakemann, J., Huebscher, C., Beier, C., Hildenbrand, A., Nomikou, P., Terrinha, P., Weiß, B., 2017. Structural evolution of deep-water submarine intraplate volcanoes/Azores, EGU General Assembly Conference Abstracts, p. 4406.

Vlag, P.A., Kruiver, P.P., Dekkers, M.J., 2004. Evaluating climate change by multivariate statistical techniques on magnetic and chemical properties of marine sediments (Azores region). *Palaeogeography, Palaeoclimatology, Palaeoecology* 212, 23-44.

- Vogt, P.R., Jung, W.Y., 2004. The Terceira Rift as hyper-slow, hotspot-dominated oblique spreading axis: A comparison with other slow-spreading plate boundaries. *Earth and Planetary Science Letters* 218, 77-90.
- Wallmann, K., Aloisi, G., Haeckel, M., Obzhirov, A., Pavlova, G., Tishchenko, P., 2006. Kinetics of organic matter degradation, microbial methane generation, and gas hydrate formation in anoxic marine sediments. *Geochimica et Cosmochimica Acta* 70, 3905-3927.
- Wallmann, K., Aloisi, G., Haeckel, M., Tishchenko, P., Pavlova, G., Greinert, J., Kutterolf, S., Eisenhauer, A., 2008. Silicate weathering in anoxic marine sediments. *Geochimica et Cosmochimica Acta* 72, 363-366.
- Weiß, B., Hübscher, C., Lüdmann, T., Serra, N., 2016. Submarine sedimentation processes in the southeastern Terceira Rift/São Miguel region (Azores). *Marine Geology* 374, 42-58.
- Weiß, B.J., Hübscher, C., Wolf, D., Lüdmann, T., 2015. Submarine explosive volcanism in the southeastern Terceira Rift/São Miguel region (Azores). *Journal of Volcanology and Geothermal Research* 303, 79-91.
- Wellsbury, P., Goodman, K., Barth, T., Cragg, B.A., Barnes, S.P., Parkes, R.J., 1997. Deep marine biosphere fuelled by increasing organic matter availability during burial and heating. *Nature* 388, 573 - 576.
- White, W.M., Tapia, M.D., Schilling, J.-G., 1979. The petrology and geochemistry of the Azores Islands. *Contributions to Mineralogy and Petrology* 69, 201-213.
- Widom, E., Shirey, S., 1996. Os isotope systematics in the Azores: implications for mantle plume sources. *Earth and Planetary Science Letters* 142, 451-465.
- Wolfram Research, I., 2018. *Mathematica*, 11.3 ed. Wolfram Research, Inc., Champaign, Illinois.

IV. Origin of high Mg and SO₄ fluids in sediments of the Terceira Rift, Azores - indications for caminite dissolution in a waning hydrothermal system

C. Schmidt¹, C. Hensen¹, K. Wallmann¹, V. Liebetrau¹, M. Tatzel^{2,3}, S.L. Schurr⁴, S. Kutterolf¹, L. Haffert¹, S. Geilert¹, C. Hübscher⁵, E. Lebas⁶, A. Heuser¹, M. Schmidt¹, H. Strauss⁴, J. Vogl²
and T. Hansteen¹

1 GEOMAR Helmholtz Centre for Ocean Research Kiel, 24148 Kiel, Germany

2 Bundesanstalt für Materialforschung und – prüfung, 12489 Berlin, Germany

3 Department of Earth and Planetary Sciences, University of California Santa Cruz, Santa Cruz, CA 95064, USA

4 Institut für Geologie und Paläontologie, Westfälische Wilhelms-Universität Münster, 48149 Münster, Germany

5 Institute of Geophysics, University of Hamburg, 20146 Hamburg, Germany

6 Institute of Geophysics, University of Kiel, 24118 Kiel, Germany

First published on 11. November 2019 in G-Cubed

Abstract

During R/V Meteor cruise 141/1, pore fluids of near surface sediments were investigated to find indications for hydrothermal activity in the Terceira Rift (TR), a hyper-slow spreading center in the Central North Atlantic Ocean. To date, submarine hydrothermal fluid venting in the TR has only been reported for the D. João de Castro seamount, which presently seems to be inactive. Pore fluids sampled close to a volcanic cone at 2800 m water depth show an anomalous composition with Mg, SO₄, and total alkalinity (TA) concentrations significantly higher than seawater and a nearby reference core. The most straightforward way of interpreting these deviations is the dissolution of the hydrothermally formed mineral caminite (MgSO₄ · 0.25Mg(OH)₂ · 0.2H₂O). This interpretation is corroborated by a thorough investigation of fluid isotope systems ($\delta^{26}\text{Mg}$, $\delta^{30}\text{Si}$, $\delta^{34}\text{S}$, $\delta^{44/42}\text{Ca}$, and $^{87}\text{Sr}/^{86}\text{Sr}$). Caminite is known from mineral assemblages with anhydrite and forms in hydrothermal recharge zones only under specific conditions such as high fluid temperatures and in altered oceanic crust, which are conditions generally met at the TR. We hypothesize that caminite was formed during hydrothermal activity and is now dissolving during the waning state of the hydrothermal system, so that caminite mineralization is shifted out of its stability zone. Ongoing fluid circulation through the basement is transporting the geochemical signal via slow advection towards the seafloor.

Plain Language Summary

Hydrothermal vents are a common phenomenon in oceanic spreading centers worldwide. During Meteor cruise 141/1 we sampled sediments and extracted pore fluids to find the first indications for hydrothermal activity in the Terceira Rift. The results indicate that a hydrothermal vent close to a major volcanic cone formed in the past and seems to be in a waning state at present. Sampled fluids are enriched in total alkalinity, Mg and SO₄. We found that the most straightforward explanation for this unusual finding is the dissolution of the hydrothermally formed mineral caminite, a magnesium-sulfate-hydroxide-hydrate. Caminite is a rare mineral, but suggested to be abundant under specific conditions in hydrothermal recharge zones. We propose that caminite formed in the Terceira Rift is now dissolving as temperatures decline, and fluids enriched in Mg and SO₄ are transported along deep-rooted faults to the seafloor.

IV.1 Introduction

Hydrothermal vents are common phenomena in slow to fast spreading centers worldwide (Beaulieu et al., 2013). Numerous authors provide a wealth of data on mineral assemblages and fluid chemistry of hydrothermal systems and their recharge zones (e.g. Alt, 1995; Teagle et al., 1998). Hydrothermal fluid circulation is a driver for cooling of the earth's crust, but also plays a major role in geochemical fluxes (Elderfield and Schultz, 1996). Generally, high-temperature reactions are the reason that fluids become depleted in Mg and SO₄ while Ca and fluid-mobile elements like Li are enriched. Mg is quantitatively removed from fluids by the formation of Mg-rich smectite such as saponite (Alt and Honnorez, 1984). SO₄ in hydrothermal systems can undergo various reactions. At temperatures above 150°C, SO₄ is typically removed by the precipitation of anhydrite (Alt et al., 1986; Teagle et al., 1998). However, SO₄ can also be reduced and precipitate as sulfide mineral (Alt, 1995). Ca is leached from the basement during albitization of plagioclase (Alt et al., 1986; Humphris and Thompson, 1978). Levels of enrichment can vary, but concentrations of Ca in fluids can reach up to 80 mM (e.g. Butterfield et al., 1994). There are few studies focusing on mineral dissolution after cooling of hydrothermal fluid circulation (e.g. Gieskes et al., 2002; Gruen et al., 2014), leading to substantial changes in fluid compositions (e.g. enrichment in SO₄ and Ca due to anhydrite dissolutions, brine formation due to leaching of hydrothermally formed salts in the subsurface).

The Terceira Rift (TR) is a ~ 500 km WNW- ESE striking rift in the Central North Atlantic Ocean, marking the plate boundary between Nubia and Eurasia. The TR has been described as a hyper slow spreading center with a spreading rate of 4 mm a⁻¹ (Vogt and Jung, 2004). Cutting through the Azores Plateau, the TR comprises four basins and passes through three volcanic islands of the Azores Archipelago (Fig. IV.1). Albeit ongoing magmatic activity in this region, only nine onshore hydrothermal springs (Couto et al., 2015), and one offshore submarine vent, located at the D. João de Castro seamount (Fig. IV.1), have been reported to date (Fig. IV.1; Cardigos et al., 2005). However, during a previous Meteor expedition (M 128) in 2016 no signs of hydrothermal activity was detected at this location (Beier, 2016). Weiß et al. (2015) reported on 252 volcanic cones and sills in the eastern TR and the flanks of São Miguel, which possibly could host hydrothermal systems. In the southern Hirondelle Basin major volcanic cones are connected to listric faults along the rift axis of the TR (Fig. IV.1C), providing a potential pathway for the ascent of hydrothermal fluids to the seafloor. One of the major cones shows no sediment cover in the backscatter data

(Weiß et al., 2015), which can be regarded as sign for recent magmatic activity. This volcanic cone provides presumably good preconditions to host a hydrothermal system. During R/V Meteor cruise M141/1 in September 2017 we sampled pore fluids by gravity coring in the vicinity of the elongated volcanic cone to detect potential signs of ongoing hydrothermal activity in the TR.

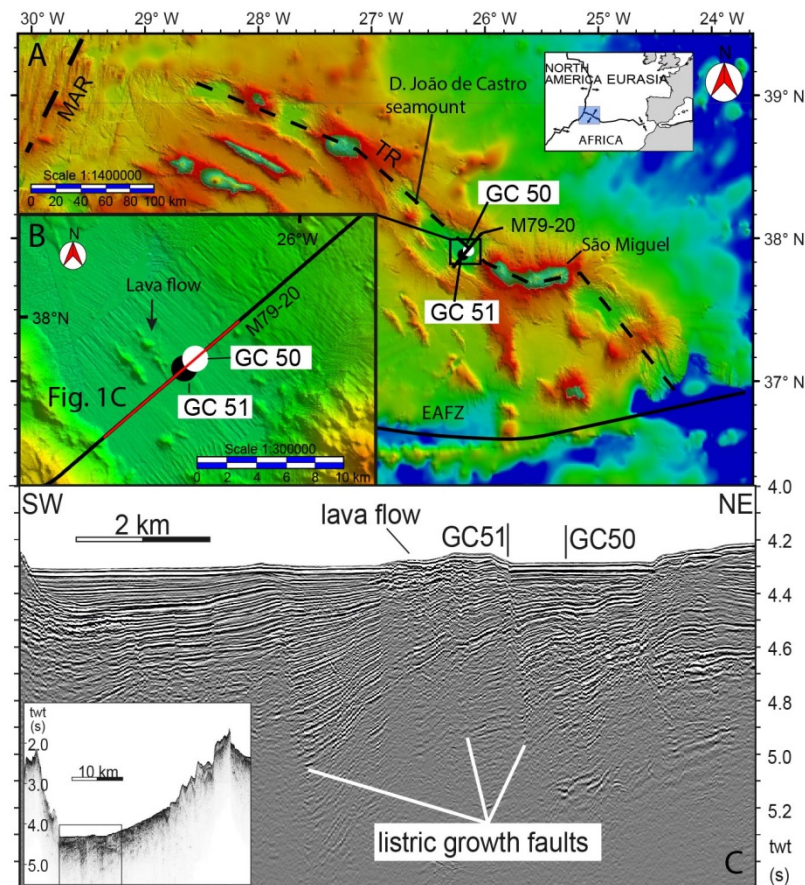


Figure IV.1. Overview Map A: regional overview map modified from Weiß et al. (2015); TR: Terceira Rift; MAR: Mid-Atlantic Ridge; EAFZ: East Azores fracture zone; B: detailed bathymetry map of core locations close to volcanic cone in the TR; C: Multi-channel seismic profile M79-20 crossing TR

IV.2 Materials and Methods

IV.2.1 Pore fluid and sediment sampling

Two gravity cores (GCs) were retrieved during the cruise at 2800 m water depth. GC51 was taken on the fault close to the volcanic cone whereas GC50 was taken as a regional reference core (Fig. IV.1B and IV.1C). Both GCs had a length of 5.75 m and were equipped with a plastic liner. Right after retrieval on deck, the plastic liner was cut into 1 m long segments and head space samples for hydrocarbon gas analyses were taken. The sampling

interval was between 5 and 20 cm. Sediment samples were squeezed in a cold room with an argon gas squeezer. On average, squeezing took about 10 minutes. Gas pressure was usually up to 5 bar. The pore fluid was filtered through 0.2 μm cellulose Whatmann filters.

IV.2.2 Pore fluid analyses

On board analyses for total alkalinity (TA) were carried out using a METROHM titration unit 876 Dosimat plus. TA was determined by titration with 0.02 N HCl using a methyl red indicator. The solution was bubbled with argon to remove CO_2 gas released during the titration. On board analyses for NH_4 were carried out using a Hitachi U2800A spectrophotometer applying a calibration curve with 8 standards covering the concentration range between 0 and 332.62 μM . In our shore-based laboratories at GEOMAR Helmholtz Center for Ocean Research, Kiel, cation concentrations (B, Ba, Ca, K, Li, Mg, Na, Si, Sr) were determined using the Inductively Coupled Plasma Optical Emission Spectrometry (ICP-OES, JY 170 Ultrace, Jobin Yvon). Anion concentrations (Cl, Br, SO_4) were analyzed using the Ion Chromatography (761 IC-Compact, Methrom). The IAPSO seawater standard was used to check the reproducibility and accuracy of the ICP-OES and IC chemical analyses (Gieskes et al., 1991). A detailed description of all standard methods used at GEOMAR can be found at <https://www.geomar.de/en/research/fb2/fb2-mg/benthic-biogeochemistry/mg-analytik/>.

IV.2.3. Solid phase analyses

Sediment samples from both cores were taken to determine their porosity and water content and for chemical bulk analyses of sediments and petrological description. For the chemical bulk analyses, sediments were dried at 65°C for 24 hours and homogenized. 100 mg of each sample was filled into a Savillex vessel and treated with 2 cm^3 HF, 2 cm^3 HNO_3 and 3 cm^3 HClO_4 at 185°C for 8 hours. Another 1 cm^3 of HNO_3 was added to smoke off the acid. The full method is available at: <https://www.geomar.de/en/research/fb2/fb2-mg/benthic-biogeochemistry/mg-analytik/acid-digestion/> (accessed January 2019 and description in Scholz et al., 2016). After treatment with acids, sediment samples were measured by inductively coupled plasma optical emission spectroscopy (ICP-OES) at GEOMAR, for concentrations of Al, Ca, Fe, K, Mg, Na, and Sr.

IV.2.4 Smear slides

Modal compositional data were obtained by counting at least 400 points in each of the 13 selected smear slides with a modified Gazzi–Dickinson method based on Decker and

Helmold (1985) and von Eynatten and Gaupp (1999) using a micro-step point-counting system and the Petroglide software without distinguishing into grain size fractions. The amount of 400 points was selected to derive a statistically significant estimation (e.g. Van der Plas and Tobi, 1965) of respective volume percentages of the components in the sediments. We distinguish between 13 juvenile and non-juvenile components. On the basis of common features four characteristic groups (total glass, total lithics, microfossils, and clay) were defined. Volume percentages of components or modal groups given in the text are normalized to 100 %. Percentage raw data and calculated volume percentages of modal groups are listed in Appendix C. Minerals like pyroxene, feldspar, amphibole, different types of pyroclasts, as well as sedimentary and volcanic lithics have not been subdivided in different species. Biogenic material has been subdivided into the main components (nannofossils, foraminifers) and minor abundances have been summarized in “biogenic rest”. The reproducibility (2 times counting) was tested for two different samples and is better than 4 % RSD regarding the modal groups. A detailed description can be found in the appendix C.

IV.2.5 Si Isotopes

Pore fluid samples were prepared for Si isotope measurements following the purification method of (Georg et al., 2006). The samples were loaded onto 1 ml pre-cleaned cation-exchange resin (Biorad AG50 W-X8) and eluted with 2 ml Milli-Q water. Si isotopes were measured on the NuPlasma high-resolution Multicollector-Inductively Coupled Plasma Mass Spectrometer (HR MC-ICPMS) in medium resolution mode using the Cetac Aridus II desolvator at GEOMAR Helmholtz Centre for Ocean Research Kiel. The Si concentration after sample purification equaled $\sim 22 \mu\text{M}$, yielding Si recoveries of $\geq 99\%$ and a procedural blank below detection limit. The measurements were executed using the standard-sample bracketing method to account for mass bias drifts of the instrument (Albarède et al., 2004). Si isotopes are given in the $\delta^{30}\text{Si}$ notation, which represents the deviation of the sample $^{30}\text{Si}/^{28}\text{Si}$ from that of the international Si standard NBS28. Long-term $\delta^{30}\text{Si}$ values of the reference materials Big Batch ($-10.6 \pm 0.2 \text{ ‰}$; 2SD; $n= 49$), IRMM018 ($-1.5 \pm 0.2 \text{ ‰}$; 2SD; $n= 48$), and Diatomite ($+1.3 \pm 0.2 \text{ ‰}$; 2SD; $n= 44$) agree well with published $\delta^{30}\text{Si}$ values in the literature (e.g. Reynolds et al., 2007). Additionally, an in-house pore fluid matrix standard has been measured, which yielded an average $\delta^{30}\text{Si}$ value of $+1.3 \pm 0.2 \text{ ‰}$ (2SD; $n= 17$). All samples were measured 2-3 times on different days and the resulting $\delta^{30}\text{Si}$ values have uncertainties between 0.1 and 0.2 ‰ (2SD).

IV.2.6 Sulfur Isotopes

Pore fluids were filtered (0.2 μm pore size filter) and acidified (25 % HCl) to a pH below 2. Subsequently, BaCl_2 solution (8.5 %) was added to precipitate barium sulfate at 80°C. The BaSO_4 precipitate was obtained via filtration using a cellulose nitrate filter (0.45 μm pore size). For $\delta^{34}\text{S}$ measurement 0.4mg barium sulfate mixed with 0.4 to 0.8mg V_2O_5 (catalyst) was placed into tin capsules. The $\delta^{34}\text{S}$ values were determined using an EA-IRMS (Thermo Scientific Delta V advantage coupled with a Flash-EA-IsoLink-CN Elemental Analyzer) at the Institute of Geology, Westfälische Wilhelms-Universität of Münster, and are reported in the standard delta notation as per mil difference to the Vienna-Canyon Diablo Troilite (V-CDT) standards. Analytical performance was monitored using international reference materials IAEA S-1, S-2, S-3 and NBS 127 with an external reproducibility better than 0.6 ‰ (2SD). For $\delta^{18}\text{O}_{\text{SO}_4}$ analysis 0.2 mg barium sulfate was placed in a silver capsule and $\delta^{18}\text{O}_{\text{SO}_4}$ was determined with a TC/EA-IRMS (Thermo Scientific Delta V plus connected with a high-temperature pyrolysis unit). The $\delta^{18}\text{O}_{\text{SO}_4}$ values are reported as per mil difference to the V-SMOW standard. Measurement of replicate samples and reference materials (IAEA-SO-5, -SO-6 and NBS 127) yielded an external reproducibility better than 1.0 ‰ (2SD).

IV.2.7. Sr Isotopes

Sr isotope ratios ($^{87}\text{Sr}/^{86}\text{Sr}$) were measured by thermal ionization mass spectrometry (TIMS, TRITON, ThermoFisher Scientific) at the GEOMAR on aliquots of the original ICP-OES pore water samples (described above). According to the prior element concentration analyses (ICP-OES) individual sample amounts equivalent to approx. 1500 ng Sr (usually in the range of tens to hundreds of μl pore water) were dried down in 2 ml of a 1 plus 2 mixture of 30 % H_2O_2 (supra pure) and 8 N HNO_3 (double distilled from per analyses quality). The separation of Sr followed a highly selective one step ion exchange chromatography using SrSpec resin (Eichrom) at whole procedure blanks of max. 60 pg. Before loading 100 to 200 ng Sr mixed with TaCl_5 activator on Re single filaments for TIMS measurements the Sr eluate was dried down in the $\text{H}_2\text{O}_2/\text{HNO}_3$ mixture as described above. Repeated analyses of the standard NIST SRM 987 were used for performance monitoring and normalization of the measured $^{87}\text{Sr}/^{86}\text{Sr}$ ratios applying a standard value of 0.710248 and reaching a reproducibility of ± 0.000010 (2SD, n=10) throughout the study. The latter level of precision is representative for the individual sample results (see uncertainties given in Table IV.3). Furthermore, the IAPSO seawater standard a $^{87}\text{Sr}/^{86}\text{Sr}$ ratio was determined on 0.709178 at ± 0.000010 (2SD, n=4).

IV.2.8. Ca Isotopes

Ca isotope measurements were performed on aliquots of the original pore water samples used for Sr isotope and element geochemistry ICP-OES analyses, with the same pretreatment as described for Sr purification. Calcium yields were >95 % suggesting that Ca isotopes are not measurably fractionated by chemical purification (Morgan et al., 2011). Prior to Ca isotope measurements samples were purified to remove matrix and interfering elements. We used a fully automated chromatographic purification system (prepFAST MC, ESI, Omaha, Nebraska, USA) following the method of Romaniello et al. (2015). Calcium isotope measurements were performed on a MC-ICPMS (Thermo Scientific Neptune, Thermo Fisher Scientific, Bremen, Germany) at the mass spectrometer facilities of GEOMAR. The mass spectrometer was set up to measure m/z of 42, 43, 43.5 and 44 simultaneously. In order to suppress interfering Ca- and Ar-hydrides (e.g. $^{40}\text{Ar}^1\text{H}_2$ on ^{42}Ca) an APEX IR (ESI, Omaha, Nebraska, USA) sample introduction system was used. All measurements were performed in medium resolution (MR, $m/\Delta m \sim 4,000$) on the low mass side of the peaks (cf. Wieser et al., 2004). Instrumental fractionation (mass bias) was corrected by applying the standard-sample-bracketing (SSB) approach. Interference correction for remaining sample Sr was done following the method of Morgan et al. (2011). Ca isotopes are given in the $\delta^{44/42}\text{Ca}$ notation, which represents the deviation of the sample $^{44}\text{Ca}/^{42}\text{Ca}$ from that of the international Ca standard NIST SRM 915a in per mil (‰). Long-term $\delta^{44/42}\text{Ca}$ of the reference materials NIST SRM 915b (0.35 ± 0.11 ‰, 2SD, $n=13$), NIST SRM 1486 (-0.50 ± 0.05 ‰, 2SD, $n=131$) and IAPSO (0.89 ± 0.06 ‰, 2SD, $n=128$) agree well with the literature values. A procedural blank for the Ca isotope work was determined and found to contribute less than 1% of the processed Ca.

IV.2.9 Mg Isotopes

Mg was separated from matrix elements by cation chromatography using DOWEX AG 50W-X12 in polypropylene columns. Mg was eluted using HNO_3 (2 N). Splits (1 mL) before and after the Mg elution peak were screened for Mg as indicator for quantitative ion separation. Mg isotope ratios were analyzed on a Neptune Plus MC-ICP-MS at Bundesanstalt für Materialforschung, Berlin. Samples and standards were introduced into a SIS spraychamber using a PFA microflow nebulizer with an uptake rate of 165 $\mu\text{L}/\text{min}$. Measurements were done in medium resolution mode using a normal sample cone and a X-skimmer cone. Procedural blanks are typically < 7 ng Mg, of which < 2 ng derived from the column procedure. Measured Mg isotope ratios were normalized to the standard ERM-AE

144 (Vogl et al., 2016) to compensate for mass bias drift (i.e. SSB). Samples and standard were diluted in HNO₃ (0.32 M) to $\approx 0.75 \mu\text{g/mL Mg}$, where matching was better than 12 %. Isotope ratios are reported in the δ -notation, i.e. as the deviation of a measured isotope intensity ratio (I) with the high mass isotopes $y=^{25}\text{Mg}$ or $z=^{26}\text{Mg}$ over the low mass-isotope ^{24}Mg of a sample (smp) from that of a standard (std):

$$\delta Mg_{std}^{y,z/24} = \frac{\left(\frac{I^{(y,z)Mg}}{I^{(24)Mg}}\right)_{smp} - \left(\frac{I^{(y,z)Mg}}{I^{(24)Mg}}\right)_{std}}{\left(\frac{I^{(y,z)Mg}}{I^{(24)Mg}}\right)_{std}} \quad (\text{IV.1})$$

δ -values (abbreviated as $\delta^{25}\text{Mg}$ and $\delta^{26}\text{Mg}$) were converted from the ERM-AE144 reference frame into the DSM3 reference frame using equation (Vogl and Pritzkow, 2010) for δ -values obtained from the above equation in their basic form (no ‰, ppm or else). When δ -values in ‰ are to be used, they have to be divided by 1000 before entering into the following equation.

$$\delta^{y,z/x}E(spl)_{std B} = \delta^{y,z/x}E(spl)_{std A} - \delta^{y/z}E(std B)_{std A} \left(\delta^{y/z}E(spl)_{std A} \cdot \delta^{y/z}E(std B)_{std A} \right) \quad (\text{IV.2})$$

As quality control standards we have analyzed NASS-6 (North Atlantic Seawater, NRC Canada) and the reference material ERM-AE145. NASS-6 yields $\delta^{25}\text{Mg}_{\text{DSM3}} = -0.37 \pm 0.04 \text{ ‰}$ and $\delta^{26}\text{Mg}_{\text{DSM3}} = -0.74 \pm 0.06 \text{ ‰}$ (2 SD, n= 4), identical within 2 SD to the published values of NASS-5 by Wombacher et al. (2009) with $\delta^{25}\text{Mg}_{\text{DSM3}} = -0.43 \pm 0.07 \text{ ‰}$ (2 SD, n= 8) and $\delta^{26}\text{Mg}_{\text{DSM3}} = -0.84 \pm 0.16 \text{ ‰}$ (2 SD, n= 4). Our measurements of ERM-AE145 yield $\delta^{25}\text{Mg}_{\text{DSM3}} = -2.30 \pm 0.05 \text{ ‰}$ and $\delta^{26}\text{Mg}_{\text{DSM3}} = -4.58 \pm 0.08 \text{ ‰}$ (2 SD, n= 3), identical within 2 SD with published values in Vogl et al. (2016) with $\delta^{25}\text{Mg}_{\text{DSM3}} = -2.30 \text{ ‰}$ and $\delta^{26}\text{Mg}_{\text{DSM3}} = -4.61 \text{ ‰}$. The uncertainty of δ -values for the entire dissolution, separation and measurement procedure is estimated to $<0.1 \text{ ‰}$ (2 SD).

IV.2.10 Head Space gas analyses

Headspace gas composition of 20 ml glass vials containing 3 cm³ of sampled sediment and additional 6 ml NaCl-solution were prepared according to Sommer et al. (2009). The vials were stored upside down at room temperature until measurement by using gas chromatography at GEOMAR. 100 μl of headspace gas was injected into a Shimadzu gas

chromatograph (GC-2014), equipped with flame ionization detector and thermal conductivity detector (carrier gas: He 5.0; HayeSep™ Q 80/100 column, column length: 2 m; column diameter: 1/8”). The detection limit for CH₄ and CO₂ were 0.1 ppmV and 100 ppmV, respectively. Precision was about 4 ‰ (2SD).

Porewater concentrations of dissolved methane (mmol per liter porewater) were calculated by considering measured sediment porosity and molar volumes at laboratory pressure and temperature. CO₂ values were used to determine pH values using the co2sys.xls program by Pelletier et al. (2005).

IV.2.11 Endmember calculations

Endmember (EM) calculations were performed for Mg, Ca, SO₄ and Sr. assuming binary mixing of seawater and the theoretical fluid EM. To calculate fluid EM we used element ratios vs elements for ⁸⁷Sr/⁸⁶Sr vs. Sr; Mg/Sr vs. Mg; Mg/Ca; Ca and Mg/SO₄ vs. SO₄. Seawater values were used as: ⁸⁷Sr/⁸⁶Sr = 0.709176; Sr = 90 μM, SO₄ = 27.8 mM; Ca = 10 mM and Mg = 53.2 mM. For the fluid EM, a fixed value is required, which is typically Mg = 0 for hydrothermal fluids. Since this is not possible in this case we approximate EM concentrations by using a fixed ⁸⁷Sr/⁸⁶Sr ratio (see details in section IV.4.6). For each element ratio vs. element concentration we calculated a mixing line using following equation (here shown for the example ⁸⁷Sr/⁸⁶Sr vs. Sr):

$${}^{87}\text{Sr}_{mix} = f_b[{}^{87}\text{Sr}]_b + (1 - f_b)[{}^{87}\text{Sr}]_a \quad (\text{IV.3})$$

$${}^{86}\text{Sr}_{mix} = f_b[{}^{86}\text{Sr}]_b + (1 - f_b)[{}^{86}\text{Sr}]_a \quad (\text{IV.4})$$

Taking ratios:

$$\frac{{}^{87}\text{Sr}}{{}^{86}\text{Sr}_{mix}} = \frac{f_b[{}^{87}\text{Sr}]_b + (1 - f_b)[{}^{87}\text{Sr}]_a}{f_b[{}^{86}\text{Sr}]_b + (1 - f_b)[{}^{86}\text{Sr}]_a} \quad (\text{IV.5})$$

Substituting $[{}^{87}\text{Sr}] = {}^{87}\text{Sr}/{}^{86}\text{Sr} [{}^{86}\text{Sr}]$

$$\frac{{}^{87}\text{Sr}}{{}^{86}\text{Sr}_{mix}} = \frac{f_b[{}^{86}\text{Sr}]_b \frac{{}^{87}\text{Sr}}{{}^{86}\text{Sr}}_b + (1 - f_b)[{}^{86}\text{Sr}]_a \frac{{}^{87}\text{Sr}}{{}^{86}\text{Sr}}_a}{f_b[{}^{86}\text{Sr}]_b + (1 - f_b)[{}^{86}\text{Sr}]_a} \quad (\text{IV.6})$$

[Sr] instead of [⁸⁶Sr] can be used as weighting factors, hence

$$\frac{{}^{87}\text{Sr}}{{}^{86}\text{Sr}}_{mix} = \frac{f_b[{}^{87}\text{Sr}]_b \frac{{}^{87}\text{Sr}}{{}^{86}\text{Sr}}_b + (1-f_b)[{}^{87}\text{Sr}]_a \frac{{}^{87}\text{Sr}}{{}^{86}\text{Sr}}_a}{f_b[{}^{87}\text{Sr}]_b + (1-f_b)[{}^{87}\text{Sr}]_a} \quad (\text{IV.7})$$

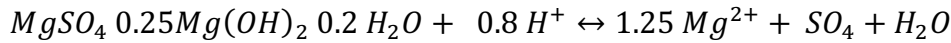
A comprehensive list for all used element ratios with all data can be found in the Appendix C.

IV.2.12 Thermodynamic model

The saturation state (SI) of caminite was calculated by comparing the ion activity product (IAP) of the solubility reaction to the corresponding thermodynamic equilibrium constant (K):

$$SI = \log\left(\frac{IAP}{K}\right). \quad (\text{IV.8})$$

The following stoichiometry was adopted for the dissolution reaction (Janecky and Seyfried, 1983):



So that the equilibrium constant is defined as

$$K_{caminite} = \frac{a_{Mg}^{1.25} a_{SO_4}}{(10^{-pH})^{0.8} a_{H_2O}} \quad (\text{IV.9})$$

where a represents the species activities.

To test the evolution of the saturation index over a broad temperature and pressure range, three different thermodynamic equilibrium constants (valid for a SO_4/Mg ratio of 0.625) were chosen from the work by Janecky and Seyfried (1983). In the lower temperature region $K_{caminite}$ equals 5.3 and is valid for 25°C and 1 bar. For data points near 200°C $K_{caminite}$ is assumed to be -1.98 and is valid for 200°C and 500 bar and the SI for 300°C uses the value -5.59 for the equilibrium constant and is valid for 300°C and 500 bar.

Species activities were calculated based on the molal concentration (m) and the activity coefficient (γ):

$$a = \gamma m \quad (\text{IV.10})$$

The activity coefficients and the activity of water were computed based on the Pitzer model as described in and originally derived by Pitzer and Mayorga (1973). Interactions among the

major sea ions were considered including Na, Mg, Ca, K, Cl and SO₄ and their concentrations were set either to the bottom water values or the extrapolated endmember values (Appendix C). Respective Pitzer parameters were derived from internally consistent collections (Pabalan and Pitzer (1987) and Greenberg and Moller (1989)), which incorporate the effects of ion pairing into their parameterization. It should be noted that the temperature range for the Pitzer data applied in the calculation of the species activities in most cases does not exceed 200°C. Instead of extrapolating the Pitzer parameters outside the stated temperature range, we use the parameterization of the upper temperature limit. For comparison, caminite SI is calculated for a range of pH values (7, 7.5 and 8). Also, while the equilibrium constants for elevated temperatures are valid only for 500 bar, we have also included the SI values that were calculated with activities for 1 bar to allow for a rough estimate of the pressure effect on the SI.

IV.2.13 Transport model

A simple 1D transport model including diffusion and advection was applied using Mathematica 11.3 (Wolfram Research, 2018). The model was solved for the solute species Mg, Ca, TA, and SO₄. The general differential equation reads as follows:

$$\frac{\partial \phi \cdot c}{\partial t} = \frac{\partial(\phi \cdot D_s \cdot \frac{\partial c}{\partial x})}{\partial x} - \frac{\partial(\phi \cdot v \cdot c)}{\partial x} \quad (\text{IV.11})$$

Where t is the time (yr), x is the depth (cm), ϕ - porosity (unitless), C - concentration of solutes (mmol dm⁻³), D_s - diffusion coefficient in the sediments (cm² yr⁻¹) corrected for tortuosity after (Boudreau, 1997) and v the fluid velocity (cm yr⁻¹). The model did not include any reactions. Initial porosity was set to 0.8 and porosity after compaction was set to 0.6 to fit the measured profile. Boundary conditions were defined for the sediment surface (0 cm) with ambient seawater concentrations (Mg = 54 mM, Ca = 10.2 mM, SO₄= 28.7 mM and TA = 2.7 meq/L) and for 300 cm depth (Mg = 63 mM, Ca = 11.5 mM, SO₄= 33 mM and TA = 11 meq/L; note that the lower boundary conditions are not equal to the calculated EM). The model was run into steady state. The upward flow velocity was determined by fitting the model to the measured pore water data.

IV.2.14 Seismic data

The reflection seismic data (Fig. IV.1C) have been collected during RV Meteor expedition M79/2 (Hübscher, 2012). Four so-called GI-Guns created the seismic signal and a

144-channel, 600 m-long seismic streamer, with a channel spacing of 4.2 m, recorded the data. Processing included band pass-filtering, energy balancing, NMO-correction, stacking, time-migration and fx-deconvolution. For an overview of the marine seismic method, see Hübscher and Gohl (2014).

IV.3 Results

IV.3.1 Pore fluid composition and isotope data

Pore fluid depth profiles for TA, Mg, Ca, SO₄, Li, Sr are shown in Fig. IV.2 A- F and data are provided in Table IV.1 (GC50) and Table IV.2 (GC51). The reference core GC50 shows a slightly elevated TA with 3.84 meq/L at 133 cm below seafloor (bsf). Ca is slightly decreasing from 10.86 at 12 cm bsf to 9.72 mM at 118 cm bsf. Sr is depleted in with respect to ambient bottom water (91 μM), with a decrease to 86.73 μM at 133 cm bsf. Mg, SO₄ and Li do not show any deviations from seawater values. For GC51, TA increases downcore from seawater values of 2.35 meq/L to up to 8.33 meq/L at 142 cm bsf. Also Mg is increasing with depth to 59.46 mM at 122 cm bsf and SO₄ increases from 27.8 mM to 31.21 mM at 134 cm bsf Ca remains almost constant over depth, with a slight increase up to 10.99 mM at 142 cm bsf with respect to seawater (10.2 mM). Sr in GC51 increases up to 150 μM at 142 cm bsf. In addition to that Li is also increasing to 40 μM in GC51.

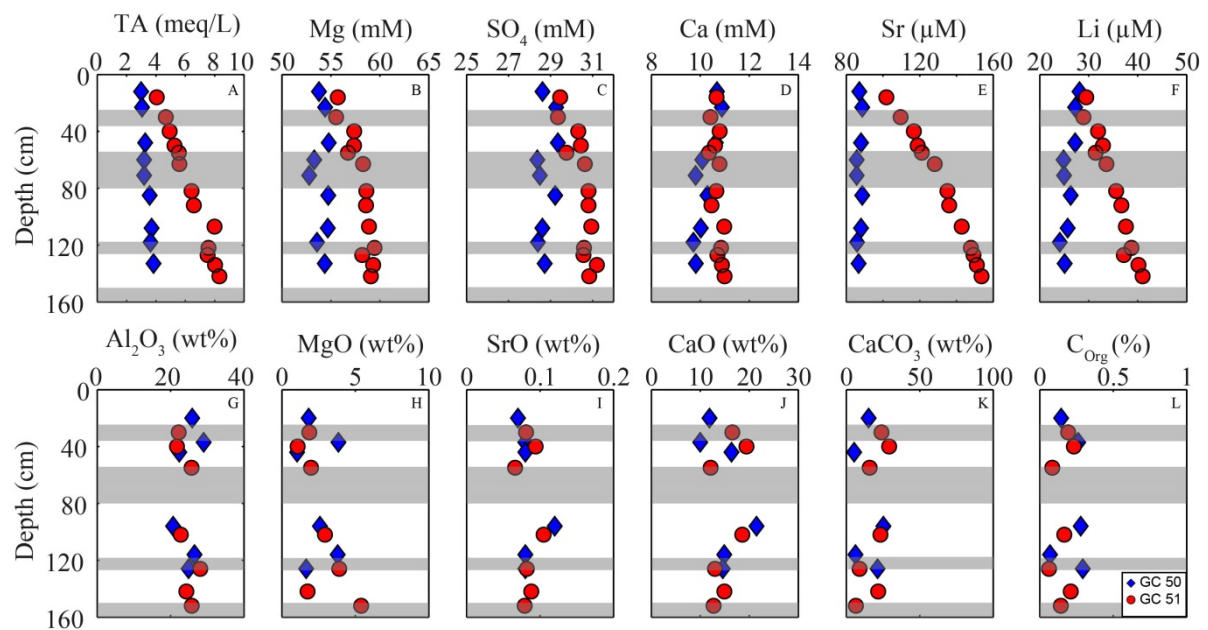


Figure IV.2 A – F: Pore water profiles for Total Alkalinity, Mg, SO₄, Ca, Sr and Li; **G – L:** depth profiles for solids of Al₂O₃, MgO, SrO, CaO, CaCO₃ and C_{Org}; Gray area indicate ash layers based on GC51

Table IV.1. Pore fluid data GC50; Core Location: 37°58.345'N; 26°5.046'W; gray areas indicate ash and tephra layers

Depth [cm]	NH4 [μM]	TA [meq/L]	B [mM]	Ca [mM]	Na [mM]	Mg [mM]	Sr [μM]	Si [mM]	Li [μM]	K [mM]	Cl [mM]	SO ₄ [mM]	Porosity [-]
12	11.40	2.99	0.46	10.68	483.40	53.78	87.17	0.19	28.14	10.69	559.73	28.62	
23	39.85	3.06	0.45	10.88	484.38	54.41	88.72	0.21	27.23	10.72	566.80	29.27	0.65
48	89.19	3.27	0.46	10.63	487.98	54.79	88.07	0.25	27.23	10.78	572.76	29.35	0.62
60	113.00	3.20	0.44	10.08	481.90	53.30	85.71	0.25	24.87	10.73	566.93	28.37	
71	123.80	3.20	0.44	9.81	480.01	52.79	85.71	0.25	24.97	10.74	568.66	28.49	
85	159.90	3.58	0.47	10.29	487.27	54.74	88.72	0.23	26.33	10.78	574.94	29.22	0.62
108	186.30	3.71	0.48	10.02	486.97	54.69	88.09	0.22	25.70	10.61	572.46	28.61	0.82
118	188.10	3.63	0.45	9.72	483.11	53.59	85.89	0.21	24.11	10.15	569.10	28.40	
133	194.10	3.84	0.49	9.82	484.83	54.38	86.73	0.22	25.09	10.49	572.76	28.72	0.64

Table IV.2. Pore fluid data GC51; Core Location: 37°58.049'N; 26°5.489'W; gray areas indicate ash and tephra layers

Depth [cm]	NH4 [μM]	TA [meq/L]	B [mM]	Ca [mM]	Na [mM]	Mg [mM]	Sr [μM]	Si [mM]	Li [μM]	K [mM]	Cl [mM]	SO ₄ [mM]	Porosity [-]
16	64.57	4.05	0.45	10.66	485.68	55.72	101.80	0.21	29.48	10.33	560.59	29.46	0.59
30	88.09	4.67	0.45	10.41	481.60	55.52	109.57	0.22	28.91	9.80	564.72	29.35	
40	114.50	4.94	0.47	10.79	490.37	57.39	116.86	0.25	31.94	10.50	571.75	30.32	0.61
50	140.10	5.27	0.48	10.60	488.25	57.37	118.92	0.26	32.89	10.40	571.82	30.45	0.61
55	144.50	5.57	0.47	10.36	486.04	56.73	121.14	0.24	31.42	9.86	567.28	29.76	
63	179.30	5.60	0.48	10.78	490.16	58.29	128.12	0.23	33.63	10.80	571.78	30.64	
82	221.00	6.42	0.50	10.65	491.83	58.64	135.08	0.26	35.61	10.15	571.47	30.81	0.62
92		6.58	0.48	10.46	489.73	58.59	136.02	0.22	36.69	10.32	575.87	30.81	0.60
107	324.00	7.99	0.52	10.98	490.31	58.90	142.84	0.35	37.61	10.07	573.06	30.94	0.66
122	290.30	7.58	0.52	10.85	492.54	59.46	147.86	0.24	38.73	10.14	561.68	30.59	0.62
127	268.50	7.52	0.51	10.70	488.66	58.19	149.34	0.23	37.16	9.62	567.62	30.57	
134	277.90	8.03	0.53	10.88	491.80	59.33	151.08	0.23	40.15	9.94	573.32	31.21	0.65
142	293.00	8.33	0.53	10.99	489.33	59.09	153.67	0.23	41.02	9.94	572.27	30.84	0.64
153*	6.94	3.00	0.42	10.54	483.01	53.66	89.93	0.17	26.68	9.82	560.76	28.76	
162*	40.13	3.99	0.46	10.84	485.85	55.68	100.65	0.20	29.71	10.45	564.75	29.70	0.59

Table IV.3 Isotope results for $^{87}\text{Sr}/^{86}\text{Sr}$, $\delta^{34}\text{S}$, $\delta^{18}\text{O}_{\text{SO}_4}$, $\delta^{26}\text{Mg}$, $\delta^{30}\text{Si}$, and $\delta^{44/42}\text{Ca}$ for GC50 and GC51.

Depth [cm]	$^{87}\text{Sr}/^{86}\text{Sr}$	2SD	n	$\delta^{34}\text{S}_{\text{SO}_4}$ [‰; V-CDT]	2SD	n	$\delta^{18}\text{O}_{\text{SO}_4}$ [‰; V-SMOW]	2SD	n	$\delta^{26/24}\text{Mg}$ [‰; DSM3]	2SD	n	$\delta^{30}\text{Si}$ [‰; NBS28]	2SD	n	$\delta^{44/42}\text{Ca}$ [‰; SRM915A]	2SD	n	
GC50																			
23	0.709061	0.000007	3	-	-	-	-	-	-	-0.80	0.06	3	1.63	0.15	2	0.88	0.07	4	
133	0.708817	0.000010	4	24.2	0.08	2	15.9	0.46	2	-0.75	0.04	3	1.41	0.23	2	0.86	0.08	4	
GC51																			
16	-	-	-	21.9	0.10	2	11.0	0.82	2	-	-	-	1.6	0.22	3	-	-	-	
50	0.708084	0.000013	4	23.0	0.02	2	14.0	0.97	2	-0.39	0.04	3	1.79	0.22	3	0.84	0.08	4	
82	0.707752	0.000010	4	-	-	-	-	-	-	-0.30	0.06	3	1.46	0.18	3	0.81	0.05	4	
134	-	-	-	24.7	0.05	2	17.5	0.80	2	-	-	-	-	-	-	-	-	-	
142	0.707428	0.000008	3	-	-	-	-	-	-	-0.18	0.05	3	1.22	0.08	2	0.77	0.05	4	

Isotope systematics of GC51 show a strong deviation from seawater for $^{87}\text{Sr}/^{86}\text{Sr}$ and $\delta^{26}\text{Mg}$ and only minor deviations for $\delta^{34}\text{S}$, $\delta^{44/42}\text{Ca}$ and $\delta^{30}\text{Si}$ (Fig. IV.4 and Table IV.3). $^{87}\text{Sr}/^{86}\text{Sr}$ shows a decreasing trend from 0.7091 (present day seawater) to 0.7074 at 142 cm bsf. $\delta^{26}\text{Mg}_{\text{GC51}}$ values of the sampled fluids show an increase in $\delta^{26}\text{Mg}$ from -0.81 ‰ (seawater) to -0.18 ‰ at 142 cm bsf. $\delta^{34}\text{S}_{\text{GC51}}$ increases with depth from 21.9 ‰ at 16 cm bsf to 24.7 ‰ at 134 cm bsf. $\delta^{44/42}\text{Ca}_{\text{GC51}}$ does decrease slightly from 0.84 ‰ at 50 cm bsf to 0.77 ‰ at 142 cm bsf. $\delta^{30}\text{Si}_{\text{GC51}}$ does on the other side show no deviation from seawater values with depth. In contrast to GC51 all isotopic ratios measured for GC50 do not show any or only minor ($^{87}\text{Sr}/^{86}\text{Sr}$ and $\delta^{34}\text{S}$) deviations from present day seawater values (Fig. IV.4 and Table IV.3).

IV.3.2 Solid phase

The sediments largely consist of nannofossil-rich mud to mud-rich nannofossil ooze with variable admixture of fresh volcanic, siliciclastic, and biogenic material. A detailed description of sediments and components can be found in the appendix C. Organic input to sediments is low resulting in an average amount $<0.3\%$ of C_{Org} . CaCO_3 proportion of the sediments is in average $\sim 20\%$. The main composition of the sediments is rather constant over depth and does not show pronounced differences between the two coring locations (Fig. IV.2 G – L). The Chemical Index of Alteration (CIA) (Nesbitt and Young, 1982) is used as a measure to determine the degree of weathering of the sediments. The CIA is calculated as: $\text{CIA} = \text{Al}_2\text{O}_3 / (\text{Al}_2\text{O}_3 + \text{CaO}^* + \text{Na}_2\text{O} + \text{K}_2\text{O}) \times 100$. CaO^* is the Ca bound to silicates, and is determined by subtracting Ca bound to carbonates ($\text{CaCO}_3 = 8.33 * \text{TIC}$) from total Ca. The average CIA for both cores is between 40 and 60 % (Appendix C).

IV.3.3 Head space gas

Head space gas analyses for CH_4 and CO_2 did not show any variations with depth (see Appendix C for data). CH_4 values stay at background values. The highest methane concentration was observed in GC50 at 166 cm bsf with $0.739\ \mu\text{M}$. In addition to that, also fCO_2 values remain at background values with slightly elevated values for GC51. fCO_2 values go up to 5599 ppm in GC51. The calculated pH values from fCO_2 and TA concentrations are for both cores about 7.5.

IV.4 Discussion

In the following, we will present a comprehensive analysis of potential processes that might explain the unusual geochemical pore fluid signature of GC51 with anomalously high TA, Mg and SO₄ concentrations.

IV.4.1 Near-surface diagenetic processes

Pore water profiles of enriched species display a slight exponential curvature within the uppermost ~50 cm (Fig. IV.2). Generally, such type of profiles can either be the result of continuous reactive processes, or be caused by fluid advection. Reactions typically include organic matter degradation, secondary redox reactions, weathering/alteration of rocks and mineral dissolution reactions. Our data suggests, that the reactive influence in the shallow sediments is only minor: The TR in the Central North Atlantic Ocean receives only minor input of organic matter reflected by very low concentrations of TOC (<0.3 wt.%). Moreover, the increase in TA that results from organic matter degradation should also have been observed in GC50 where the increase is almost negligible. The increase in TA, could also be explained by the anaerobic oxidation of methane (AOM) coupled to sulfate reduction. This would require a deep methane source but neither indications for sulfate reduction (SO₄ concentrations are elevated in GC51), nor methane enrichment were detected in GC51. We assume that some of the elevated TA in GC51 comes from minor organic matter degradation, but additional processes have to be considered. Weathering/alteration of rocks or mineral dissolution processes could on first sight explain the curvature in the increasing profiles in GC51. Weathering of the volcanoclastic sediments can have an effect on the fluid composition, as minerals like Mg-smectite and zeolites can be formed or elements can be released due to volcanic glass dissolution (Schacht et al., 2008). However, visual analyses of the surface sediments by smear slides did not reveal indications for altered volcanic compounds or any secondary Mg or SO₄ bearing minerals (e.g. being indicative for hydrothermal alteration). Furthermore, the sediments of the reference core GC50 are identical in composition and depth of stratigraphic layers compared to GC51 (Fig. IV.2 G – L). Intense weathering and formation of secondary minerals typically results in the loss of alkaline and alkaline earth metals, which is reflected in high values (>75 %) of the CIA. CIA values for both cores do not show any evidence for pronounced alteration processes and no depth-related trends.

IV.4.2 Indications for upward fluid flow

The lack of evidence for alteration processes in the near surface sediments suggests that the geochemical composition of the fluid is not the result of *in situ* processes, but instead seems to be derived from deeper sources. The application of a simple numerical fluid transport model was carried out to test if the shape of the profiles (Fig. IV.2 A-F) can be explained by an advective flux component. We tested two model scenarios (i) only diffusion and (ii) advection and diffusion (Fig. IV.3). Indeed, a reasonably good fit to the data could be obtained with a fluid velocity of 0.5 cm yr^{-1} , emphasizing the need to include the advection process in the profile interpretation. With shallow diagenetic processes being only of minor importance, the hypothesis that fluids are derived from a deeper source is supported.

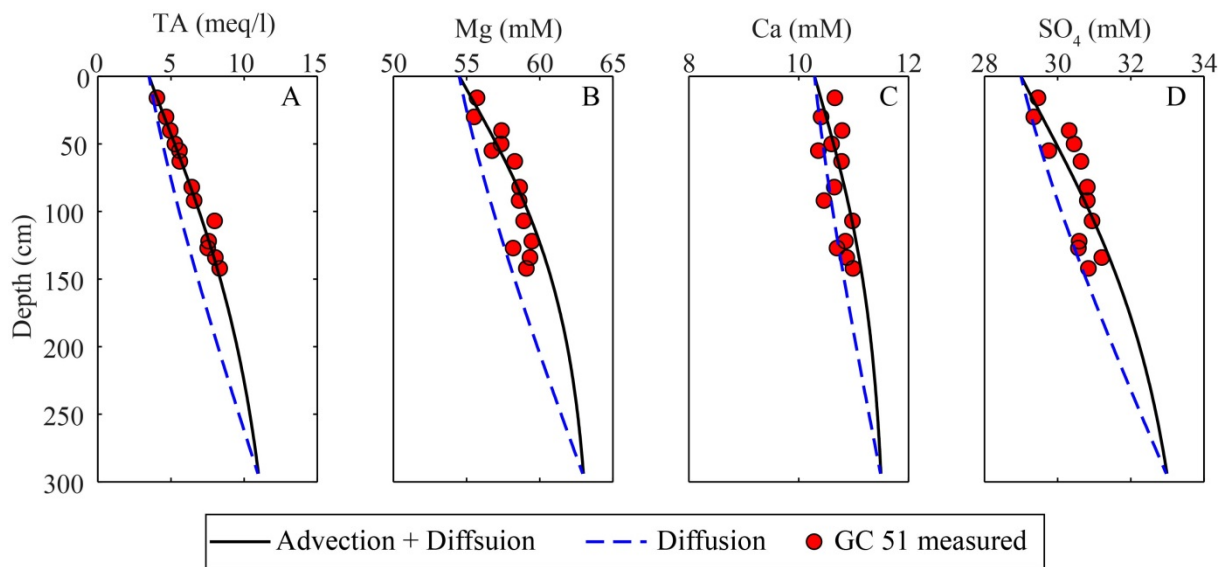


Figure IV.3 Transport model results for both scenarios: (i) diffusion (dashed line) and (ii) diffusion and advection (solid line) for A: TA; B: Mg; C: Ca and D: SO₄

IV.4.3 Hydrothermal signature

With respect to the location close to an active spreading center and recent magmatic activity in the area, we suspect that the observed pore water anomalies are related to hydrothermal activity. Many processes in hydrothermal systems do affect Mg and SO₄ concentrations of fluids. Below, we analyze potential processes that might cause such anomalies and discuss their likeliness.

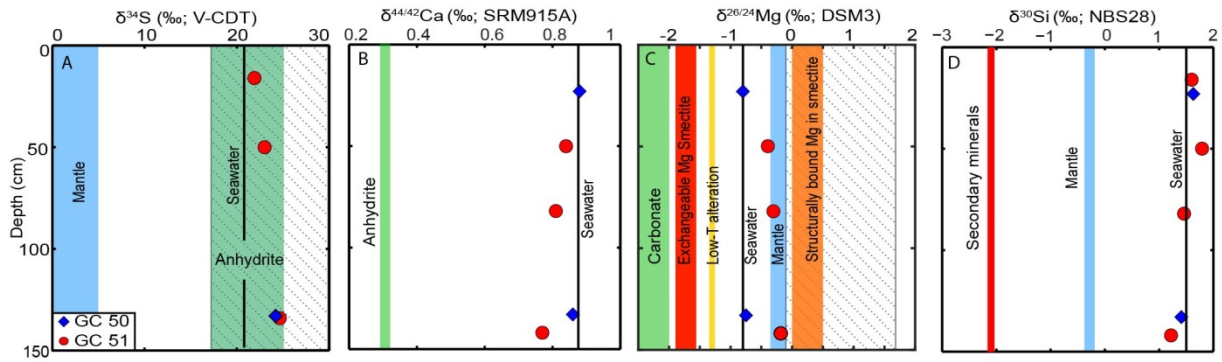


Figure IV.4 Depth profiles for isotopes and potential sources; the shaded area in A and B represent the estimated range of $\delta^{26}\text{Mg}$ and $\delta^{34}\text{S}$ -values of caminite. A: $\delta^{34}\text{S}_{\text{Seawater}} = 21 \text{ ‰}$; $\delta^{34}\text{S}_{\text{Evaporites}} = 19 - 25 \text{ ‰}$; $\delta^{34}\text{S}_{\text{Mantle}} = 0 - 5 \text{ ‰}$ (Alt, 1995); B: $\delta^{26}\text{Mg}_{\text{Seawater}} = 0.81 \text{ ‰}$, $\delta^{26}\text{Mg}_{\text{Carbonate}} < -2 \text{ ‰}$, mantle = $-0.4 - -0.2 \text{ ‰}$ (Teng, 2017); $\delta^{26}\text{Mg}_{\text{exchangeable of smectite}} = -1.5 \text{ ‰}$; $\delta^{26}\text{Mg}_{\text{structurally bound in smectite}} = 0 - 0.5 \text{ ‰}$ (Wimpenny et al., 2014); $\delta^{26}\text{Mg}_{\text{Low-T alteration fluids}} = -1.31 \text{ ‰}$ (Liu et al., 2017); C: $\delta^{30}\text{Si}_{\text{Seawater}} = +1.6 \text{ ‰}$, $\delta^{30}\text{Si}_{\text{Mantle}} = -0.3 \text{ ‰}$, $\delta^{30}\text{Si}_{\text{Secondary Mineral}} = -2.1 \text{ ‰}$; D: $\delta^{44/42}\text{Ca}_{\text{Seawater}} = 0.9 \text{ ‰}$, $\delta^{44/42}\text{Ca}_{\text{Anhydrite}} = 0.3 \text{ ‰}$, the shaded area in A and C indicates the presumed isotopic composition for caminite

IV.4.3.1 SO_2 enriched volatiles

Hydrothermal fluids enriched in Mg and SO_4 have been reported from other regions, e.g. the DESMOS caldera (Gamo et al., 1997; Seewald et al., 2015). In these case, the excess SO_4 concentrations were explained by the discharge of SO_2 -enriched magmatic volatiles and their subsequent disproportionation to SO_4 . Such highly acidic fluids can leach Mg-rich silicate minerals from the host rock, resulting in increased Mg concentrations (Gamo et al., 1997). Sulfur of magmatic origin can be distinguished from seawater sulfur and other sources by its $\delta^{34}\text{S}$ signature. Fluids sampled at the DESMOS caldera show much lower values compared to seawater and, hence, are typical for a mantle sulfur source ($\delta^{34}\text{S}_{\text{Mantle}} < 5 \text{ ‰}$; Seewald et al., 2015). In contrast, $\delta^{34}\text{S}_{\text{GC51}}$ values increase slightly and stay at levels above seawater (Fig. IV.4A). A mantle origin of SO_4 via disproportionation from SO_2 we can rule out.

IV.4.3.2 Anhydrite dissolution

One of the most abundant minerals formed in hydrothermal systems is anhydrite. Hydrothermal anhydrite formation is a major sink for SO_4 , resulting in the removal of SO_4 from fluids (Alt, 1995). The mineral phase forms at temperatures above 150°C , but is generally not present in old, altered oceanic crust as it dissolves at lower temperatures (Alt, 1995). Dissolution of anhydrite could therefore be a source for SO_4 to the pore fluids (Gieskes et al., 2002). $\delta^{34}\text{S}$ values of anhydrite are typically around or slightly above seawater (Alt, 1995), matching our observations in the fluids (Fig. IV.4A). In contrast, Ca concentrations are not significantly elevated in GC51, albeit the fact that anhydrite dissolution releases equal

amounts of Ca and SO₄ to the pore fluids. Moreover, an extensive dissolution of anhydrite should result in much stronger deviations of the $\delta^{44/42}\text{Ca}_{\text{GC51}} = 0.77\text{‰}$ from $\delta^{44/42}\text{Ca}_{\text{Seawater}} = 0.89\text{‰}$ (Fig. IV.4B). Anhydrite has a shift of 0.5‰ from seawater to lower values (Amini et al., 2008). Thus, an additional sink for Ca, e.g. calcium carbonate formation or ion exchange with clay minerals would be required or only a minor dissolution of anhydrite seems plausible here. Additionally dissolution of anhydrite could explain the elevated Sr concentrations. Sr is an abundant trace element in hydrothermally formed anhydrite (Teagle et al., 1998). However, anhydrite dissolution cannot explain the increased TA or Mg concentration.

IV.4.3.3 Mg-rich smectite

Mg-rich smectite, such as saponite, is the major sink for Mg in hydrothermal systems (Alt et al., 1986). In contrast to anhydrite, saponite is present in aged oceanic crust and is not dissolving during cooling of hydrothermal systems (Alt and Honnorez, 1984). Mg Smectite dissolution can be excluded as potential source for the Mg excess relative to seawater. Clay minerals do have a significant ion exchange capacity due to their large surface area. The main cations being exchanged are Mg, Ca, H, and Na (Wimpenny et al., 2014). Accordingly, smectite could be a potential sink for Ca and source for Mg. The overall $\delta^{26}\text{Mg}$ of Mg-smectites is above 0‰ (Fig. IV.4C, Teng, 2017). Most of Mg is bound to the clay mineral lattice and only absorbed Mg and Mg in the interlayers can be exchanged. The exchangeable Mg of smectite is typically around -1.5‰ $\delta^{26}\text{Mg}$ (Wimpenny et al., 2014) and therefore lower than seawater values. Consequently, ion exchange should result in a decrease of the $\delta^{26}\text{Mg}$ -value in the fluid relative to the $\delta^{26}\text{Mg}$ in seawater, which is opposite to the $\delta^{26}\text{Mg}$ values in GC51. In contrast, the dissolution of Mg-rich silicates by acidic fluids yields $\delta^{26}\text{Mg}$ -values between -0.15‰ and -0.25‰ (Teng, 2017), identical with the pore fluid $\delta^{26}\text{Mg}$ in GC51.

Silicon isotopes ($\delta^{30}\text{Si}$) can be used as an additional fluid tracer, as different reservoirs are characterized by distinct $\delta^{30}\text{Si}$ values. Mantle fluids have an average $\delta^{30}\text{Si}$ value of -0.3‰ (De La Rocha et al., 2000). Also secondary clay mineral dissolution would enrich the fluid phase in light ²⁸Si, as clays show on average low $\delta^{30}\text{Si}$ values of -2.1‰ (De La Rocha et al., 2000; Ziegler et al., 2005; Opfergelt et al., 2010). The $\delta^{30}\text{Si}$ values in GC51 range between +1.2‰ and +1.8‰ (Fig. IV.4D) and thus overlap within error of the Si isotope value of the deep Atlantic water at 2800 m water depth (average $\delta^{30}\text{Si}_{\text{Atlantic}} = +1.6\text{‰}$ (Brzezinski & Jones, 2015; De Souza et al., 2012) and the reference core GC50, which has an average $\delta^{30}\text{Si}$ value of +1.5‰ (see Table IV.3). Consequently, dissolution of secondary Si-rich minerals or mixing with mantle fluids can be excluded as well.

IV.4.3.4 Low temperature weathering of peridotite

Snow and Dick (1996) proposed that the weathering of peridotite at temperatures below 150°C results in the pervasive loss of Mg of the basement. Slow spreading ridges are the typical environments where peridotites get exposed to the seafloor surface. Ligi et al. (2013) proposed that the increase in number of slow spreading ridges in the past 80 Ma have contributed to a shift in the global Mg cycle as enhanced weathering of peridotites could have occurred. However, up to date no Mg-rich fluids have been found in slow spreading environments. The hyper slow spreading TR could be suitable for the conditions defined for high Mg vents by Ligi et al. (2013). The crustal thickness of the basaltic Azores Plateau is about 14 km (Escartin et al., 2001), and exposure of mantle peridotite is unlikely here. In addition to that, no description of exposed peridotites is available for the TR. Nevertheless, if a deep fluid circulation could reach peridotites, low temperature weathering of peridotites results in the formation of Mg-smectite, accompanied with a fractionation of Mg isotopes (Liu et al., 2017). According to the authors fluids enriched in Mg affected by low temperature weathering result in $\delta^{26}\text{Mg}$ values lower than seawater by -1.31 ‰ while $\delta^{26}\text{Mg}$ values in core GC51 are enriched with respect to seawater. Hence, we conclude that this process is not or at least not significantly affecting the fluid composition at GC51.

IV.4.4 Dissolution of Caminite

None of the processes described above can satisfactorily explain the geochemical pore fluid anomalies of high Mg, SO_4 and TA concentrations observed in GC51. All of the above discussed processes only impacts one of the three enriched species. A complex succession of these processes can also not satisfactorily explain the fluid geochemistry at GC51. We suggest therefore that we see here as of yet underestimated case where the dissolution of the hydrothermally formed mineral caminite may offer an explanation for the observed pore fluid deviations. Caminite is a magnesium-sulfate-hydroxide-hydrate ($\text{MgSO}_4 \cdot 0.25\text{Mg}(\text{OH})_2 \cdot 0.2\text{H}_2\text{O}$), which to date has been only found once in a natural environment. Haymon and Kastner (1986) reported caminite from a black smoker site on the East Pacific Rise 21°N, precipitating directly from heated seawater. Furthermore, this mineral has been synthesized under laboratory conditions (Janecky and Seyfried, 1983). Both studies indicate that high fluid temperatures of >240°C are needed to form caminite. Although caminite can be regarded as a rare mineral, Haymon and Kastner (1986) proposed that it could be an abundant mineral in hydrothermal recharge zones where high temperatures are present in the system while Mg-smectite formation is largely inhibited. The authors assumed that such a scenario is possible

in hydrothermal systems with little fresh basaltic glass present in the recharge zone. This implies that during a former hydrothermal alteration Mg-smectite already formed and the reactivity of the basement is lower compared to young oceanic basement. The basement of the Azores Plateau has undergone intensive alteration (Beier et al., 2019), hence, there is the possibility that smectite formation has occurred before and no fresh basaltic glass is present at this location in the basement. Moreover, an enrichment of Li in fluids is indicative for elevated fluid temperatures in the subsurface (e.g. Scholz et al., 2010). The Li concentrations in GC51 is slightly elevated compared to the reference core, we can therefore assume that high fluid temperatures are present in the subsurface in the TR.

Thus, the general conditions for the formation of caminite (as defined by Haymon and Kastner (1986) are likely to be met in the TR. It has also been shown, that caminite dissolves rapidly at temperatures $< 240^{\circ}\text{C}$ (Haymon and Kastner, 1986). Decreasing temperatures after hydrothermal activity could result in the dissolution of previously formed caminite increasing the Mg and SO_4 concentrations in the ambient fluids. This is also in line with the additional increased TA in GC51 compared to GC50 due to the release of $(\text{OH})^-$ through the dissolution of caminite.

According to Janecky and Seyfried (1983), caminite is present in two modifications with different SO_4/Mg ratios. The authors describe one modification with $\text{SO}_4/\text{Mg} = 0.625$ which is the more stable phase at temperatures above 300°C and pressures below 500 bars, and caminite with $\text{SO}_4/\text{Mg} = 0.7$, which is more stable at temperatures below 300°C and 500 bars. In addition the $\text{SO}_4/(\text{OH})^-$ ratio can vary between 1.25 and 2. Maximum concentrations of Mg and SO_4 in GC51 are above seawater levels by are 5.89 and 3.41 mM, respectively. To determine the excess TA at GC51, the maximum TA at GC50 was subtracted from the value at GC51, resulting in an excess concentration of 4.24. The resulting ratios for SO_4/Mg and $\text{SO}_4/(\text{OH})^-$ are 0.58 and 0.8, respectively. These ratios are very similar to the published ratios despite the fact that minor modification of fluids in the remaining sedimentary column (e.g. through microbial activity) are possible.

Unfortunately, all isotope systems discussed in the preceding sections cannot be used to further constrain the process of caminite dissolution, which is simply due to the fact that no isotopic analyses for caminite have been reported so far. Hence, the measured isotopic compositions of $\delta^{26}\text{Mg}$ and $\delta^{34}\text{S}$ in GC51 provide a first idea of how these isotope systems are affected during formation of caminite. Based on our findings, we expect a shift towards

positive $\delta^{34}\text{S}$ values, similar to anhydrite (Fig. IV.4A), and a fractionation towards positive ^{26}Mg values (Fig. IV.4C).

Caminite re-dissolution can explain the increase of Mg, SO_4 and TA in pore water of GC51, but elevated Sr concentrations remain a puzzling observation. In laboratory experiments caminite did not incorporate Sr into the mineral structure (Janecky and Seyfried, 1983). The absence of Sr in caminite thus indicates that the enrichment of Sr in pore fluids cannot be explained by caminite dissolution. Notably though, caminite is typically associated with anhydrite (Haymon and Kastner, 1986), that incorporates Sr and other divalent ions (Teagle et al., 1998). As discussed before, an accompanied minor dissolution of anhydrite could explain the Sr increase. Also a small increase in Sr from anhydrite dissolution would have a minor affect SO_4 and Ca concentrations, as they have different concentration levels in the pore fluid. Thus, the suggested fluid mixture is generated by different sources but in the same depth and transported to the seafloor. Concentrations of Sr, Mg, Ca, and SO_4 are coherent and Sr can therefore be used as a tracer for EM calculation.

IV.4.5 End member calculation

The fluids sampled in GC51 are a mixture of ambient pore water (seawater) and the deep fluid. EM calculations are used to determine maximum concentrations of the fluid source. For hydrothermal fluids this is in general performed using a 0 mM EM for Mg and calculate respective element enrichments or depletions accordingly (e.g. Douville et al., 2002). However, the high Mg concentrations complicate the problem and a workaround had to be found to constrain the unknown fluid endmember at depth. The concentrations of Sr, Mg, Ca and SO_4 are coherent as the fluid mixture (from caminite and to a lower extent anhydrite dissolution) is generated in the same region and transported to the seafloor. We chose to base our estimates on $^{87}\text{Sr}/^{86}\text{Sr}$ ratios. Sr isotopes and concentration ($1/\text{Sr}$) plot on a linear regression line. The minimum isotope ratio can be approached for $1/\text{Sr}$ approaching towards 0, resulting in an $^{87}\text{Sr}/^{86}\text{Sr}$ of 0.7049 for GC51 (Fig. IV.5C). Interestingly, this value, is in agreement with ratios of the oceanic basement in the TR (0.7035 to 0.7060; Beier et al., 2008; White et al., 1976). Sr isotope ratios in the west are lower and shifting to higher ratios to the east. The sample location of GC51 is located in the part of the TR where values for $^{87}\text{Sr}/^{86}\text{Sr}$ are around 0.705. Moreover the proposed EM value represents also Sr isotope ratios of hydrothermally formed anhydrite (Teagle et al., 1998). Assuming Sr release is caused by minor anhydrite dissolution as discussed before, this Sr release can also cause the Sr isotope deviation. Therefore we take $^{87}\text{Sr}/^{86}\text{Sr} = 0.7049$ as a fixed EM for the following EM

calculation of the other elements. The EM calculation was then performed as described in section IV.2.11 assuming a binary mixing of seawater and the EM. The best fit for $^{87}\text{Sr}/^{86}\text{Sr}$ vs. Sr could be obtained with a Sr concentration of 650 μM . On a mixing line between seawater ($^{87}\text{Sr}/^{86}\text{Sr} = 0.709176$; Sr = 91 μM) and fluid EM ($^{87}\text{Sr}/^{86}\text{Sr} = 0.7049$; Sr = 650 μM) the measured sample lies at 10 % EM fluid (Fig. IV.5C). Accordingly we used in a next step the Sr concentration as a fixed value and deduced the Mg concentration using the Sr/Mg ratio. The same approach was used to deduce EM Ca and SO_4 concentrations. The resulting EMs are: Mg = 85 mM, $\text{SO}_4 = 47$ mM, Sr = 650 μM , Ca 12 mM, and $^{87}\text{Sr}/^{86}\text{Sr} = 0.7049$ (Fig. IV.5). Nevertheless, this method is based on a number of assumptions (e.g. no modification of fluids in the sediment column), which cannot be further constrained, and hence, the EM calculation can only be regarded as a rough approximation.

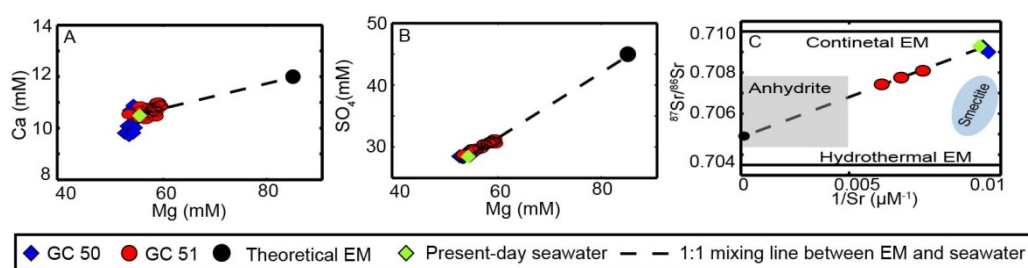


Figure IV.5 Binary mixing between present-day seawater (green diamond) and theoretical EM (black dots); dashed line: mixing line between seawater and EM; A: Ca vs. Mg; B SO_4 vs. Mg; C: $^{87}\text{Sr}/^{86}\text{Sr}$ vs. $1/\text{Sr}$, Anhydrite $^{87}\text{Sr}/^{86}\text{Sr} = 0.745 - 0.708$, $1/\text{Sr} < 0.005$ (Teagle et al., 1998); Smectite $^{87}\text{Sr}/^{86}\text{Sr} = 0.705 - 0.707$, $1/\text{Sr} = 0.01 - 0.025$ (Hart and Staudigel, 1980); Hydrothermal EM < 0.704 (Palmer and Edmond, 1989)

Finally, we apply thermodynamic calculations to test the plausibility of the proposed scenario. The caminite saturation index - based on Pitzer-derived activities (Pitzer and Mayorga, 1973) - is calculated for seawater and the theoretical EM concentrations. The results in Fig. IV.6 show that seawater and EM are strongly undersaturated in the low temperature region and that both solutions are around the state of saturation at temperatures around 200°. Temperatures above 200°C likely induce strong oversaturation. The similarity in SI values for seawater and EM stems from the fact that while SO_4 and Mg concentrations increase in EM solutions, their activity coefficient decreases compared to seawater. Variations in pH between 7 and 8 do not significantly influence the SI region for a given temperature and do not influence the overall interpretation. The good agreement between the calculated fluid EM and caminite solubility at elevated temperatures supports the theory that caminite controls the fluid composition at depth. Taking everything together, caminite dissolution offers the most plausible explanation for the observed fluid deviations in GC51.

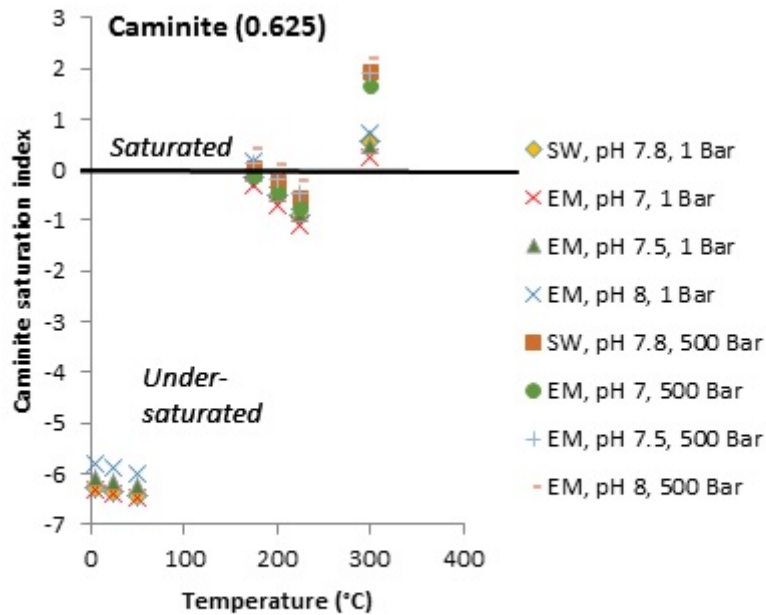


Figure IV.6 Saturation index for caminite (0.625; Janecky and Seyfried, 1983) at varying temperatures for seawater and fluid EM concentrations. For comparison, calculations are shown over a pH range of 7 to 8 and up to 500 bar, highlighting the importance of the temperature effect over the influence of pH and pressure.

IV.4.6 Implications

The presence of caminite confirms the existence of a deep submarine hydrothermal system in the TR, which has not been reported yet in this region. Listric faults offer suitable fluid pathways and advective fluxes, albeit low (0.5 cm/yr), imply an ongoing fluid circulation in the basement. Dissolution of Caminite occurs when temperatures in hydrothermal systems drop below 240°C. Our conclusion is that the system is currently in a waning state. Our conceptual model (Fig. IV.7A) is based on the idea that a magma intrusion in the basement below the volcanic cone is currently cooling and the isotherms are retracting. Fluids circulating through the basement may dissolve caminite at temperatures <240°C, but temperatures are still high enough to drive active fluid convection. Fluids affected by caminite dissolution are transported along the listric faults via diffusion and slow advection through the sediments to the surface (Fig. IV.7B). The fact that caminite starts to dissolve rapidly when temperatures drop it might explain why it has been rarely reported to date. Our findings support the hypothesis by Haymon and Kastner (1986) that caminite can be abundant under specific conditions in hydrothermal recharge zones. To date, only for one further vent, at Brother lower cone (Kermadec arc, SW Pacific), caminite dissolution has been hypothesized to play a role in fluid generation (Kleint et al., 2019). Numerous hydrothermal vents exist in slow spreading settings, e.g. Southwest Indian Ridge (German et al., 1998), but for none of them high Mg/SO₄ fluids have been reported. However, crustal age and geological setting

would be favorable to host this type of vents. For the TR, 251 magmatic intrusions and submarine volcanoes in aged oceanic crust have been reported (Weiß et al., 2015), providing potentially suitable conditions for a widespread formation and dissolution of caminite.

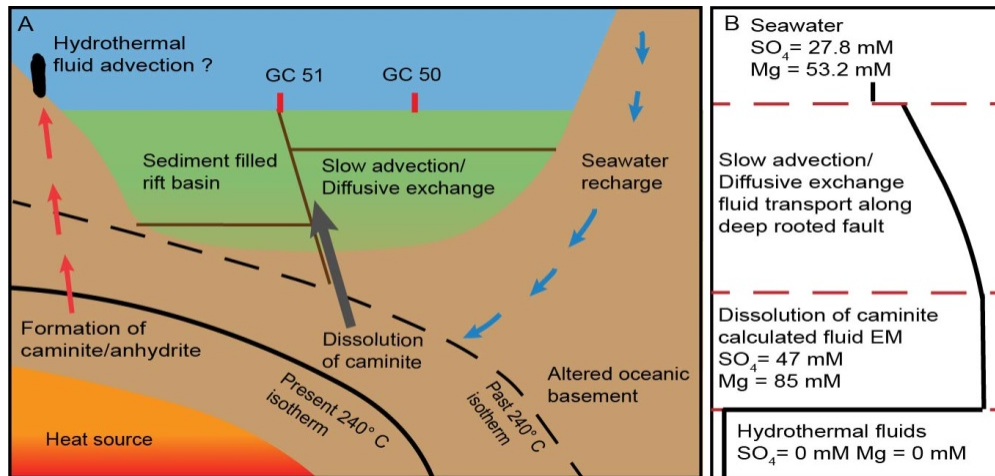


Figure IV.7 A: Conceptual model illustrating evolution of the hydrothermal system. The cooling heat source leads to a retraction of the 240°C isotherm, forcing caminite out of the stability field. Ongoing recharge of seawater dissolves caminite and supports fluid flow along listric faults to the seafloor B: Theoretical depth profile for dissolved SO_4 and Mg concentrations in the subsurface.

IV.5 Summary and conclusions

We present pore fluid data from a gravity core taken at the rim of a submarine lava flow in the TR, which are characterized by high Mg, SO_4 , and total alkalinity concentrations. By applying comprehensive isotope measurements and numerical modeling we could exclude several known diagenetic and hydrothermal processes to cause the observed deviations. The most straight forward explanation for our findings is the dissolution of hydrothermally formed caminite. The literature offers little information on caminite but it has been proposed that it can precipitate under specific conditions in hydrothermal recharge zones, which are generally met in the TR. Thus our findings support the hypothesis by Haymon and Kastner (1986) suggesting that caminite occurrence could be more common than previously thought, especially in active hydrothermal systems before subsiding temperatures induce rapid caminite dissolution. This hydrothermal signal is the first indication of a deep submarine hydrothermal system in the TR. Hydrothermal systems are important sinks for Mg in the global budget (Mottl and Wheat, 1994). A widespread dissolution of caminite in cooling hydrothermal systems might cause a non-negligible reflux of Mg to the ocean. The additional strong fractionation measured for $\delta^{26}\text{Mg}$ isotopes implies neglected effects on the oceanic Mg budget and seawater $\delta^{26}\text{Mg}$.

Acknowledgments, Samples, and Data

We thank Capt. D. Korte and his crew for the excellent support on board R/V Meteor during the expedition M141/1. Without the great help on board of T. Schott, K. Meier, E. Horstmann, and T. Lux this study would not have been possible. We gratefully thank our colleagues B. Domeyer, A. Bleyer, R. Surberg, A. Bodenbinder and A. Kolevica for their help in the shore-based laboratories at GEOMAR. We also thank W. Bach, M. Ligi, B. Tutolo and two anonymous reviewers for helpful comments. M141/1 was funded by the Deutsche Forschungsgemeinschaft (DFG) and the Bundesministerium für Bildung und Forschung (BMBF) with additional support of FLOWS (EU-COST ES 1301).

References

- Alt, J.C. (1995) Sulfur isotopic profile through the oceanic crust: Sulfur mobility and seawater-crustal sulfur exchange during hydrothermal alteration. *Geology* 23, 585-588.
- Alt, J.C. and Honnorez, J. (1984) Alteration of the upper oceanic crust, DSDP site 417: mineralogy and chemistry. *Contributions to Mineralogy and Petrology* 87, 149-169.
- Alt, J.C., Honnorez, J., Laverne, C. and Emmermann, R. (1986) Hydrothermal alteration of a 1 km section through the upper oceanic crust, Deep Sea Drilling Project Hole 504B: Mineralogy, chemistry and evolution of seawater-basalt interactions. *Journal of Geophysical Research: Solid Earth* 91, 10309-10335.
- Amini, M., Eisenhauer, A., Böhm, F., Fietzke, J., Bach, W., Garbe-Schönberg, D., Rosner, M., Bock, B., Lackschewitz, K.S. and Hauff, F. (2008) Calcium isotope ($\delta^{44}/^{40}\text{Ca}$) fractionation along hydrothermal pathways, Logatchev field (Mid-Atlantic Ridge, 14°45'N). *Geochimica et Cosmochimica Acta* 72, 4107-4122.
- Beaulieu, S.E., Baker, E.T., German, C.R. and Maffei, A. (2013) An authoritative global database for active submarine hydrothermal vent fields. *Geochemistry, Geophysics, Geosystems* 14, 4892-4905.
- Beier, C. (2016) Azores Plateau - Cruise No. M128 - July 2 - July 27, 2016 - Ponta Delgada (Azores, Portugal) - Ponta Delgada (Azores, Portugal), METEOR Berichte, p. 42.
- Beier, C., Bach, W., Busch, A.V., Genske, F.S., Hübscher, C. and Krumm, S.H. (2019) Extreme intensity of fluid-rock interaction during extensive intraplate volcanism. *Geochimica et Cosmochimica Acta*.
- Beier, C., Haase, K.M., Abouchami, W., Krienitz, M.S. and Hauff, F. (2008) Magma genesis by rifting of oceanic lithosphere above anomalous mantle: Terceira Rift, Azores. *Geochemistry, Geophysics, Geosystems* 9.
- Boudreau, B.P. (1997) Diagenetic models and their implementation: modelling transport and reactions in aquatic sediments. Springer, Berlin, Heidelberg, Berlin, Heidelberg, New York.

- Butterfield, D.A., McDuff, R.E., Franklin, J. and Wheat, C.G. (1994) 20. Geochemistry of hydrothermal vent fluids from Middle Valley, Juan de Fuca Ridge. Proceedings of the Ocean Drilling Program, Scientific Results Vol. 139.
- Cardigos, F., Colaço, A., Dando, P.R., Ávila, S.P., Sarradin, P.M., Tempera, F., Conceição, P., Pascoal, A. and Serrão Santos, R. (2005) Shallow water hydrothermal vent field fluids and communities of the D. João de Castro Seamount (Azores). *Chemical Geology* 224, 153-168.
- Couto, R.P., Rodriguesa, A.S. and Neto, A.I. (2015) Shallow-water hydrothermal vents in the Azores (Portugal). *Revista de Gestão Costeira Integrada-Journal of Integrated Coastal Zone Management* 15.
- Decker, J. and Helmold, K.P. (1985) The effect of grain size on detrital modes: a test of the Gazzi-Dickinson point-counting method: discussion. *Journal of Sedimentary Research* 55.
- Douville, E., Charlou, J., Oelkers, E., Bienvenu, P., Colon, C.J., Donval, J., Fouquet, Y., Prieur, D. and Appriou, P. (2002) The rainbow vent fluids (36 14' N, MAR): the influence of ultramafic rocks and phase separation on trace metal content in Mid-Atlantic Ridge hydrothermal fluids. *Chemical Geology* 184, 37-48.
- Elderfield, H. and Schultz, A. (1996) Mid-Ocean Ridge hydrothermal fluxes and the chemical composition of the ocean. *Annual Review of Earth and Planetary Sciences* 24, 191-224.
- Escartin, J., Cannat, M., Pouliquen, G., Rabain, A. and Lin, J. (2001) Crustal thickness of V-shaped ridges south of the Azores: Interaction of the Mid-Atlantic Ridge (36–39 N) and the Azores hot spot. *Journal of Geophysical Research: Solid Earth* 106, 21719-21735.
- Gamo, T., Okamura, K., Charlou, J.-L., Urabe, T., Auzende, J.-M., Ishibashi, J., Shitashima, K. and Chiba, H. (1997) Acidic and sulfate-rich hydrothermal fluids from the Manus back-arc basin, Papua New Guinea. *Geology* 25, 139-142.
- Georg, R., Reynolds, B.C., Frank, M. and Halliday, A.N. (2006) New sample preparation techniques for the determination of Si isotopic compositions using MC-ICPMS. *Chemical Geology* 235, 95-104.
- German, C., Baker, E., Mevel, C. and Tamaki, K. (1998) Hydrothermal activity along the southwest Indian ridge. *Nature* 395, 490.
- Gieskes, J.M., Gamo, T. and Brumsack, H. (1991) Chemical methods for interstitial water analysis aboard JOIDES Resolution.
- Gieskes, J.M., Simoneit, B.R.T., Shanks III, W.C., Goodfellow, W.D., James, R.H., Baker, P.A. and Ishibashi, J.-i. (2002) Geochemistry of fluid phases and sediments: relevance to hydrothermal circulation in Middle Valley, ODP Legs 139 and 169. *Applied Geochemistry* 17, 1381-1399.
- Greenberg, J.P. and Moller, N. (1989) The prediction of mineral solubilities in natural waters: A chemical equilibrium model for the Na-K-Ca-Cl-SO₄-H₂O system to high concentration from 0 - 250°C. *Geochimica et Cosmochimica Acta* 53, 2503-2518.
- Gruen, G., Weis, P., Driesner, T., Heinrich, C.A. and de Ronde, C.E. (2014) Hydrodynamic modeling of magmatic–hydrothermal activity at submarine arc volcanoes, with implications for ore formation. *Earth Planet. Sci. Lett.* 404, 307-318.

- Hart, S. and Staudigel, H. (1980) 43. Ocean crust-sea water interaction: Sites 417 and 418, Proceedings of the Ocean Drilling Program: Initial report. National Science Foundation, p. 1169.
- Haymon, R.M. and Kastner, M. (1986) Caminite; a new magnesium-hydroxide-sulfate-hydrate mineral found in a submarine hydrothermal deposit, East Pacific Rise, 21 degrees N. *American Mineralogist* 71, 819-825.
- Hübscher, C. (2012) RV METEOR, Cruise Report M79/L2. August 26–September 21, 2009, Ponta Delgada (Azores/Portugal)–Las Palmas (Canary Islands/Spain). Institut für Geophysik.
- Hübscher, C. and Gohl, K. (2014) Reflection/Refraction seismology. *Encycl. Mar. Geosciences*.
- Humphris, S.E. and Thompson, G. (1978) Hydrothermal alteration of oceanic basalts by seawater. *Geochimica et Cosmochimica Acta* 42, 107-125.
- Janecky, D. and Seyfried, W. (1983) The solubility of magnesium-hydroxide sulfate-hydrate in seawater at elevated temperatures and pressures. *American Journal of Science* 283, 831-860.
- Kleint, C., Bach, W., Diehl, A., Fröhberg, N., Garbe-Schönberg, D., Hartmann, J.F., de Ronde, C.E., Sander, S.G., Strauss, H. and Stucker, V.K. (2019) Geochemical characterization of highly diverse hydrothermal fluids from volcanic vent systems of the Kermadec intraoceanic arc. *Chemical Geology*, 119289.
- Ligi, M., Bonatti, E., Cuffaro, M. and Brunelli, D. (2013) Post-Mesozoic rapid increase of seawater Mg/Ca due to enhanced mantle-seawater interaction. *Scientific reports* 3.
- Liu, P.-P., Teng, F.-Z., Dick, H.J.B., Zhou, M.-F. and Chung, S.-L. (2017) Magnesium isotopic composition of the oceanic mantle and oceanic Mg cycling. *Geochimica et Cosmochimica Acta* 206, 151-165.
- Morgan, J.L., Gordon, G.W., Arrua, R.C., Skulan, J.L., Anbar, A.D. and Bullen, T.D. (2011) High-precision measurement of variations in calcium isotope ratios in urine by multiple collector inductively coupled plasma mass spectrometry. *Analytical chemistry* 83, 6956-6962.
- Nesbitt, H.W. and Young, G. (1982) Early Proterozoic climates and plate motions inferred from major element chemistry of lutites. *Nature* 299, 715.
- Pabalan, R.T. and Pitzer, K.S. (1987) Thermodynamics of concentrated electrolyte mixtures and the prediction of mineral solubilities to high temperatures for mixtures in the system Na-K-Mg-Cl-SO₄-OH-H₂O. *Geochimica et Cosmochimica Acta* 51, 2429-2443.
- Palmer, M.R. and Edmond, J.M. (1989) The strontium isotope budget of the modern ocean. *Earth Planet. Sci. Lett.* 92, 11-26.
- Pelletier, G., Lewis, E. and Wallace, D. (2005) A calculator for the CO₂ system in seawater for Microsoft Excel/VBA. Washington State Department of Ecology, Olympia, WA, Brookhaven National Laboratory, Upton, NY.
- Pitzer, K.S. and Mayorga, G. (1973) Thermodynamics of electrolytes. II. Activity and osmotic coefficients for strong electrolytes with one or both ions univalent. *The Journal of Physical Chemistry* 77, 2300-2308.

- Romaniello, S., Field, M., Smith, H., Gordon, G., Kim, M. and Anbar, A. (2015) Fully automated chromatographic purification of Sr and Ca for isotopic analysis. *Journal of Analytical Atomic Spectrometry* 30, 1906-1912.
- Schacht, U., Wallmann, K., Kutterolf, S. and Schmidt, M. (2008) Volcanogenic sediment-seawater interactions and the geochemistry of pore waters. *Chemical Geology* 249, 321-338.
- Scholz, F., Hensen, C., De Lange, G.J., Haeckel, M., Liebetrau, V., Meixner, A., Reitz, A. and Romer, R.L. (2010) Lithium isotope geochemistry of marine pore waters - Insights from cold seep fluids. *Geochimica et Cosmochimica Acta* 74, 3459-3475.
- Scholz, F., Löscher, C.R., Fiskal, A., Sommer, S., Hensen, C., Lomnitz, U., Wuttig, K., Göttlicher, J., Kossel, E. and Steininger, R. (2016) Nitrate-dependent iron oxidation limits iron transport in anoxic ocean regions. *Earth Planet. Sci. Lett.* 454, 272-281.
- Seewald, J.S., Reeves, E.P., Bach, W., Saccocia, P.J., Craddock, P.R., Shanks, W.C., Sylva, S.P., Pichler, T., Rosner, M. and Walsh, E. (2015) Submarine venting of magmatic volatiles in the Eastern Manus Basin, Papua New Guinea. *Geochimica et Cosmochimica Acta* 163, 178-199.
- Sommer, S., Linke, P., Pfannkuche, O., Schleicher, T., Schneider v. Deimling, J., Reitz, A., Haeckel, M., Flögel, S. and Hensen, C. (2009) Seabed methane emissions and the habitat of frenulate tubeworms on the Captain Arutyunov mud volcano (Gulf of Cadiz). *Marine Ecology Progress Series* 382, 69-86.
- Teagle, D.A.H., Alt, J.C. and Halliday, A.N. (1998) Tracing the chemical evolution of fluids during hydrothermal recharge: Constraints from anhydrite recovered in ODP Hole 504B. *Earth Planet. Sci. Lett.* 155, 167-182.
- Teng, F.-Z. (2017) Magnesium Isotope Geochemistry. *Reviews in Mineralogy and Geochemistry* 82, 219-287.
- Van der Plas, L. and Tobi, A. (1965) A chart for judging the reliability of point counting results. *American Journal of Science* 263, 87-90.
- Vogl, J., Brandt, B., Noordmann, J., Rienitz, O. and Malinovskiy, D. (2016) Characterization of a series of absolute isotope reference materials for magnesium: ab initio calibration of the mass spectrometers, and determination of isotopic compositions and relative atomic weights. *Journal of Analytical Atomic Spectrometry* 31, 1440-1458.
- Vogl, J. and Pritzkow, W. (2010) Isotope reference materials for present and future isotope research. *Journal of Analytical Atomic Spectrometry* 25, 923-932.
- Vogt, P.R. and Jung, W.Y. (2004) The Terceira Rift as hyper-slow, hotspot-dominated oblique spreading axis: A comparison with other slow-spreading plate boundaries. *Earth Planet. Sci. Lett.* 218, 77-90.
- von Eynatten, H. and Gaupp, R. (1999) Provenance of Cretaceous synorogenic sandstones in the Eastern Alps: constraints from framework petrography, heavy mineral analysis and mineral chemistry. *Sedimentary Geology* 124, 81-111.
- Weiß, B.J., Hübscher, C., Wolf, D. and Lüdmann, T. (2015) Submarine explosive volcanism in the southeastern Terceira Rift/São Miguel region (Azores). *Journal of Volcanology and Geothermal Research* 303, 79-91.

White, W., Schilling, J.-G. and Hart, S. (1976) Evidence for the Azores mantle plume from strontium isotope geochemistry of the Central North Atlantic. *Nature* 263, 659.

Wieser, M.E., Buhl, D., Bouman, C. and Schwieters, J. (2004) High precision calcium isotope ratio measurements using a magnetic sector multiple collector inductively coupled plasma mass spectrometer. *Journal of Analytical Atomic Spectrometry* 19, 844-851.

Wimpenny, J., Colla, C.A., Yin, Q.-Z., Rustad, J.R. and Casey, W.H. (2014) Investigating the behaviour of Mg isotopes during the formation of clay minerals. *Geochimica et Cosmochimica Acta* 128, 178-194.

Wolfram Research, I. (2018) *Mathematica*, 11.3 ed. Wolfram Research, Inc., Champaign, Illinois.

Wombacher, F., Eisenhauer, A., Heuser, A. and Weyer, S. (2009) Separation of Mg, Ca and Fe from geological reference materials for stable isotope ratio analyses by MC-ICP-MS and double-spike TIMS. *Journal of Analytical Atomic Spectrometry* 24, 627-636.

V. Conclusion

The primary focus of this thesis was to characterize fluid expulsion on the Nubian/Eurasian plate boundary in the North Atlantic Ocean. Chapter II focuses on the genesis of fluids of Mud Volcanoes in the Gulf of Cadiz. Chapter III gives a regional overview about pore fluid patterns of the Azores Plateau and presents indications for hydrothermal activity on the plateau. Chapter IV is based on a multi isotope and element study to identify the source for an unusual high Mg and SO₄ enriched fluid in the Terceira Rift.

The novel coupled 1D reaction transport model, described in chapter II, is a major step forward in geochemical basin scale modelling. The realistic coupling of geophysical and geochemical parameters allows us to reproduce the evolution of fluids emitted by mud volcanoes. With the model framework further evidence could be provided for the hypothesis that distal mud volcanoes in the Gulf of Cadiz are recharged by fluids flowing through aged crust (>140 Ma basement).

A major finding of this thesis is the first geochemical indication for hydrothermal activity on the Azores Plateau remote to the Mid Atlantic Ridge. Based on geochemical findings combined with seismic evidence I can present here indications for four vents. During various sea going expeditions campaigns were undertaken to localize vents on the Azores Plateau. With the now available indications a more detailed sampling campaign can be carried out, focusing on geochemical fluid variations, biogeochemical reactions and if sea floor mineralization's are present.

Furthermore, this study can present indications for another hydrothermal vent in the Terceira Rift, the northern boundary of the Azores plateau. At a sample location in the Hirondele Basin an unusual pore water signal was found. The pore water is marked by high Mg, SO₄ and total alkalinity values, being completely different to typical hydrothermal fluids. The samples were taken close to a lava flow and in the vicinity of a major listric fault. Here a multi-isotope approach (⁸⁷Sr/⁸⁶Sr, δ^{26} Mg, δ^{34} S, δ^{30} Si and $\delta^{44/42}$ Ca) was employed to identify dissolution of caminite as the most likely source of the observed fluid signature and to exclude other hypothesis. Caminite is a rare mineral in hydrothermal vents, only found once before, but postulated to be abundant under specific conditions such as high temperatures and aged oceanic crust present. The Terceira Rift provides these specific conditions. Here we present the first field data showing that caminite can be an abundant mineral as previously

proposed. This result can have important implications for the global Mg cycle and the marine $\delta^{26}\text{Mg}$ budget. This process can provide an abundant reflux of Mg from hydrothermal systems. To date these systems are only seen as sinks for Mg, but abundant caminite occurrence could partly reverse this flux. Fig. V.1 shows a map with crustal age of the seafloor and hydrothermal systems. According to the pre-defined conditions other places for caminite occurrence are e.g. Pitcairn Hotspot, the Tonga and Kermadec Trench, the Caribbean Sea or at the SW Indian Ridge. However, a thorough investigation has to be carried out first in the Terceira Rift to understand the formation of caminite occurrence in recharge zones to define other possible locations with caminite occurrence.

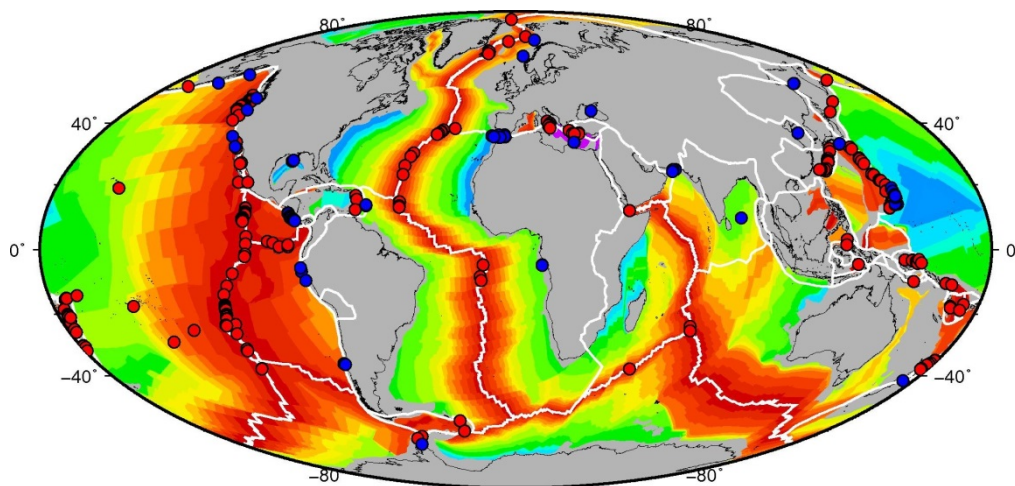


Fig. V.1. World map with ocean floor crustal age from Mueller (2008) with locations of hydrothermal systems (red circles) and cold seeps (blue circles); map was created by R. Bartolome

Overall, this thesis reveals that fluids are circulating on the western and eastern end of the Nubian/Eurasian Plate boundary. This interaction of fluids with aged oceanic basement, does indicate that fluid flow on the Gloria Transform Fault, the largest segment of the Nubian/Eurasian Plate boundary, could be possible and fluid circulation is not only present at spreading centers and convergent margins.

Acknowledgements

A special thank you to Christian Hensen for all the support you gave me in the past years. You helped me a lot with endless discussions, encouragement and reading over and over the drafts. Thank you for letting me share an office with you for my first four years at GEOMAR, I have learned a lot in this time.

Many thanks to Klaus Wallmann to accept me as a doctoral candidate. I have enjoyed to sail with you twice during my time here. You have showed me how to work scientifically with a high standard and your constructive criticism helped my progress tremendously.

I also would like to thank Laura Haffert, Kristin Hamann, Christian Deusner and Elke Kossel who I had the pleasure to share the office with, for the past 2 years. I enjoyed unlocking the door for you every morning and be there first, to welcome you all and also the “Lange Nacht der Wissenschaften” with food and maybe sometimes cold drinks, which always helped to push forward this thesis.

This thesis could never have been completed without the assistance of Bettina Domeyer, Anke Bleyer, Regina Surberg, Andrea Bodenbinder and Jutta Heinze. Thank you for your support and the great data set you provided me with.

I would like to thank Ewa Burwicz, Volker Liebetrau, Mark Schmidt, Steffen Kutterolf, Thor Hansteen and Matthias Haeckel for numerous discussions and support during the past years. I have learned a lot about numerical models, isotopes systems and head space gas sampling.

A warm thank you to my wife Mirja Heinrich for all your support in past years. I am looking forward to our future with our offspring.

Lastly, I would like to thank my family for the support you gave me from the beginning of my studies. None of us would have dared to dream at the beginning where this trip will go.

1 Appendix A for chapter II

2 A1.1 Governing equations

3 The 1D model used for this study is based on the assumption that the pore space is fully saturated by
4 fluids. Sediment grains and fluids are transported downwards according to the burial velocity. The
5 burial velocity of solids is derived from the sedimentation rate from DSDP Site 135 on Coral Patch
6 Ridge (Hayes et al., 1972). The mass balance for solids reads as follows:

$$7 \frac{\partial((1-\Phi)\rho_s)}{\partial t} = -\nabla \cdot ((1-\Phi)\rho_s \vec{V}_s) + Q_s \quad (\text{A1})$$

8 where ϕ - porosity, ρ_s - solid density, V_s - burial velocity of solids, t - time and Q_s - source term for
9 mineral reactions.

10 The mass balance for fluids reads as follows:

$$11 \frac{\partial(\phi\rho_f)}{\partial t} = -\nabla \cdot (\phi\rho_f \vec{V}_f) + Q_f \quad (\text{A2})$$

12 where ρ_f - fluid density, V_f - fluid phase velocity and Q_f - source term for biogeochemical reactions in
13 the fluid phase.

14 Concentrations of dissolved species are transported by diffusion and advection after following
15 equation:

$$16 \frac{\partial(\phi C)}{\partial t} = -\nabla \cdot (\phi D_s \nabla C) - \nabla \cdot (\phi C \vec{V}_f) + Q_{fc} \quad (\text{A3})$$

17 where, C - concentration of solutes, D_s - diffusion coefficient, and Q_{fc} - source term for biogeochemical
18 reactions of each chemical species in the fluid phase. Fluid velocity V_f was calculated after the Darcy
19 formulation which reads as

$$20 \vec{U}_f = \phi(\vec{V}_f - \vec{V}_s) = -\frac{k}{\mu_f}(\nabla P - \rho_f \vec{g}) \quad (\text{A4})$$

21 where U_f – Darcy fluid velocity, k - intrinsic permeability, μ_f - viscosity of fluid phase, ∇P - pressure
22 gradient, and g - gravitational acceleration. The viscosity of fluids depends on temperature and
23 pressure, however, here we used a constant average value (see Table A1).

24 The temperature-dependent molecular diffusion coefficients of dissolved species in the fluid are
25 calculated according to Boudreau (1997). The diffusion coefficient D_s is the molecular diffusion
26 coefficient scaled by the tortuosity, which is calculated using the following equation (Boudreau
27 1997):

28 $T_o = 1 - 2 \cdot \log(\phi)$ (A5)

29 The intrinsic permeability can be derived with the Kozeny-Carman relation. This relationship is
30 defined after Hantschel and Kauerauf (2009) as:

31 $k = \frac{B \cdot \phi^3}{T_o^2 \cdot S^2}$ (A6)

32 where B- is the scaling factor and S- is the specific sediment surface area. Values for S and B that are
33 applied to characterize the permeability of the GoC lithologies are based on Hantschel and Kauerauf
34 (2009) (Table A1).

35 **A1.2 Pressure equations**

36 The lithostatic pressure, assuming a constant sediment grain density, has been calculated according to
37 following equation after Hantschel and Kauerauf (2009)

38 $P_{Litho(z)} = \rho_{seawater} \cdot g \cdot wd + P_{Aero} + g \cdot \int_{z_0}^z (\rho_f \phi + \rho_s (1 - \phi)) dz$ (A7)

39 where P_{Litho} - lithostatic pressure, $\rho_{seawater}$ - seawater density, wd- water depth, P_{Aero} - atmospheric
40 pressure, z_0 - seafloor and z- sediment depth.

41 The effective pore fluid pressure P calculation is based on the Terzaghi's effective stress definition
42 and accounts for compressible fluids and incompressible grains. P is calculated according to the
43 following equation:

44 $\rho_f \left(\phi \beta_f + \frac{\zeta}{(1-\phi)} \right) \frac{\partial P}{\partial t} - \nabla \cdot \left(\frac{\rho_f k}{\mu_f} \nabla P \right) = \nabla \cdot \left(\frac{\rho_f k}{\mu_f} (\rho_f \vec{g}) \right) + \frac{\rho_f \zeta}{(1-\phi)} \frac{\partial P_{Litho}}{\partial t} - \frac{\partial \rho_f}{\partial t} + Q_{Reaction}$ (A8)

45 where β_f - compressibility factor for fluids, ζ - sediment compaction parameter, P the effective pore
46 fluid pressure, and $Q_{Reaction}$ source term for pore fluid released from chemical reactions.

47 The first term on the LHS of the pore pressure equation (A8) accounts for a density change of fluid
48 with time. A compressibility factor for fluids (β_f) is calculated as:

49 $\beta_f \rho_f = \frac{\partial \rho_f}{\partial P}$ (A9)

50 The first term on the RHS accounts for mobility of a fluid due to the pressure change and gravitational
51 flow. The second last term on the RHS, the volume expansion term, describes changes in fluid density
52 with time, and the last term is the source term.

53 The effective stress calculation is used to estimate the porosity reduction due to sediment compaction.
 54 Thus, the actual state of the pore fluid pressure P is used to calculate the amount of pore fluids
 55 expelled from the matrix. The effective stress reads as follows:

$$56 \quad \sigma'_z = P_{Litho} - P \quad (A10)$$

57 where σ'_z - the effective stress. The porosity is calculated after modified Athy's law taking into
 58 account the effective stress:

$$59 \quad \phi = \phi_{res} + \phi_0 e^{-\zeta \sigma'_z} \quad (A11)$$

60 where ϕ_{res} - residual porosity, ϕ_0 - initial porosity. The residual porosity stands for the irreducible
 61 fraction of the pore space filled by pore fluids.

62 **A1.3 Temperature**

63 The temperature field is determined using an average constant basement heat flow over time, and
 64 constant sediment water interface temperature (T_0). Heat is transported via advection and diffusion in
 65 the model domain. The temperature distribution (T) reads as follows:

$$66 \quad \frac{\partial}{\partial t} \left((\rho C_p)_{bulk} T \right) = -\nabla \cdot \left(\left((\rho C_p)_{bulk} \overline{V_s} \right) T \right) - \nabla \cdot \left((\rho_f C_f \overline{U_f}) T \right) + \nabla \cdot (\lambda_{bulk} \nabla T)$$

67 (A12)

68 where $(\rho C_p)_{bulk}$ - volumetric heat capacity, C_{pf} - heat capacity of fluids, and λ_{bulk} - thermal conductivity.

69 The bulk volumetric heat capacity accounts for the solid and fluid phase and reads as follows:

$$70 \quad (\rho C_p)_{bulk} = (1 - \phi) \rho_s C_{ps} + \phi \rho_f C_{pf} \quad (A13)$$

71 where ρ_s - density and C_{ps} - heat capacity for solids, and respectively ρ_f and C_{pf} for fluids. The bulk
 72 thermal conductivity can be expressed after Deming and Chapman (1989) as

$$73 \quad \lambda_{bulk} = \lambda_s^{1-\phi} \lambda_f^\phi \quad (A14)$$

74 where λ_s - average thermal conductivity for solids, and λ_f - fluid respectively. Here we used constant
 75 values for thermal conductivities for solids and species. A list of all input parameters is provided in
 76 Table A1.

77

78

79

80 **Table A1: Parameters used in the governing equations of the basin model.**

Parameter	Symbol	Value	References
Gravitational acceleration	g	$9.81 \text{ m} \cdot \text{s}^{-2}$	-
Time step	dt	200 000 years	-
Density of solids	ρ_s	$2600 \text{ kg} \cdot \text{m}^{-3}$	-
Density of fluids	ρ_f	$1000 \text{ kg} \cdot \text{m}^{-3}$	-
Geometrical factor	B	10	Based on Hantschel and Kauerauf (2009)
Specific surface area	S	$10^5 \text{ m}^2 \cdot \text{m}^{-3}$	Based on Hantschel and Kauerauf (2009)
Dynamic viscosity of fluid	μ_f	$10^{-3} \text{ Pa} \cdot \text{s}$	Xu and Germanovich (2006)
Thermal conductivity of solids	λ_s	$2.0 \text{ W} \cdot \text{m}^{-1} \cdot \text{K}^{-1}$	Hantschel and Kauerauf (2009)
Thermal conductivity of fluid	λ_f	$0.6 \text{ W} \cdot \text{m}^{-1} \cdot \text{K}^{-1}$	Hantschel and Kauerauf (2009)
Specific heat capacity of solids	$C_{ps(\text{clay})}$	$940 \text{ J} \cdot \text{kg}^{-1} \cdot \text{K}^{-1}$	Hantschel and Kauerauf (2009)
	$C_{ps(\text{carbonate})}$	$840 \text{ J} \cdot \text{kg}^{-1} \cdot \text{K}^{-1}$	Hantschel and Kauerauf (2009)
Specific heat capacity of fluid	C_{pf}	$4181.3 \text{ J} \cdot \text{kg}^{-1} \cdot \text{K}^{-1}$	Hantschel and Kauerauf (2009)
Sedimentation rate of solids 155 Ma - 120 Ma	$V_{S \text{ 155 - 120 Ma}}$	$55 \text{ m} \cdot \text{Ma}^{-1}$	Modified after Hayes et al. (1972)
Sedimentation rate of solids 120 Ma - 25 Ma	$V_{S \text{ 120 - 25 Ma}}$	$25 \text{ m} \cdot \text{Ma}^{-1}$	Modified after Hayes et al. (1972)
Sedimentation rate of solids 25 Ma - 0 Ma	$V_{S \text{ 25 - 0 Ma}}$	$150 \text{ m} \cdot \text{Ma}^{-1}$	Modified after Hayes et al. (1972)
Seawater Temperature	T_0	4°C	-
Atmospheric pressure	P_{aero}	101325 Pa	-
Compressibility of fluid	β_f	$4 \cdot 10^{-10} \text{ Pa}^{-1}$	Hantschel and Kauerauf (2009)
Initial porosity	$\phi_{0(\text{clay})}$	0.6	Hantschel and Kauerauf (2009)
	$\phi_{0(\text{carbonate})}$	0.5	Hantschel and Kauerauf (2009)
Sediment compaction parameter	ζ_{clay}	$1.7 \cdot 10^{-7} \text{ Pa}^{-1}$	Hantschel and Kauerauf (2009)
	$\zeta_{\text{carbonate}}$	$1.176 \cdot 10^{-7} \text{ Pa}^{-1}$	Hantschel and Kauerauf (2009)
Intrinsic permeability	k	Equation A6	Hantschel and Kauerauf (2009)

81

82

Table A2 Parameter variations for case studies and scenarios

	<i>Clay dehydration</i>							<i>Carbonate recrystallization</i>				<i>Advection trough</i> <i>crust in kg s⁻¹ m⁻²</i>
	Alpha	Betta	Frequency Factor	Activation Energy	⁸⁷ Sr/ ⁸⁶ Sr of smectite	wt% water in smectite	Sr in smectite (X _{Sr})	Alpha	Betta	Gamma	K	Flow rate through LBC (5 - 0 Ma)
CAMV												
Parameter test												
Scenario 1	5	0.25	3.00E-10	20000	0.7100	22.5	0.4	-	-	-	-	-
Scenario 2	5	0.25	90	120000	0.7100	22.5	0.4	-	-	-	-	-
Scenario 3	5	0.25	3.5e-8	38500	0.7100	22.5	0.4	-	-	-	-	-
CAMV												
Heat flow test												
Scenario 1	5	0.25	3.50E-08	38500	0.7100	22.5	0.4	-	-	-	-	-
Scenario 2	5	0.25	3.50E-08	38500	0.7100	22.5	0.4	-	-	-	-	-
ATI MV												
Scenario 1	5	0.25	3.50E-08	38500	0.7100	22.5	0.4	1.00E-07	0.05	4	20	-
Scenario 2	5	0.25	3.50E-08	38500	0.7100	22.5	0.4	1.00E-07	0.05	4	50	-
Porto MV												
Scenario 1	5	0.25	3.50E-08	38500	0.7095	25.0	0.2	-	-	-	-	-
Scenario 2	5	0.25	3.50E-08	38500	0.7095	25.0	0.2	1.00E-07	0.05	4	50	-
Scenario 3	5	0.25	3.50E-08	38500	0.7095	25.0	0.2	1.00E-07	0.05	4	50	-
Scenario 4	5	0.25	3.50E-08	38500	0.7095	25.0	0.2	1.00E-07	0.05	4	50	1.5E-04

References

Boudreau, B.P. (1997) Diagenetic models and their implementation: modelling transport and reactions in aquatic sediments. Springer, Berlin, Heidelberg, Berlin, Heidelberg, New York.

Deming, D. and Chapman, D.S. (1989) Thermal histories and hydrocarbon generation-example from the Utah-Wyoming thrust belt. AAPG Bull.-Am. Assoc. Petr. Geol. 73, 1455-1471.

Hantschel, T. and Kauerauf, A.I. (2009) Fundamentals of basin and petroleum systems modeling. Springer Science & Business Media.

Hayes, D.E., Pimm, A.C., Beckmann, J.P., Benson, W.E., Berger, W.H., Roth, P.H., Supko, P.R. and von Rad, U. (1972) Site 135, DSDP, Initial Reports U.S. Government Printing Office, Washington, D.C, pp. 15-48.

Xu, W. and Germanovich, L.N. (2006) Excess pore pressures resulting from methane hydrate dissociation in marine sediments: A theoretical approach. Journal of Geophysical Research 111, doi:10.1029/2004JB003600.

Appendix B for chapter III

B1. Model parameters

Table B1 Model parameters for AOM models

Parameter	Value	Unit	Reference
<i>General Parameters</i>			
Temperature	4	°C	Approximated by field data
Pressure	100	bar	Approximated by field data
Salinity	35	‰	Approximated by field data
Molar N:C ratio during POM degradation	16:106		
Sedimentation Rate	3.5	cm ka ⁻¹	Vlag et al. (2004) Approximated by field data
Density	2.65	g cm ⁻³	Approximated by field data
<i>Upper Boundary concentrations</i>			
SO ₄	29.7	mM	Approximated by field data
CH ₄	0	mM	Approximated by field data
NH ₄	0	mM	Approximated by field data
DIC	2.71	mM	Approximated by field data
Ca	10.5	mM	Approximated by field data
Total Alkalinity	2.7	meq/L	Approximated by field data
<i>Rate parameters</i>			
Constant for inhibition of POC degradation	35	mM	Wallmann et al. (2006)
Monod constant for SO ₄ reduction	1	mM	Boudreau (1997)
<i>Model specific parameters</i>			
GC10			
Porosity at sediment surface	0.65		fitted to data
Porosity at maximum depth	0.45		fitted to data
Maximum depth of calculation	50	m	fitted to data
Rain rate of POC to the seabed	9.9 * 10 ⁻⁶	g cm ⁻² yr ⁻¹	fitted to data
Kinetic constant for CH ₄ oxidation	0.8	1 yr ⁻¹	fitted to Data

(k_{AOM})			
Exponent decrease in POC reactivity	1	-	fitted to Data

Lower Boundary concentrations GC10

SO ₄	0	mM	fitted to data
CH ₄	5	mM	fitted to data
NH ₄	2.6	mM	fitted to data
DIC	40	mM	fitted to data
Ca	0	mM	fitted to data
Total Alkalinity	2.7	meq/L	fitted to data

GC20

Porosity at sediment surface	0.8		fitted to data
Porosity at maximum depth	0.5		fitted to data
Maximum depth of calculation	100	m	-
Rain rate of POC to the seabed	$4 * 10^{-6}$	$g\ cm^{-2}\ yr^{-1}$	fitted to data
Kinetic constant for CH ₄ oxidation (k_{AOM})	1	$1\ yr^{-1}$	fitted to data
Exponent decrease in POC reactivity	0.9	-	fitted to data

Lower Boundary concentrations GC20

SO ₄	0	mM	fitted to data
CH ₄	30	mM	fitted to data
NH ₄	0.45	mM	fitted to data
DIC	40	mM	fitted to data
Ca	0	mM	fitted to data
Total Alkalinity	2.7	meq/L	fitted to data

GC27

Porosity at sediment surface	0.8		fitted to data
Porosity at maximum depth	0.5		fitted to data
Maximum depth of calculation	200	m	fitted to data
Rain rate of POC to the seabed	$9.9 * 10^{-6}$	$g\ cm^{-2}\ yr^{-1}$	fitted to data
Kinetic constant for CH ₄ oxidation (k_{AOM})	1	$1\ yr^{-1}$	fitted to data
Exponent decrease in POC reactivity	1	-	fitted to data

Lower Boundary concentrations GC27

SO ₄	0	mM	fitted to data
CH ₄	5	mM	fitted to data
NH ₄	2.3	mM	fitted to data
DIC	40	mM	fitted to data
Ca	0	mM	fitted to data
Total Alkalinity	2.7	meq/L	fitted to data

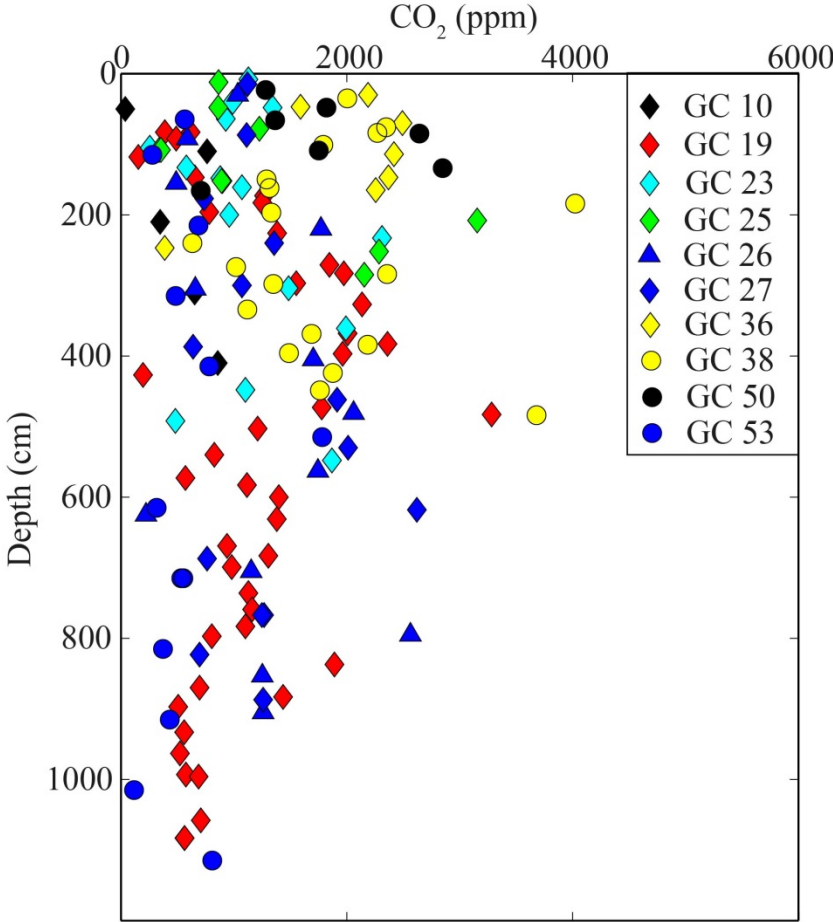
- Boudreau, B. P., 1997, *Diagenetic models and their implementation: modelling transport and reactions in aquatic sediments*, Berlin, Heidelberg, New York, Springer, Berlin, Heidelberg, 414 p.:
- Vlag, P. A., Kruiver, P. P., and Dekkers, M. J., 2004, Evaluating climate change by multivariate statistical techniques on magnetic and chemical properties of marine sediments (Azores region): *Palaeogeography, Palaeoclimatology, Palaeoecology*, v. 212, no. 1, p. 23-44.
- Wallmann, K., Aloisi, G., Haeckel, M., Obzhairov, A., Pavlova, G., and Tishchenko, P., 2006, Kinetics of organic matter degradation, microbial methane generation, and gas hydrate formation in anoxic marine sediments: *Geochimica et Cosmochimica Acta*, v. 70, no. 15, p. 3905-3927.

Table B2 Model Parameters for calcium carbonate recrystallization models

Parameter	Value	Unit	Reference
<i>Upper Boundary concentrations</i>			
Sr	91	μM	
$^{87}\text{Sr}/^{86}\text{Sr}$	0.7092	-	Banner (2004)
GC19			
α	0.1	-	fitted to data
β	0.6	-	fitted to data
γ	4.0	-	fitted to data
Carbonate	53	wt%	fitted to data
Model column	30	m	fitted to data
$^{87}\text{Sr}/^{86}\text{Sr}$ Carbonate	0.7090	-	Banner (2004)
Porosity at sediment surface	0.78	-	fitted to data
Porosity at maximum depth	0.60	-	fitted to data
GC31			
α	0.005	-	fitted to data
β	0.8	-	fitted to data
γ	4.0	-	fitted to data
Carbonate	70	wt%	fitted to data
Model column	50	m	fitted to data
$^{87}\text{Sr}/^{86}\text{Sr}$ Carbonate	0.7090	-	Banner (2004)
Porosity at sediment surface	0.70	-	fitted to data
Porosity at maximum depth	0.55	-	fitted to data

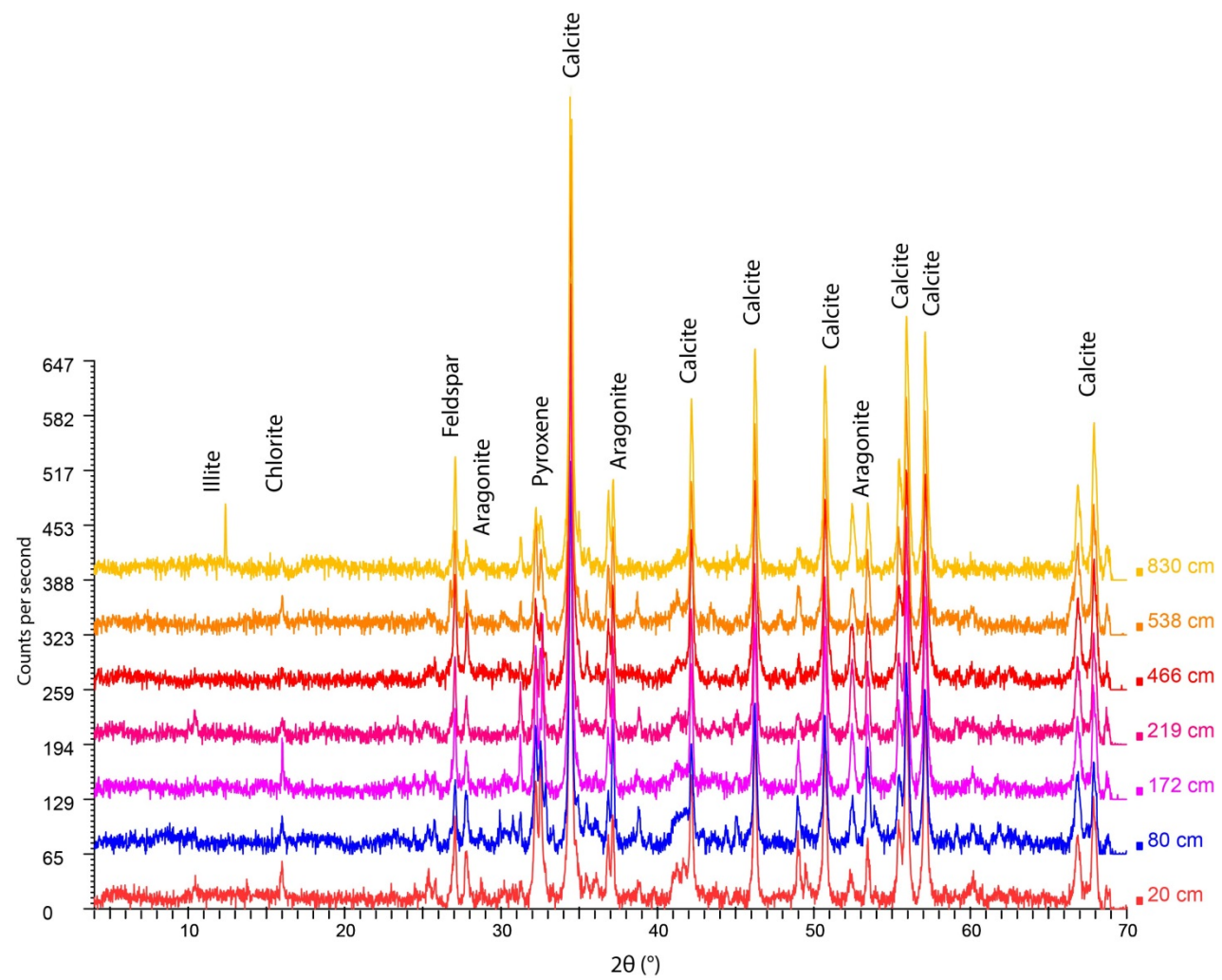
Banner, J. L., 2004, Radiogenic isotopes: systematics and applications to earth surface processes and chemical stratigraphy: *Earth Science Review*, v. 65, p. 141-194.

B2. Head space gas CO₂

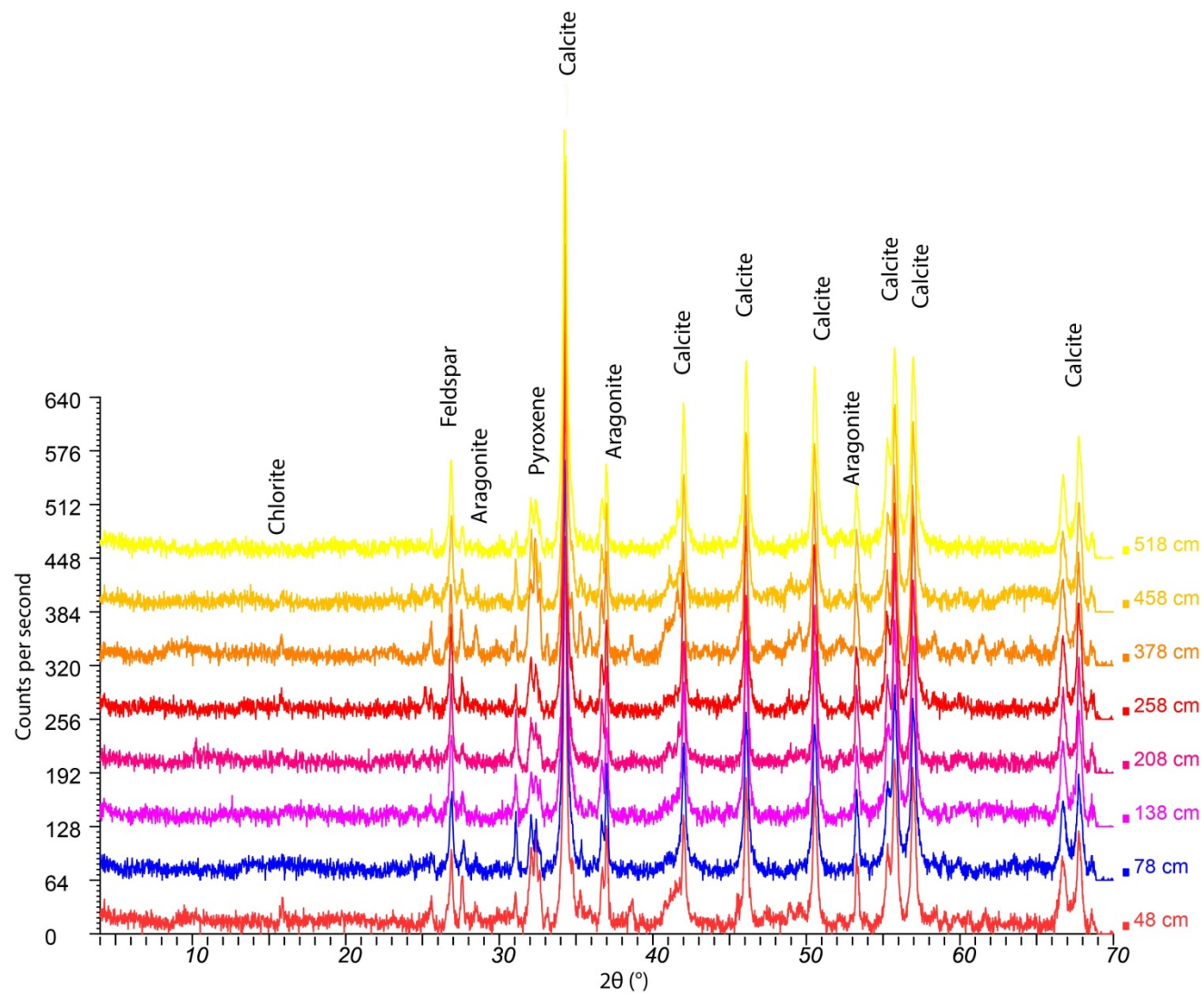


B3. XRD results

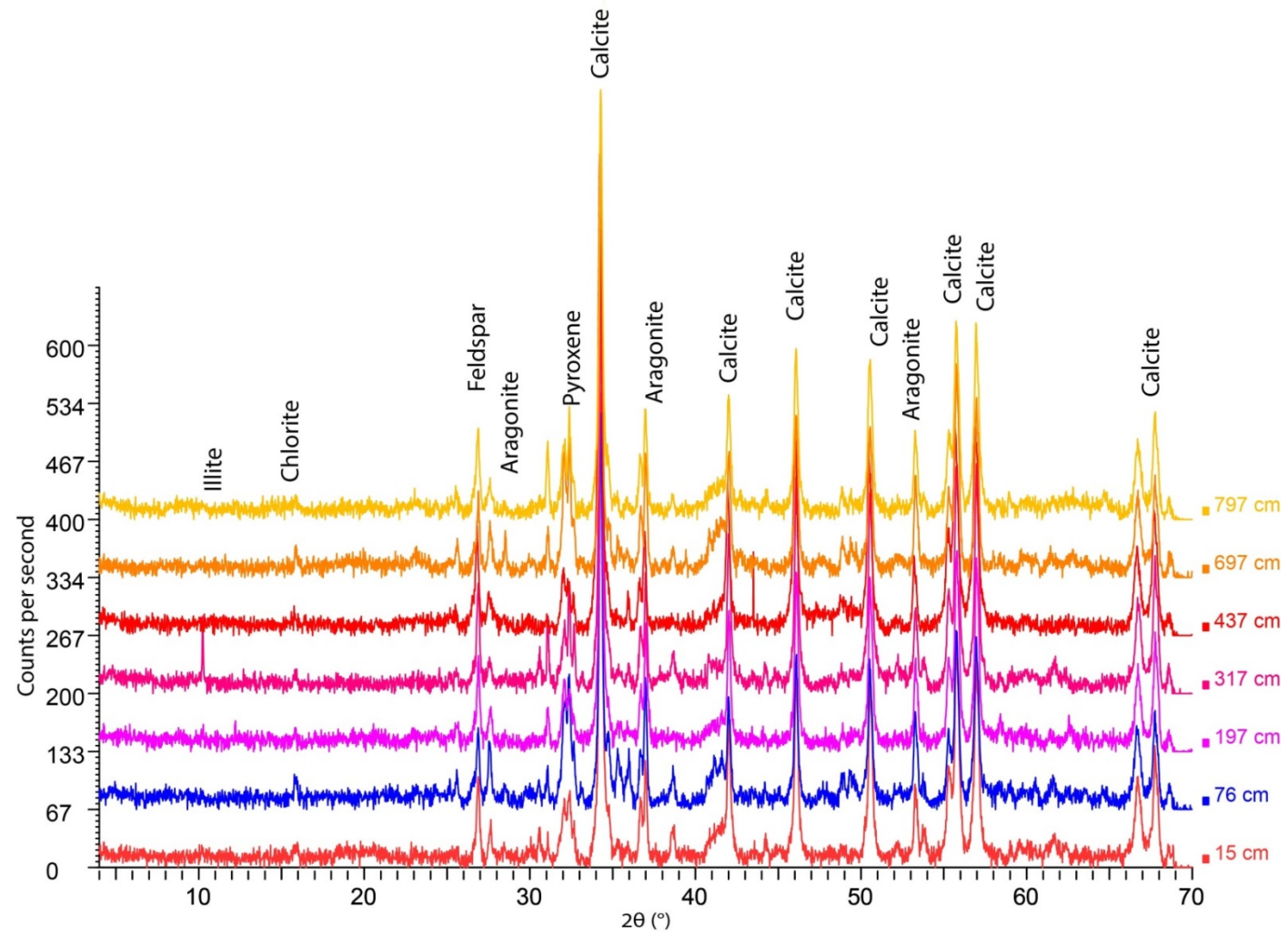
GC13



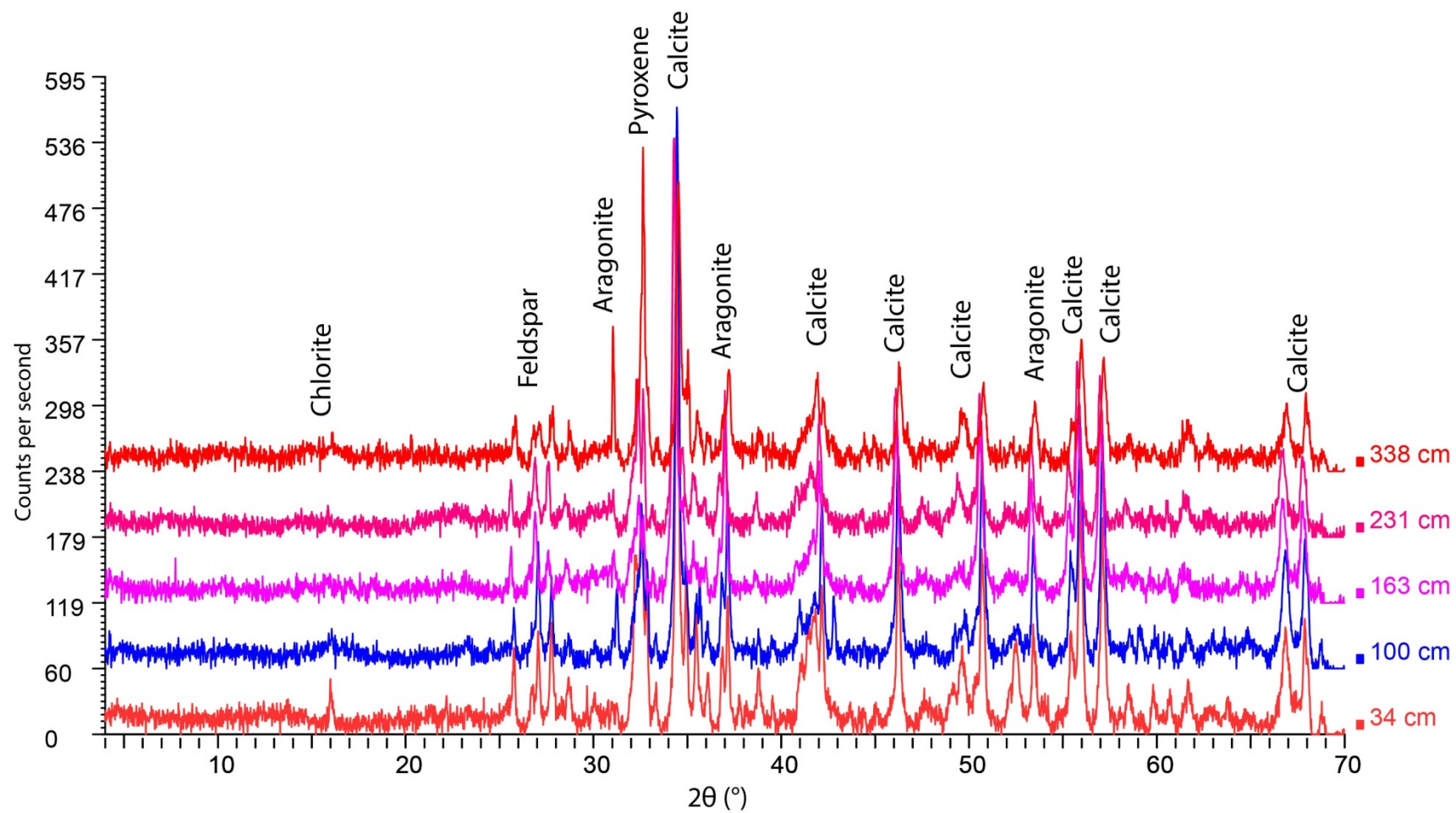
GC23



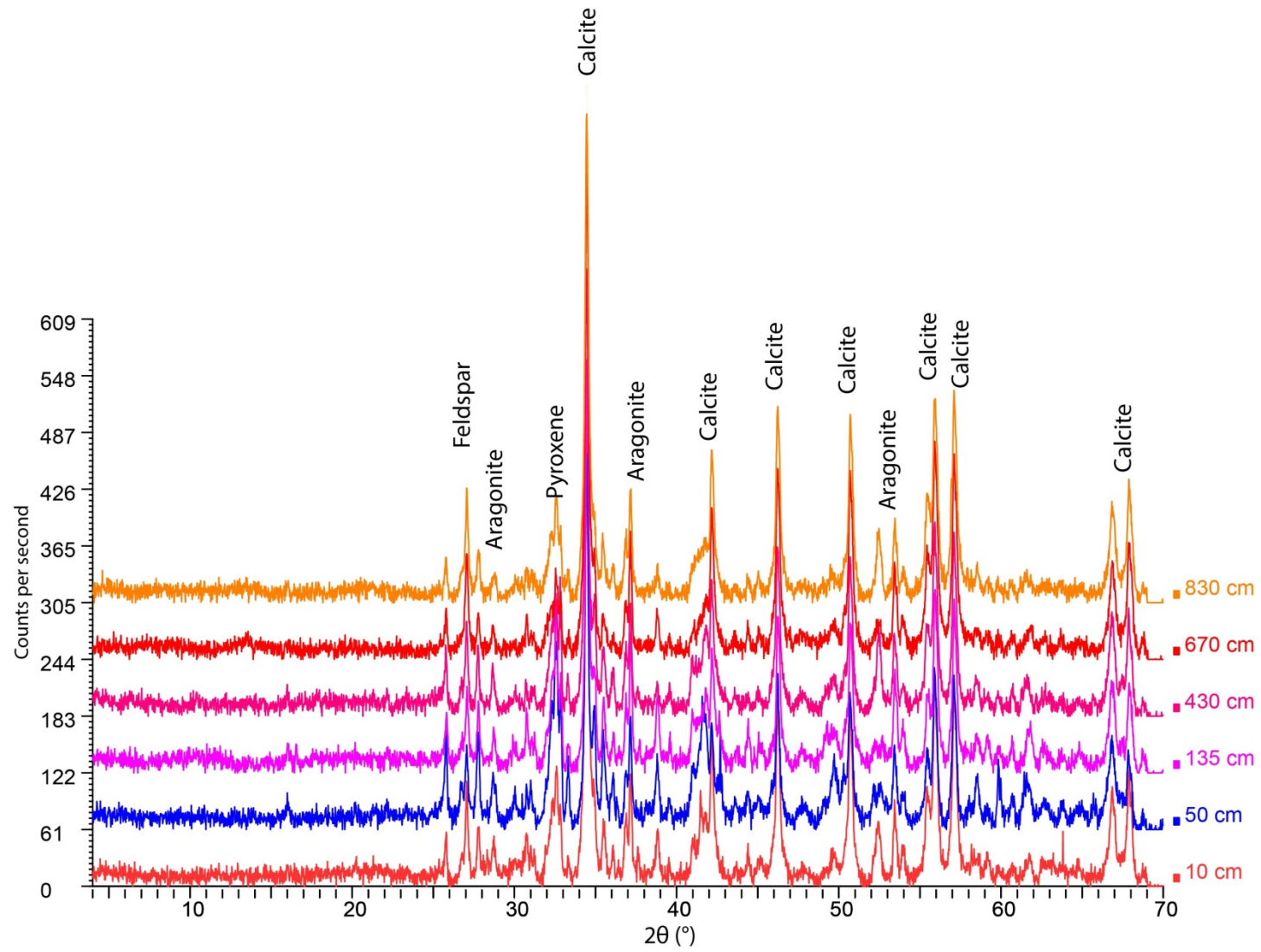
GC27



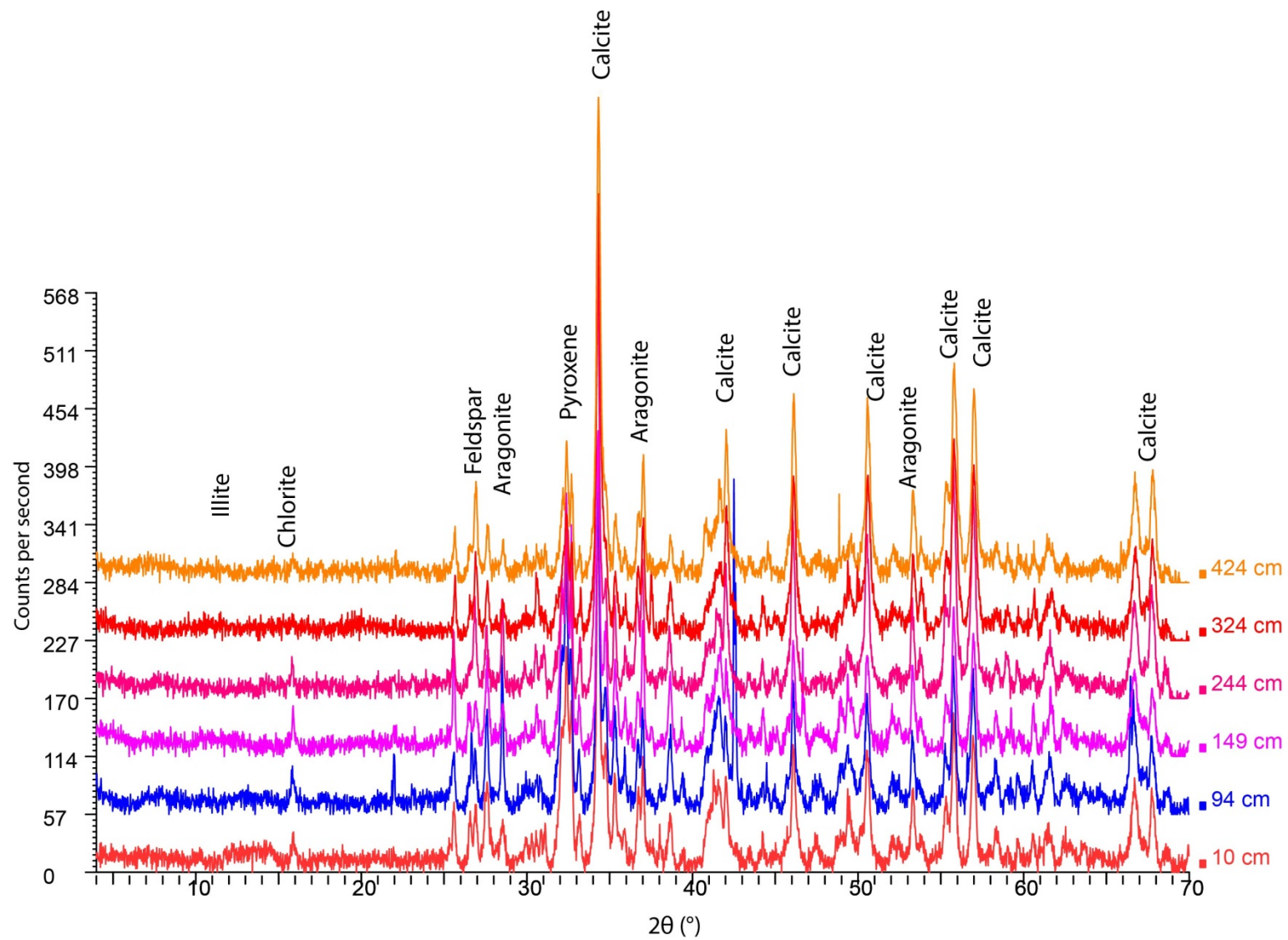
GC29



GC31



GC38



Appendix C for chapter IV

C1 Head space samples and pH calculations

Table C1 GC50

Depth [cm]	CH ₄ [μM]	fCO ₂ [ppm]	pH [#]
23	0.0915	1282	7.71
48	0.1397	1820	7.61
66	0.1650	1365	
85	0.1582	2634	7.76
109	0.1092	1752	7.67
134	0.1551	2850	7.49
166	0.2648	707	

Table 2C2 GC51

Depth [cm]	CH ₄ [μM]	fCO ₂ [ppm]	pH [#]
17	0.0831	2042	7.65
42	0.1216	3177	7.65
49	0.1291	2831	7.62
68	0.1438	1872	
87	0.1251	5429	7.45
105	0.2561	5599	7.52
118	0.1515	4734	7.56
140	0.1683	3493	7.72
161	0.1407	1008	7.81
172	0.1068	2775	

pH was calculated using co2sys.xls program by *Pelletier et al.* [2005]

C2 Solid phase bulk elemental composition

Table C3 GC50; grey highlighted samples are taken within ash layers.

Depth [cm]	Al ₂ O ₃ [wt%]	CaO [wt%]	CaO* [wt%]	Fe ₂ O ₃ [wt%]	K ₂ O [wt%]	MgO [wt%]	Na ₂ O [wt%]	SrO [wt%]	CaCO ₃ [%]	TIC [%]	Corg [%]	CIA [#] [%]
20	25.88	11.87	2.56	4.58	7.39	1.82	11.95	0.07	15.26	1.83	0.146	54.16
37	29.03	9.98		6.91	6.48	3.85	10.23	0.08				
44	22.38	16.37	0.91	3.01	7.28	1.03	11.56	0.08	5.42	0.65	0.262	53.12
96	20.70	21.48	4.24	5.04	4.62	2.59	8.25	0.12	25.25	3.03	0.279	54.75
116	26.53	14.90	1.05	6.96	5.02	3.80	8.74	0.08	6.28	0.75		64.18
126	24.92	14.60	3.57	4.16	6.57	1.65	10.45	0.08	21.30	2.56	0.293	54.76

Table C4 GC51 grey highlighted samples are taken within ash layers.

Depth [cm]	Al ₂ O ₃ [wt%]	CaO [wt%]	CaO* [wt%]	Fe ₂ O ₃ [wt%]	K ₂ O [wt%]	MgO [wt%]	Na ₂ O [wt%]	SrO [wt%]	CaCO ₃ [%]	TIC [%]	Corg [%]	CIA [#] [%]
30	22.20	16.57	4.02	3.68	6.84	1.87	12.62	0.08	23.95	2.87	0.252	48.60
40	21.75	19.42	4.90	3.04	7.07	1.07	11.34	0.09	29.19	3.50	0.264	48.27
55	25.68	12.10	2.69	4.49	7.71	1.99	12.34	0.07	16.01	1.92	0.151	53.04
102	22.75	18.57	3.90	5.85	4.86	2.93	8.37	0.11	23.24	2.79	0.129	57.06
126	28.08	12.99	1.53	7.52	5.05	3.90	8.28	0.08	9.10	1.09	0.057	65.40
142	24.30	14.92	3.65	4.31	6.50	1.75	10.28	0.09	21.75	2.61	0.261	54.32
152	25.75	12.69	1.12	8.36	4.83	5.40	7.15	0.08	6.65	0.80	0.043	66.29

* The Ca bound to silicates (CaO*) was approximated by subtracting Ca bound to carbonates ($\text{CaCO}_3 = 8.33 \cdot \text{TIC}$) from total Ca.

Chemical Index of Alteration (CIA) after *Nesbitt and Young* [1982] was calculated as follows: $\text{CIA} = \text{Al}_2\text{O}_3 / (\text{Al}_2\text{O}_3 + \text{CaO}^* + \text{Na}_2\text{O} + \text{K}_2\text{O}) \times 100$

C3 Microscopic description

C3.1 GC50

Microscopic inspection of the sediments classifies them as nannofossil-rich mud to mud-rich nannofossil ooze with variable admixture of volcanic, siliciclastic, and biogenic material. Quantitative smear slide analysis specifies that the predominant mud is composed of a mixture of clay and silt (not to be further distinguished by simple inspection of the cores) with some additions of sand. The typical silty clay and clayey silt facies are dominated by calcareous nannofossils with rare (1 vol% – 8 vol%) but persistent admixtures of feldspar, pyroxene, amphibole and biotite. Common to abundant amounts (8 vol% - 31 vol%) of transparent (felsic) and brown (mafic) volcanic glass are found in all investigated samples. Felsic glass shards normally exceed over mafic ones with the exception of sample M141_GC50_116 cm which is dominated by brown glass (56,3 vol%) and therefore classified as mafic ash with foraminifers. Rare to common lithic volcanic lithic clasts (1 vol% – 13 vol%) include glass, partly devitrified, plagioclase and ferromagnesian minerals. Sedimentary lithic clasts occur in rare to common amounts and consist of rounded and hardened mudstone. Granules of opaque iron oxide, as well as spinel, chlorite, and carbonate clasts are rare to vary rare. Next to nannofossils, the fine-grained sediment commonly contains significant amounts of well-preserved microfossils (2 vol%-13 vol%) in the form of foraminifers, sponge spicules, and diatoms, plus spasmodic occurrences of radiolarians.

Table C5 GC50

Depth		Glass (transparent)	Glass (brown)	glass total	Feldspar	Pyroxene	Amphibole	Biotite	Opaque	Lithics sed	Lithics vol	Lithic total	Clay	Nannofossils	Foraminifers	Biogenic rest	microfossil	Total
20 cm	mud-rich nanofossil ooze with glass	15	6.7	21.7	7.4	3.5	0.4	1.5	0.7	6.2	4	10.2	3.1	49.7	1.1	0.7	1.8	100
37 cm	tuffaceous nannofossil- rich mud	10.8	9.5	20.3	4.9	4.6	1.3		2	13.8	13.1	26.9	15	20.1	3.9	1	4.9	100
44 cm	tuffaceous nannofossil- rich mud	27.4	4	31.4	8.3	2.2	0.9	0.9	1	7.6	3.2	10.8	11	24.4	4.4	4.7	9.1	100
96 cm	mud-rich nanofossil ooze	3.9	4.2	8.1	3.6	2	0.6		1.5	6.8	2.3	9.1	18	53.2	0.7	3.2	3.9	100
116 cm	mafc ash with foraminifers	1.7	56.3	58	5.6	2			2.3	1.3	1.3	2.6	7.3	9.6	10.6	2	12.6	100
126 cm	mud-rich nanofossil ooze with glass	12.3	2.7	15	5.6	2		0.6	1.7	1.7	1	2.7	15.3	55.2	1.3	0.6	1.9	100

C3.2 GC51

Core 51 sediments mainly consist of tuffaceous nannofossil-rich mud with variable amounts of nannofossils (13 vol% - 36 vol%) and ash (19 vol% - 36 vol%). Quantitative smear slide analysis reveals that the predominant mud is composed of a mixture of clay, silt, and the coarser sand fraction (10 vol% - 50 vol%). Next to ash and nannofossils, the sediment is predominantly composed of clay (12 vol% - 29 vol%) with rare to common (3 vol% - 7 vol%) feldspar, and pyroxene, as well as very rare to rare but persistent admixtures of amphibole, opaque minerals, and biotite (0.3 vol% - 2 vol%); occasionally olivine occurs. Generally, the ash content is slightly higher than in core GC50. With one exception, common to abundant amounts of transparent (felsic) glass shards (21 vol % - 36 vol%) dominate the first 60 cm of the sediment. Brown (mafic) volcanic glass, including two brownish ash layers with more than 54% brown glass at a depth of 126 cm bsf and 152 cm bsf, is predominantly found in the deeper samples. Rare to common volcanic lithic clasts (1vol% – 10 vol%) include glass, partly devitrified, plagioclase and ferromagnesian minerals. Sedimentary lithic clasts occur in rare to common amounts (2 vol% - 10 vol%) and consist of rounded and hardened mudstone. Chlorite and carbonate clasts occur in traces. Next to nannofossils, the fine-grained sediment commonly contains significant amounts of well-preserved microfossils (4 vol% - 11 vol%) in the form of foraminifers, sponge spicules, and diatoms, plus spasmodic occurrences of radiolarians. In comparison to core GC50 the sediment inventory in core GC51 is composed more of mafic and terrigenous matter, especially in the deeper parts of the core.

Table C6 GC51

Depth	Name	Glass (transparent)	Glass (brown)	glass total	Feldspar	Pyroxene	Amphibole	Biotite	Olivine	Opaque	Lithics sed	Lithics vol	Lithic total	Clay	Nanno- fossils	Foram- inifers	Biogenic rest	microfossil	Total	mafic terrigenous
30 cm	tuffaceous nannofossil- rich mud	22.2	7	29.2	7.3	3.6	1.5			0.7	8.6	5	13.6	12.4	24	6	1.7	7.7	100	17.8
40 cm	tuffaceous nannofossil- rich mud	35.6		35.6	3.6	2.6	2.3	1.3		1.6	1.9	2.9	4.8	16.5	27.5	2.9	1.3	4.2	100	9.4
55 cm	tuffaceous nannofossil- rich mud	20.8	4.6	25.4	7.3	4	1.7	0.3		1.3	9.6	9.9	19.5	22.3	12.5	5	0.7	5.7	100	21.5
102 cm	tuffaceous nannofossil ooze with mud	7.6	20.9	28.5	5.3	2.7	0.3	0.3	0.7	1.3	1.3	0.7	2	16	36.2	3	3.7	6.7	100	26.6
126 cm	nanofossil- rich mafic ash with foraminifers	2.6	51.3	53.9	5.3	3.3			1.2	2	3.3	4.3	7.6	7.3	11.6	7.3	0.5	7.8	100	62.1
142 cm	tuffaceous nannofossil- rich mud	16.3	2.3	18.6	5	2.7	2.3	0.7		3	4.7	3	7.7	28.7	22.9	3.7	4.7	8.4	100	13.3
152 cm	mafic ash with foraminifers	2.6	53.9	56.5	7	6			1.7	1.3	2.3	4.7	7	3	6.3	10.2	1	11.2	100	67.6

C4 End member calculation

**Table C7 Mixing between seawater and fluid for Sr; in yellow the measured concentration of GC51
($^{87}\text{Sr}/^{86}\text{Sr} = 0.7074$; $\text{Sr} = 153 \mu\text{M}$) is marked**

	Ratio	$^{87}\text{Sr}/^{86}\text{Sr}$	Sr [μM]
Seawater	1.00	0.7092	90
	0.95	0.7080	118
GC51	0.90	0.7073	146
	0.85	0.7068	174
	0.80	0.7064	202
	0.70	0.7060	258
	0.60	0.7056	314
	0.50	0.7054	370
	0.40	0.7053	426
	0.30	0.7051	482
	0.20	0.7050	538
	0.10	0.7050	594
Fluid EM	0.00	0.7049	650

**Table C8 Mixing between seawater and fluid for Mg/Sr; in yellow the measured concentration of GC51
($\text{Mg} = 59.09 \text{ mM}$; $\text{Sr} = 153 \mu\text{M}$; $\text{Mg}/\text{Sr} = 0.39$) is marked**

	Ratio	Mg/Sr	Sr
Seawater	1	0.6111	90
	0.95	0.4788	118
GC51	0.9	0.3973	146
	0.85	0.3419	174
	0.8	0.3020	202
	0.7	0.2481	258
	0.6	0.2134	314
	0.5	0.1892	370
	0.4	0.1714	426
	0.3	0.1577	482
	0.2	0.1468	538
	0.1	0.1380	594
Fluid EM	0	0.1308	650

Table C10 Mixing between seawater and fluid for Mg/Ca; in yellow the measured concentration of GC51 (Mg = 59.09 mM; Ca = 10.99 mM; Mg/Ca = 5.38) is marked

	Ratio	Mg/Ca	Ca
Seawater	1	5.50	10.5
	0.95	5.4356	10.9
GC51	0.9	5.3756	11.3
	0.85	5.3194	11.6
	0.8	5.2667	12.0
	0.7	5.1706	12.8
	0.6	5.0852	13.5
	0.5	5.0088	14.3
	0.4	4.9400	15.0
	0.3	4.8778	15.8
	0.2	4.8212	16.5
	0.1	4.7696	17.3
Fluid EM	0	4.72	18.0

Table C11 Mixing between seawater and fluid for Mg/Ca; in yellow the measured concentration of GC51 (Mg = 59.09 mM; SO4 = 30.84 mM; Mg/SO4 = 1.91) is marked

	Ratio	Mg/SO ₄	SO ₄
Seawater	1	1.9272	28.80
	0.95	1.9177	29.71
GC51	0.9	1.9089	30.62
	0.85	1.9006	31.53
	0.8	1.8927	32.44
	0.7	1.8783	34.26
	0.6	1.8653	36.08
	0.5	1.8536	37.90
	0.4	1.8429	39.72
	0.3	1.8332	41.54
	0.2	1.8243	43.36
	0.1	1.8161	45.18
Fluid EM	0	1.8085	47.00

References

- Nesbitt, H. W., and G. Young (1982), Early Proterozoic climates and plate motions inferred from major element chemistry of lutites, *Nature*, 299(5885), 715.
- Pelletier, G., E. Lewis, and D. Wallace (2005), A calculator for the CO₂ system in seawater for Microsoft Excel/VBA, *Washington State Department of Ecology, Olympia, WA, Brookhaven National Laboratory, Upton, NY*.

Curriculum Vitae

Christopher Schmidt

Hansastr.20

24118 Kiel

cschmidt@geomar.de

Personal Information

Date of Birth: 08.April 1988

Place of Birth: Freiburg im Breisgau, Germany

Education

Since 09/2016 GEOMAR Helmholtz Centre for Ocean Research Kiel, Germany,
Doctoral Candidate

10/2013 - 03/2016 Master of Science, Geoscience, Christian-Albrechts Universität zu Kiel,
Germany

10/2009 -10/2012 Bachelor of Science, Applied Geoscience, Karlsruhe Institute of
Technology (KIT), Germany

Professional Work Experience

04/2016 – 08/2016 GEOMAR Helmholtz Center for Ocean Research Kiel, Germany,
Research Fellow

11/2012- 07/2013 CSIRO, Floreat (Perth), Western Australia,
Student researcher

Publications

Peer- Reviewed Articles

Hensen, C., Duarte, J. C., Vannucchi, P., Mazzini, A., Lever, M. A., Terrinha, P., Géli, L., Henry, P., Villinger, H., Morgan, J., Schmidt, M., Gutscher, M.-A., Bartolome, R., Tomonaga, Y., Polonia, A., Gràcia, E., Tinivella, U., Lupi, M., Çağatay, M. N., Elvert, M., Sakellariou, D., Matias, L., Kipfer, R., Karageorgis, A. P., Ruffine, L., Liebetrau, V., Pierre, C., **Schmidt, C.**, Batista, L., Gasperini, L., Burwicz, E., Neres, M., and Nuzzo, M., 2019, Marine Transform Faults and Fracture Zones: A Joint Perspective Integrating Seismicity, Fluid Flow and Life: *Frontiers in Earth Science*, v. 7, no. 39.

Schmidt, C., Burwicz, E., Hensen, C., Wallmann, K., Martinez-Loriente, S., and Gracia, E., 2018, Genesis of mud volcano fluids in the Gulf of Cadiz using a novel basin-scale model approach: *Geochimica et Cosmochimica Acta*, v. 243, p. 186-204.

Devey, C. W., Augustin, N., Brandt, A., Brenke, N., Köhler, J., Lins, L., **Schmidt, C.**, and Yeo, I. A., 2018, Habitat characterization of the Vema Fracture Zone and Puerto Rico Trench: *Deep Sea Research Part II: Topical Studies in Oceanography*, v. 148, p. 7-20.

Wallmann, K., Riedel, M., Hong, W. L., Patton, H., Hubbard, A., Pape, T., Hsu, C. W., **Schmidt, C.**, Johnson, J. E., Torres, M. E., Andreassen, K., Berndt, C., and Bohrmann, G., 2018, Gas hydrate dissociation off Svalbard induced by isostatic rebound rather than global warming: *Nature Communications*, v. 9, no. 1, p. 83.

Scientific communications

Schmidt, C., Hensen, C., Wallmann, K., Liebetrau, V., Tatzel, M., Schurr, S.L., Geilert, S., Hübscher, C., Kutterolf, S., Lebas, E., Haffert, L., Strauss, H. and Hansteen T., (2019); Genesis of high Mg and SO₄ hydrothermal fluids in the Terceira Rift, EGU General Assembly 2019, Vienna (Talk)

Schmidt, C., Hensen, C., Hübscher, C., Wallmann, K., Tatzel, M., Schurr, S.L., Liebetrau, V., Geilert, S., Kutterolf, S., Strauss, H. and Hansteen T., (2019); Insights into pore fluid geochemistry of the Azores Plateau: From early diagenesis to hydrothermal vents; EGU General Assembly 2019, Vienna (PICO)

Schmidt, C., Hensen, C., Schmidt, M., Kutterolf, S., Huebscher, C. and Hansteen, T. (2018) Hydrothermal pore fluid characterization of the Azores Plateau, EGU General Assembly 2018, Vienna (Talk)

Schmidt, C., Burwicz, E., Hensen, C., Martínez-Loriente, S., Gràcia, E. and Wallmann, K. (2017) Genesis of mud volcano fluids of Porto MV in the Gulf of Cadiz, FLOWS-Cost Meeting, Granada (Poster)

Hong, W.-L., **Schmidt, C.**, Yao, H., Wallmann, K., Rae, J., Lepland, A., Torres, M.E., Plaza-Faverola, A., Latour, P., Bunz, S., Bohrmann, G., (2017) Fracture-induced fluid migration in an Arctic deep water pockmark: Porewater geochemistry from the MEBO

drilling (MSM57) in Vestnesa Ridge (Svalbard) , Goldschmidt Conference 2017, Paris (Poster)

Wallmann, K., Riedel, M., Hong, W.-L. **Schmidt, C.**, and Bohrmann, G. (2017) Gas Hydrate Dissociation at the Continental Margin off Svalbard Induced by Glacial Rebound Rather Than Global Warming, ICGH9 Conference, Denver (Talk)

Schmidt, C., Burwicz, E., Hensen, C., Martínez-Loriente, S., Gràcia, E. and Wallmann, K. (2017) Genesis of mud volcano fluids in the Gulf of Cadiz - A novel model approach, EGU General Assembly 2017, Vienna (Poster)

Schmidt, C., Hensen, C. and Wallmann, K. (2016) Geochemical modeling of subsurface fluid generation in the Gulf of Cadiz, FLOWS- Cost Meeting, Barcelona (Talk)

Schmidt, C., Hensen, C. and Wallmann, K. (2016) Geochemical modeling of subsurface fluid generation in the Gulf of Cadiz, EGU General Assembly 2016, Vienna (Poster)